Investigation of metal - insulator transition in magnetron sputtered samarium nickelate thin films

Katarzyna Bilewska

Institute of Physics, Department of Solid State Physics

University of Silesia

A thesis submitted for the degree of

PhilosophiæDoctor

Work done under the supervision of Prof. Dr hab. Jacek Szade

September 2019

Abstract

Metal-insulator transition is one of the most interesting phenomena to be investigated in the matter of solid state physics. Not only for the possible applications but for the pure physics of this phenomenon there has been immense number of works devoted to its investigation. The origin and driving factor of the transition may differ significantly depending on the material of interest, be it Coulomb repulsion, spin-orbit coupling and others. Among a vast number of compounds rare earth nickelates, the object of this thesis, represent only one type of transition.

In those materials, the transition is yet to be thoroughly described. Present description involves considering charge disproportionation on the nickel site, which in turn affects the overlap between the nickel and oxygen ligand bands and thus the electrical conductivity of the material. A consistent variation of electrical properties between the members of the nickelate family with respect to rare earth element has been observed. That occurs simultaneously with the level of structural distortion down the family line. If the structural distortion is the driving force for the transition, its influence should also be evidenced with respect to dimensions of the material. The argument that is discussed in this dissertation is that reduced dimension of samarium nickelate compound does influence its crystalline structure and, what follows, the electronic structure and metal-insulator transition. This correlation is a possible starting point for developing theory on metal-insulator transition in thin films.

The argument is verified by studying a series of magnetron sputtered samarium nickelate thin film materials with variable thickness and synthesis conditions. As a result, nearly amorphous, polycrystalline as well as strongly textured films were obtained in thickness range between 20-500 nm. Both surface sensitive and bulk measurement techniques were used to characterize the materials and investigate the occurrence of the metal-insulator transition. However the investigation

was impeded by a chromium oxide surface contamination arising from necessary post-deposition treatment.

Despite the difficulties, it was possible to verify the occurrence of the metal-insulator transition. The effect is correlated with obtained Raman spectra and temperature variation of the modes‘ position. Changes observed for polycrystalline films were in general smaller and less prominent than those in textured films. Even though the amorphous films did not present the correct crystalline structure and Raman modes as for distorted nickelate perovskite, the electronic structure variation across wider temperature range was noted. In fact all data obtained by X-ray Photoelectron Spectroscopy suggest that temperature-induced changes of electronic structure of nickel band do occur in every studied sample. Comparison of energy separation of Ni $2p_{3/2}$ component peaks and the magnitude of its temperature alteration indicate that the most severe changes occur in the thinnest films. The film that had a high lattice mismatch, large Raman temperature shift and high MI temperature, also happens to have a high XPS energy separation and the magnitude of its temperature change.

The results show that the disproportionation of nickel charge is not specific for the insulating state in samarium nickelate thin films. It appears also in metallic state, although its magnitude is lower. On top of that it is even present in films that do not contain the proper crystalline structure. The transition occurs at higher temperature for thinner films that also have higher level of lattice mismatch. It is argued that for such a thin film the strain is large enough to require higher thermal energy to induce variation in nickel-oxygen bond lengths and the band overlap. The crystalline preferred orientation also influences the transition however small number of samples made it difficult to grasp more details of that behaviour.

The effect of thickness and crystal structure presented in this work is a variation of the classical rare-earth ion effect. The metal-insulator transition can be modified by changing materials dimensions and crystal orientation. This anisotropy and size effect is important in view of future adaptation of the transition to specific needs.

Streszczenie

Przejście metal-izolator jest jednym z najciekawszych zjawisk, którymi zajmuje się fizyka ciała stałego. Nie tylko ze względu na możliwe zastosowania tego zjawiska ale przede wszystkim ze względu na samą jego fizykę, ogromna ilość prac jest poświęcona badaniu go. Geneza i kluczowe czynniki jego występowania takie jak odpychanie kulombowskie, rozszczepienie spin-orbita czy inne, różnią się znacznie w zależności od rozważanego materiału. Pośród dużej grupy materiałów nikielaty ziem rzadkich, obiekt badań tej pracy, reprezentują tylko jeden rodzaj przejścia.

W tych materiałach przejście metal-izolator czeka jeszcze na pełne wyjaśnienie. Obecny opis uwzględnia nierównowagowe rozłożenie ładunku (charge disproportionation) na jonach niklu, co z kolei wpływa na przekrywanie się pasm niklu i tlenu a w związku z tym na przewodnictwo elektryczne w materiale. Zaobserwowano spójną zmienność właściwości elektrycznych między członkami rodziny nikielatów w odniesieniu do pierwiastka ziem rzadkich. Zmiany te związane są jednocześnie z poziomem zniekształceń strukturalnych. Jeśli zniekształcenie strukturalne jest siłą napędową przejścia, można również wykazać jego wpływ w odniesieniu do wymiarów materiału. Teza dyskutowana w niniejszej rozprawie zakłada, że nanoskopowe wymiary nikielatu samarowego wpływają na jego strukturę krystaliczną, a co za tym idzie, na strukturę elektronową i przejście metal-izolator. Ta korelacja jest możliwym punktem wyjścia do opracowania teorii dotyczącej przejścia metal-izolator w cienkich warstwach.

Postawiona teza jest weryfikowana poprzez badanie szeregu materiałów tlenków samarowo-niklowych w postaci cienkich warstw napylanych magnetronowo, o zmiennej grubości i zmiennych warunkach syntezy. Otrzymano prawie amorficzne, polikrystaliczne, oraz silnie steksturowane warstwy o grubości od 20 do 500 nm. Do scharakteryzowania materiałów i zbadania przejścia metal-izolator zastosowano zarówno techniki pomiarowe powierzchniowo czułe, jak i metody objętościowe. Badania utrudniało jednak zanieczyszczenie powierzchni tlenkiem chromu wynikające z niezbędnej końcowej obróbki termicznej.

Pomimo tych trudności udało się zweryfikować występowanie przejścia metal-izolator. Zjawisko to jest skorelowane z uzyskanymi widmami Ramana i zmianami temperatury pozycji modów ramanowskich. Zmiany zaobserwowane w powłokach polikrystalicznych były w ogólności mniejsze i mniej wyraźne niż w przypadku warstw z preferowaną orientacją. Ponadto, chociaż warstwy amorficzne nie wykazywały prawidłowej struktury krystalicznej i modów Ramana odpowiednich dla rombowej struktury niekielatu, zauważono zmianę struktury elektronowej w szerszym zakresie temperatur. W rzeczywistości wszystkie dane uzyskane za pomocą spektroskopii fotoelektronów rentgenowskich sugerują, że w każdej badanej próbce zachodzą zmiany struktury elektronowej pasma niklu wywołane temperaturą. Porównanie różnic energii wiązania składowych Ni $2p_{3/2}$ i jej zmian w zależności od temperatury wskazują, że największe zmiany zachodzą w najcieńszych warstwach. Warstwa, która miała duże niedopasowanie strukturalne w stosunku do podłoża, duże przesunięcie temperatury Ramana i wysoką temperaturę MI, również ma wysoki rozdziałenergii XPS i wielkość jego zmiany temperatury.

Wyniki pokazują, że dysproporcja ładunku niklu nie jest charakterystyczna dla stanu izolatora w cienkich warstwach $SmNiO_3$. Pojawia się także w stanie metalicznym, chociaż jest mniejsza. Ponadto występuje nawet w powłokach, które nie zawierają odpowiedniej struktury krystalicznej. Przejście występuje w wyższej temperaturze w przypadku cieńszych warstw, które również mają wyższy poziom niedopasowania sieci. Argumentuje się, że w przypadku tak cienkiej warstwy odkształcenie jest wystarczająco duże, aby wymagać wyższej energii cieplnej, aby wywołać zmiany długości wiązań nikiel-tlen i zachodzenia pasm na siebie. Preferowana orientacja krystaliczna również wpływa na przejście, jednak niewielka liczba próbek utrudniała uchwycenie szczegółów tego zachowania.

Przedstawiony w pracy efekt grubości i struktury krystalicznej jest odmianą klasycznego efektu jonów metali ziem rzadkich. Przejście metal-izolator można modyfikować, zmieniając wymiary materiałów i orientację kryształów. Efekt anizotropii i rozmiaru jest ważny z uwagi na przyszłe dostosowanie przejścia MI do konkretnych potrzeb.

To Marcin, my love

To my family, my foundations

Acknowledgements

At first and foremost I would like to thank my supervisor Professor Jacek Szade who assisted my scientific development, openly sharing his knowledge and experience, always willing to discuss and dispel my doubts regarding the work I have done. He facilitated my work in various laboratories and allowed me freely use the advanced scientific equipment. Owing to that and his kindness I have always felt 'at home' when performing any experiments in the laboratories of Department of Solid State Physics.

I would like to acknowledge Professor Pascal Ruello from Université du Maine in Le Mans for allowing me use the magnetron sputtering equipment to obtain the thin film material for investigation. This work would not be possible if I did not receive his help and experience during my time spent in Le Mans preparing my master's thesis.

I am grateful to Institute of Non-Ferrous Metals in Gliwice and Department of Powder and Composite Materials for allowing me use the equipment to perform some of the valuable experiments presented in this work. I want to thank Dr Mariusz Staszewski for what he taught me about X-ray diffraction and for his passion and patience in teaching.

I can never be enough thankful for help received from Dr Katarzyna Balin, Dr Jurek Kubacki, Dr Marek Kulpa for assistance when performing experiments in UHV cluster equipment, for making time pass in good atmosphere and for their unrestricted help whenever anything went wrong. I would like to thank Dr Mateusz Dulski for performed Raman spectroscopy experiments and his constant willingness to help.

I need to thank my friends and colleagues at University and at work - Ania, Kinga, both Gosias, Darek, Alicja, Kasia, Adriana, Andrzej, Marcin, Jacek, Piotr and every other one that I do not mention here.

I also want thank from the depth of my heart to my friends Adam Dusza, Justyna Wójcik and Asia Markowska. Thank you for your genuine support and uplifting conversations.

I am immeasurably grateful to my mother and my brother Olek. You both supported me when I did not believe I could achieve what I initially aimed at. You taught me how important it is to perfect myself, to never give up, to search for purpose and meaning.

Last but not least I am immeasurably grateful to my fiancé Marcin. With your inexhaustible sense of humour that made the darkest moment light up, all the stress would go away. You did everything to make me believe that I am capable of doing whatever I want in life.

In the end I want to acknowledge the financial support from the UP-GOW and DoktoRIS programmes funded by the European Union through the European Social Funds (ESF).

Contents

List of Figures

LIST OF FIGURES

LIST OF FIGURES

List of Tables

LIST OF TABLES

Glossary

AF antiferromagnetic

AFM Atomic Force Microscopy

BE binding energy

CAFM Conductive Atomic Force Microscopy

DMFT Dynamical mean field theory

DOS density of states

GIXRD grazing incidence X-ray diifraction

GS Gupta and Sen

IMFP inelastic mean free path

IR infrared

J-T Jahn-Teller

LAO $LaAlO_3$

LC-AFM Local Conductivity Atomic Force Microscopy

LHB lower Hubbard band

LNO $LaNiO_3$

MI metal-insulator

MIT metal-insulator transition

NGO $NdGaO_3$

NIR near infrared

NNO $NdNiO_3$

PLD Pulsed Laser Deposition

PM paramagnetic

RE rare earth

RF radio-frequency

RNO $RNiO_3$

RP Ruddlesden-Popper

RS Resistive Switching

RT room temperature

SAED Selected Area Electron Diffraction

SC space-charge

SCLC space-charge-limited conduction

SIMS Secondary Ion Mass Spectroscopy

SNO $SmNiO_3$

SPM Scanning Probe Microscopy

STO $SrTiO_3$

T_{MI} metal-insulator transition temperature

T_N Néel temperature

TEM Transmission Electron Microscopy

TM transition metal

TMO transition metal oxide

TOF-SIMS Time-of-Flight SIMS

u.c. unit cell

UHB upper Hubbard band

UHV High Ultra Vacuum

UPS Ultraviolet Photoelectron Spectroscopy

UV ultraviolet

GLOSSARY

VBM Valence Bond Model

VBS Valence Bond Sum

VRH Variable Range Hopping

XPS X-ray Photoelectron Spectroscopy

XRD X-ray Diffraction

XRF X-ray Fluorescence Spectroscopy

XRPD X-ray Powder Diffraction

ZSA theory Zaanen, Savatzky and Allen theory

1

Introduction

Since the discovery of high-temperature superconductivity, there has been a growing interest in conducting metal oxides as this is quite uncommon behaviour for an oxide compound. In particular, complex metal oxides possess a variety of interesting structural, electronic, magnetic and optical properties - figure 1.1 (60). Although this work is focused on only one member the family of perovskite nickelates $SmNiO_3$ (SNO), it is worth to mention the whole family, which is described by the chemical formula $RNiO_3$ (RNO), where R (or RE) is a trivalent rare-earth ion such as La, Pr, Nd, Sm, or Lu. These nickelates are characterized by a variety of interesting physical properties and structures.

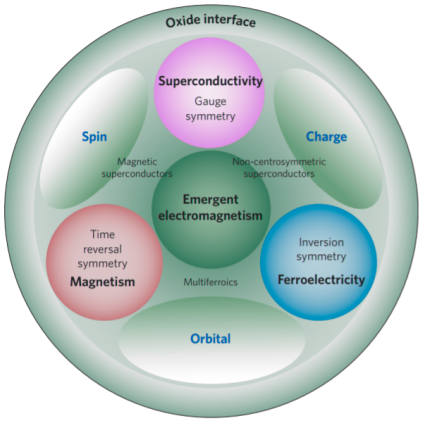

Figure 1.1: Phenomena in complex oxides - Diagram showing possible physical phenomena that can be found on the complex oxide interface with respective electron symmetries. Adapted from (60)

One of the main features of $RNiO_3$ family (with the exception of R = La), is a distinct metal-to-insulator transition (MIT). MIT in these compounds is strongly dependant on the Ni-O-Ni bond length and angle between those bonds thus are quite sensitive to the compound structure. This leads to the possibility to design properties of the material using a variety of parameters such as temperature or doping and structural strain as well. It is not so easy to introduce strain in the single crystal or in a bulk form without changing the material stoichiometry or by applying high pressure. Instead, I have decided to utilize the strain that emerges when the material is grown as a thin film. This strain can be further tailored by two factors:

a) The mismatch between the lattice parameter of the film and the lattice structure of the substrate will lead to strain. By varying the thin film thickness one can obtain different levels of epitaxial strain (thicker layer should be less strained).

b) The thin film preparation conditions (growth atmosphere) and post grow processes like annealing, which leads to the growth of the different size of crystallites and elevate internal stress.

By tailoring the physical properties (such as MIT) one can find many possible applications for the $SmNiO_3$ compound. A scheme of some of the potential applications can be found in figure 1.2. The first two applications are related to the same phenomena - Resistive Switching (RS). This effect can be explained as a permanent change in the resistance under the influence of some stimuli. It is typically observed in oxides and can originate from a variety of effects, where the formation of conducting channels and filaments by oxygen vacancies seems to be most common. However, in nickelates (or in the nickel oxide) it is often found that the Ni is more mobile than the oxygen (or oxygen vacancy). From this, a concept of memristor (a resistor with memory) was proposed and generated significant interest for its possible application as a non-volatile memory or as an element similar in its working principle to a neuron or a synapse (88). Further, the MIT is connected to drastic changes in the optical properties of the material, therefore leads to the possible application as an optoelectronic device. Those devices are ranging from electro-optic modulators, smart glasses for controlling sunlight intensity, thermoregulation or infrared camouflage (71). The relatively new idea is the use of $SmNiO_3$ as a fuel cell material (electrolyte), where the electronic conduction can be tuned (or limited) by spontaneous hydrogen incorporation (101).

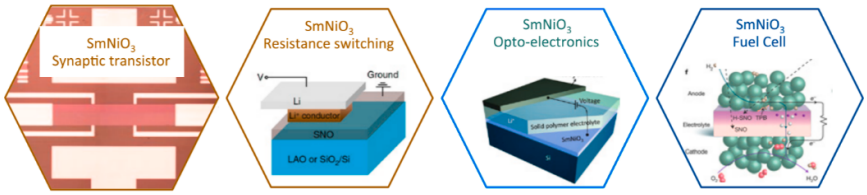

Figure 1.2: Applications of $SmNiO_3$ - Schematic view of potential applications of $SmNiO_3$ in the field of electronics, photonics, or fuel cells.

Table 1.1: Bond lengths of RE-O bonds in rare earth oxides, given in nm. * - trivalent monoxides, $^+$ - intermediate valent oxides. As presented in (23).

	La	Ce	Pr	Nd	Pm	Sm	Eu	Gd	Tb
REO	0.257*	0.254*	0.252*	0.250*	-	0.249^+	0.257	-	-
RE_2O_3	0.246	0.244	0.238	0.238	0.236	0.235	0.233	0.232	0.230
REO_2	-	0.234	0.233	-	-	-	-	-	0.226
	Dy	Ho	Er	Tm	Yb	Lu			
REO	-	-	-	-	0.244	-			
RE_2O_3	0.229	0.228	0.227	0.225	0.224	0.223			
REO_2	-	-	-	-	-	-			

1.1 Rare earth oxides

Rare earth oxides form a series of compounds that somehow follow the properties of the constituent metals. The 15 metals which are considered rare earths all have full $6s^2$ shell and with increasing atomic number progressively occupied $4f$ shell. Most of them have a $5d^0$ configuration except from La, Ce, Gd and Lu whose configuration is $5d^1$. The valence of the metals ranges from 2+ to 4+ in oxides, mostly being 3+ as is it the most stable. Some stand out of the series as trivalent monoxides - LaO, CeO and PrO. The long-lasting discussions have reveled that SmO does not exist in normal conditions as it would not be thermodynamically stable (30, 70). At normal conditions the stable form is Sm_2O_3. SmO can be obtained only at high pressure, about 40-50 kbar, where it exists as an intermediate valent oxide (70). Along the series, together with gradual localization of 4f electrons there appears a lanthanide contraction which is mostly responsible for their properties(87).

The electronic configuration, in particular the low-filling of outer d shell and

Table 1.2: Ionic radii of trivalent RE ions, given in nm. As presented in (23).

La^{3+}	Ce^{3+}	Pr^{3+}	Nd^{3+}	Sm^{3+}	Eu^{3+}	Gd^{3+}
0.123	0.115	0.114	0.112	0.106	0.106	0.104
Tb^{3+}	Dy^{3+}	Ho^{3+}	Er^{3+}	Tm^{3+}	Yb^{3+}	Lu^{3+}
0.100	0.099	0.098	0.096	0.094	0.093	0.092

its high energy, weakens possible Jahn-Teller (J-T) originating configuration instabilities.

The room temperature crystal structure of La, Ce and Pr based sesqioxide is hexagonal $P32/m$, while oxides from Sm to Lu have cubic bixbyite structure $Ia3$(1). Monoclinically distorted phase is the intermediate structure of space group $C2/m$.

The band gaps of single crystal oxides measured from optical spectra are larger than those obtained from conductivity experiments by a factor of almost two. The latter range from about 2 to 3 eV, while the former are between 4 and 5 eV, with the exception of cerium (about 2.3 eV). The variation of band gap values lead to four models of possible band gap structure. It is worth to mention, that the valence band in this model is composed of the occupied O p-states, as the conduction band is composed of mainly unoccupied RE d-states. The f-states, on the other hand, are more localized and can be found inside the bands or the band gap. The group A consists of oxides with the largest gap and the most stable configuration with f-states located within the bands instead of in the gap - La_2O_3, Gd_2O_3, Lu_2O_3, as well as in Dy_2O_3, Ho_2O_3, and Er_2O_3. The group B consists of oxides that are right after the most stable ones with significantly lower band gaps than group A - Ce_2O_3, Pr_2O_3, Nd_2O_3, and Tb_2O_3, with f-states located above the valence band. Those states can be excited into the conduction band giving lower E_g values. The group C consists of oxides which appear just before the most stable oxides and also have lower E_g values - Sm_2O_3, Eu_2O_3, Tm_2O_3, and Yb_2O_3, with empty f-states located below the conduction band. Finally, the D group consists of oxides having unoccupied and occupied f-states inside the gap, however no RE oxides can be attached to this group.

Thermodynamical stability of RE oxide thin films on silicon substrate is important for high-k applications. However some studies show a catalytic behaviour of RE oxides towards gaseous oxygen to dissociate it to atomic oxygen. This in turn can lead to formation of RE silicates (23). This is said to be even easier than

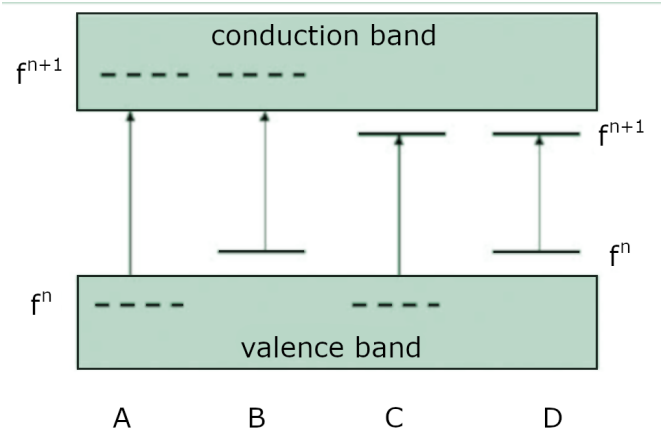

Figure 1.3: Band gap model for RE oxides - four types of the RE oxides: A - occupied and unoccupied f-states are located in the valence and conduction bands respectively, B - occupied f-states are located above valence band, unoccupied f-states are in the conduction band, C - occupied f-states are located in the valence band, unoccupied f-states are located below conduction band, D - occupied and unoccupied f-states are located inside the band gap (23)

for TM silicates, as the free energy of formation of the former is about δG $\ll$ -100 kJ/mol as compared to $\delta G \approx -1 - 10 kJ/mol$ for TM silicates(23). The intermediate compounds are not present when oxides are deposited on Ge or GaAs surfaces.

1.2 Physical properties of the $RNiO_3$ system

1.2.1 Crystallographic structure

The correlation between crystallographic structure and physical properties is unequivocally visible among the series of $RNiO_3$ compounds. The size of corresponding rare earth ion influences mutual configurations of atoms in the perovskite-like unit cell of $RNiO_3$ structure thus triggering changes in physical properties (76).

Almost all $RNiO_3$, apart from $LaNiO_3$ (LNO) compounds have an orthorhombically distorted perovskite structure described by *Pbnm* space group (29, 78) in the metallic state. This crystalline structure is observed in compounds synthesized at high oxygen gas pressure. At lower pressures rhombohedral phase is favoured for $NdNiO_3$ (NNO) (95). At the MIT this structural symmetry is low-

ered to monoclinic $P2_1$ space group for heavier RE (Ho, Y, Er, Tm, Yb, Lu), but the distortion is minor and for lighter of the members it is difficult to detect [RT structure - (5, 6, 7, 21, 24, 66), structure at the MIT- (4, 8, 29)]. $LaNiO_3$ compound is the one with the least distortion and its structure is described by $R\bar{3}c$ rhombohedral space group. The distortion is considered with respect to an ideal cubic perovskite structure of for example $CaTiO_3$ aristotype. The distortion is bound to the relative size of the rare earth ion which, if too small, does not sufficiently fill the space in the middle of the unit cell and the cubic structure is destabilized. Based on that, a measure of distortion was formulated by V. M. Goldschmidt and subsequently called *Goldschmidt* or *tolerance* factor

$$t = \frac{d_{R-O}}{\sqrt{2}d_{Ni-O}}. \tag{1.1}$$

For a perfect cubic crystal the factor has a value of one. Relative elongations of the unit cell in any direction will result in a change of distance between Ni-O and R-O, and decrease of the tolerance factor.

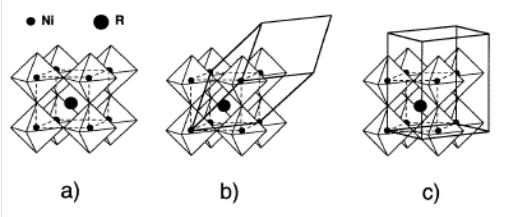

Figure 1.4: Unit cell of $RNiO_3$ crystals - a) perfect cubic perovskite structure (Pm3m), b) Rhombohedral distortion (R3c), c) Orthorhombic distortion (Pbnm) (76)

Considering $RNiO_3$ family of compounds it is generally difficult to stabilize the high symmetry structure(41). The compounds belong to a family of so-called Ruddlesden-Popper phases of oxides of $A_{n+1}M_nO_{3n+1}$ (or $(AO)(AMO_3)$), where n is natural number. Perfectly stoichiometric $RNiO_3$ compounds will correspond to $n = \infty$.

It is very much connected with the difficulty of stabilizing Ni ions in the 3+ oxidation state and the fact that Ni^{2+} state is present in NiO and R_2NiO_4 compounds. This fact will be discussed in subsequent sections.

The overview of the crystallographic structure of whole chain of rare earth nickelates can give a little insight into their electronic properties. At the very beginning Lacorre *et al.* noticed that the size of the rare earth is prominently important considering the metal-insulator transition (66). Lanthanum, the largest

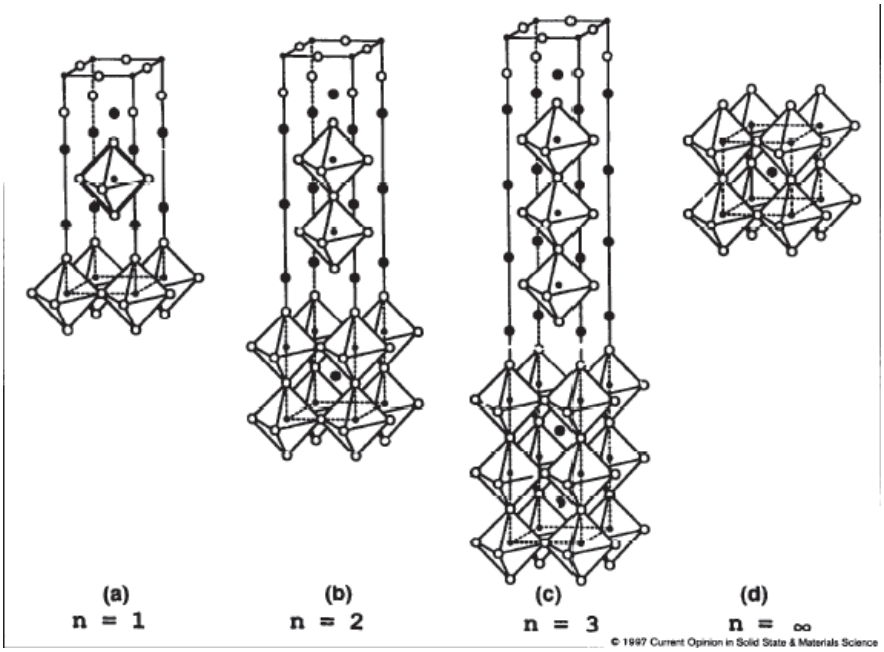

Figure 1.5: Unit cell structure of selected Ruddlesden-Popper phases - Structure for the $La_{n+1}Ni_nO_{3n+1}$ compounds with for n=1, 2, 3 and infinity. Small solid circles correspond to Ni, while medium solid circles to La and open circles to oxygen ions (41)

rare earth, fills the space between eight corner-sharing NiO_6 octahedra in such a way that the distortion is minor, t=0.987 (66), and the structure is rhombohedral. Smaller rare earth ions follow the principle that the smaller the radius, the larger the distortion. It is due to the fact that the smaller R^{3+} cations are not able to sufficiently stabilize the regular configuration of the octahedra which therefore distort in various ways. It results in decreased electronic overlap of nickel ions and increase in the metal-insulator transition temperature. This simple picture was the basis for the investigation of the properties of nickelates.

At the electronic transition there is a slight change of lattice parameters which results in 0.2-0.25% decrease in volume of metallic $PrNiO_3$ unit cell (29, 66). For samarium nickelate the change was estimated to be about 0.15%. Detailed neutron powder diffraction and X-ray diffraction studies of R=Pr, Nd, Sm nickelates revealed that the distortion from cubic structure is mainly related to NiO_6 octahedra that tilt at electron localization (29). The octahedra were found to tilt around b and c orthorhombic axes ($a^0b^+c^+$) (29) which leads to variation of the angles $\alpha = \angle Ni - O1 - Ni$ and $\beta = \angle Ni - O2 - Ni$ (the superexchange angles).

This in turn may coincide with variation of transfer integral between Ni e_g and O *2p* orbitals and allow for electron transfer.

The discontinuous change of unit cell volume implies that the phase transition is of first order type for studied $RNiO_3$ compounds (R = Pr, Nd, Sm). This change is mostly apparent due to abrupt decrease of b and c cell parameters at the transition temperature. However, the total linear expansion coefficient is the smallest for b parameter. For Nd and Pr it was possible to estimate that Ni-O bond lenghts as well as the NiO_6 tilting suddenly increase at the T_{MI} when compounds become insulating. The structural changes do not evidently impose that any change of symmetry occurs. The value of tolerance factor and superexchange angle θ are directly proportional to each other with an approximate relation (29)

$$\Delta\theta \approx 275\Delta t^{\circ}. \tag{1.2}$$

with respect to bond length variation the approximated relation is the following (29)

$$\Delta\theta \approx -275^{\circ}(d_{R-O}d_{Ni-O}^{2}\sqrt{2})\Delta d_{Ni-O}. \tag{1.3}$$

The authors of (29) stated that because no symmetry change is observed at the transition the driving force of the structural changes would be triggered by the electronic localization as a reaction to increased Ni-O distance. Application of Valence Bond Model (VBM) and results of crystallographic investigation revealed that 3+ valence of R and Ni (low-spin), and 2− of oxygen are a very good approximation of the real valence, with the discrepancy equal to about 2%.

The dependence of electronic behaviour with respect to the structure was collected by Torrance *et al.* in a well-known phase diagram(92).

The ∠Ni-O-Ni bond angle increases either with the increasing size of the rare earth ion or with the temperature, that is with the metallicity of the nickelate. As it was said by Torrance *et al.* this is a general steric effect specific for the structure and found for other distorted perovskites as well. The authors do not account it as a driving reason for the metal-insulator transition, in contrast to V_2O_3 where the volume change is significant (3.5%).

Granados and Obradors (36, 82) suggested a coexistence of both metallic and insulating phase over a wide temperature range in the vicinity of the MI transition. This, as no structure symmetry change was observed, was said to be connected with appearance of strain due to volume change. The differences in growth rate of the two phases appears to influence the electronic behaviour. Obradors performing pressure dependent electronic investigation have found an almost linear

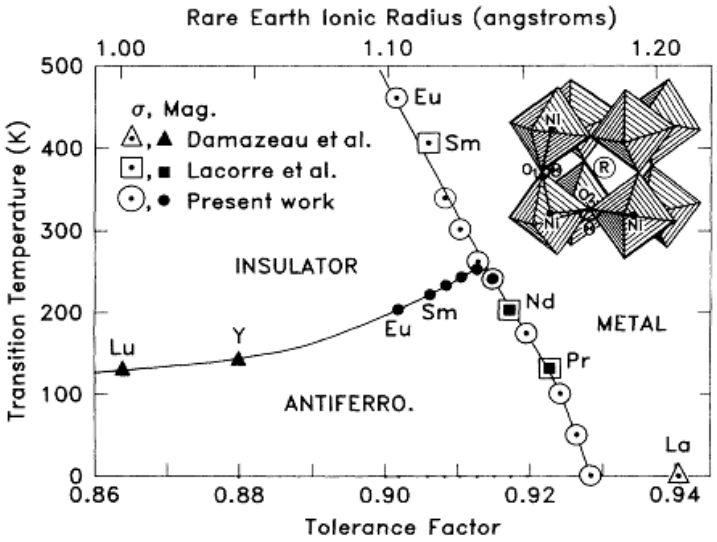

Figure 1.6: Phase diagram of rare earth nickelates - Phase diagram for the $RNiO_3$ family compounds showing Insulator-metal-antiferromagnetic phases as a function of the tolerance factor (or ionic radius) and the temperature (92)

dependence of the transition temperature from applied pressure, regardless of rare earth ion. He suggested a common structural and electronic parameter to control this evolution. With respect to the phase diagram of nickelates one can derive that a similar relation appears between transition temperature and tilting angle of NiO_6 octahedra. This suggests a significant influence of the arrangement of these octahedra. They have also noticed that R-O bond is more compressive than Ni-O bond which influences the tilting angle (82) and therefore its pressure dependence. Before, a decrease of the tilting angle with increasing temperature had been found.

Alonso *et al.* during their investigation of $EuNiO_3$ structure noted that the distortion of $SmNiO_3$ measured by tilting angle is fairly similar (3). They have also compared the tilting angles of nickelates with respect to the rare earth ion and noted a direct correspondence of the angle with the rare earth ion size. Tilting angle was calculated as in (84) as follows

- the tilting angle for rhombohedral $LaNiO_3$

$$\phi = arctg[x(O)\sqrt{12} - \sqrt{3}], \tag{1.4}$$

- the tilting angle for orthorhombic $RNiO_3$

$$\phi = arctg[z(O2)\sqrt{48}], \tag{1.5}$$

where $x(O)$ and $z(O2)$ are coordinates of oxygen atoms at positions $(x, 0, 1/4)$ (xyz) and O2 oxygen atom at position (x, y, z), respectively (3). They have also noticed a progressive increase of Ni-O distance from La to Sm in contradiction to decreasing unit cell volume. Their interpretation of the effect was connected with the charge that is 'kept' in a more covalent bonding of R-O, which would decrease the amount of charge between Ni-O and weaken (lengthen) the bond. Whereas for smaller rare earths, down to Ho, the accompanying reduction of unit cell volume influences the bondlengths more and forces a decrease of Ni-O distance. Using the Brown's valence bond model one can estimate whether there is a correspondence between the Eu-O bond lengths and the octahedra tilting. This phenomenological model describes correlation between bond-length and a corresponding formal valence. In nonstrained crystals the rule of Valence Bond Sum (VBS) is satisfied, i.e. the formal charge of an ion is equal to the sum of the bond valences around this ion. When the stress that is introduced by coexistence of various structural units is not relieved, the VBS rule is a measure of stress existing in the structural bonds. The model enabled to estimate that Ni cations are slightly underbonded and under tensile stress. Whereas Eu ions are overbonded and under compressive stress, which causes the structure to be metastable.

Brown and Shannon have formulated the so-called distortion theorem which states that deviation from of the individual bond-lengths in a coordination sphere, in which the average bondlength is kept constant, will increase the valence sum at the central ion (3). Following the theorem, with any Ni-O bond length change with respect to the average value a distortion of NiO_6 octahedra will be caused due to the trend of underbonded Ni cations to increase their valence.

In a rather different approach Frand *et al.* prepared a series of nickelates with mixture of neodymium and samarium in varying ratio (25). This resulted in obtaining a series of nickelates with monotonically decreasing metal-insulator transition temperature. This indicates that macroscopic variation of the compounds structure (proper distribution of particles or domains of constitutive compounds) may influence the transition temperature and electronic properties. The group also investigated dependence of the properties on grinding time of a chosen compound. They noticed that with the increase of grinding time the phase transition was less pronounced (investigated by DSC measurements) and completely disappeared in the amorphous sample. Annealing in synthesis conditions of the sample "restored" the transition however moderate temperature (400 °C for 16 hours) does not restore the transition.

Influence of structure on electronic properties was also evidenced by room temperature X-ray diffraction measurements. When increasing x in the $Sm_{1-x}Nd_xNiO_3$ series there appears a discontinuous drop in lattice parameters values at $x = 0.45$, and thus unit cell volume. The doping level of $x = 0.45$ is the boundary that divides metallic and insulating $Sm_{1-x}Nd_xNiO_3$ compounds. This variation in a way reflects the temperature dependence of lattice parameters of other nickelates.

No change of crystallographic structure has been observed in case of $PrNiO_3$ up to 4.7 kbar hydrostatic pressure (77). A step-like characteristics of Ni-O distance and Ni-O-Ni superexchange angle was observed with respect to temperature, with the step appearing at the MIT temperature. Reentrant metallic behaviour at low temperatures observed by other groups was suggested by Medarde to be an effect of incomplete relaxation of the system due to different experimental conditions.

The crystallinity of the compounds is highest when a high oxygen pressure annealing is used as a part of synthesis in order to stabilize the perovskite phase (2). Although the authors noted that other techniques using atmospheric pressure can produce nickelates with poorer crystallinity. The group prepared Sr/Th-doped La and Nd nickelates. Incorporation of larger and smaller than La ions into the La nickelate lattice surprisingly resulted in compression and expansion of the unit cell. This was explained by increase/decrease of mean oxidation state of nickel and thus a decrease/increase (opposite) change of Ni-O distance. On the other hand in Nd nickelates the variation of lattice parameters and unit cell volume is non-monotonic which was interpreted as a result of interplay between steric (due to size difference between R and A) and electronic factors (due to variation of Ni-O distances).

In $Nd_{0.95}Sr_{0.05}NiO_3$ the NiO_6 octahedra are flattened in the ab plane due to contraction of Ni-O2ii (by 0.017 Å) and expansion of Ni-O2i distances. At the same time the in-plane Ni-O-Ni angle increases. In $Nd_{0.95}Th_{0.05}NiO_3$ the octahedra are flattened as well however the variation of the Ni-O distances is opposite (2).

Studies done on bulk $NdNiO_{3-\delta}$ with a variable oxygen deficiency δ allowed an observation of the non-stoichiometry influence on Ni-O-Ni bond angles (91). The sol-gel prepared single phase orthorhombic polycrystalline samples had variation in oxygen deficiency from 0.08 to 0.22. The Ni-O-Ni bond angles ϕ and θ estimated by Hayashi method were found to decrease with increasing oxygen deficiency (see table 1.3 and figure 1.7). Hayashi formula for θ:

$$\theta = 135 + \sqrt{13.4(\theta_0 - 135)}, \tag{1.6}$$

where $cos\theta_0 = 1 - a^2/b^2$, and a and b are the orthorhombic lattice parameters.

Table 1.3: Sintering conditions, delta, T_{MI}, lattice parameters and Ni-O-Ni bond angles for various $NdNiO_{3-\delta}$. As presented in (91).

Sintering atmosphere			lattice parameters			Ni-O-Ni bond angles	
	δ	T_{MI}, K	a, Å	b, Å	c, Å	θ, (deg.)	ϕ, (deg.)
7 d, in O_2	0.08	180	5.432	5.431	7.556	157.82	159.86
2 d, in air + 5d, in O_2	0.12	190	5.392	5.430	7.604	155.55	158.47
4 d, in air + 3 d, in O_2	0.15	210	5.390	5.429	7.611	155.49	157.40
7 d, in air	0.20	> 300	5.387	5.428	7.620	155.37	156.36
7 d, in N_2	0.22	> 300	5.383	5.426	7.628	155.26	155.51

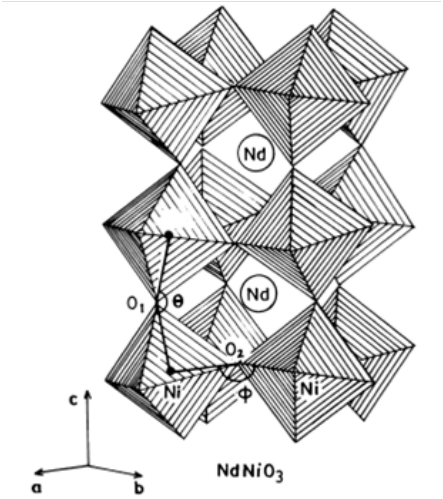

Figure 1.7: The crystal structure of $NdNiO_3$. - The structure of $NdNiO_3$ with distinguished NiO_6 octahedra. The deviation from perovskite structure is small enough to keep octahedral environment of Ni ions, but with Ni-O-Ni bond angles θ and ϕ different from 180° (91)

Such possible change in crystal structure had a clear influence on the electronic properties of the compounds.

1.2.2 Electronic structure

Conductivity of rare earth nickelates has been for a long time the source of interest due to the 'difficult' nature of the so-called metal-insulator transition. This, more of a semiconductor rather than insulator to metal, transition was investigated early by plain resistivity measurements. They have shown a drop in resistance of a few orders of magnitude. A sharply decreasing semiconductor-like resistivity at the MIT is inflected to exhibit the metallic-like character.

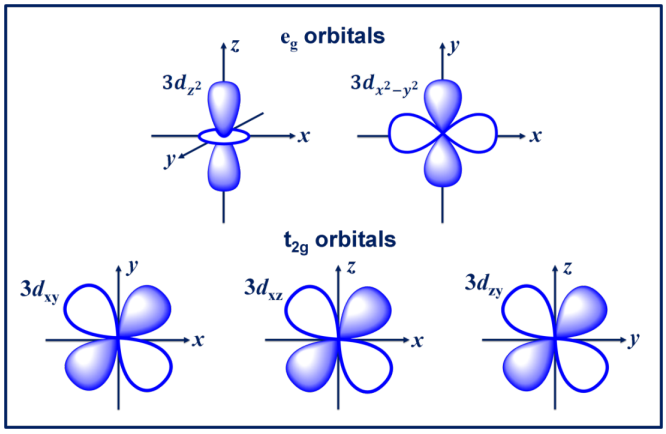

Figure 1.8: Distribution of electronic cloud in e_g and t_{2g} orbitals. - e_g orbitals are symmetric with respect to all x, y, z axes. On the other hand t_{2g}orbitals show symmetry to only one axis for each orbital (51)

It was shown that even rhombohedral $NdNiO_3$ exhibits MI transition with a large hysteresis (95). Qualitatively the behaviour does not change with respect to the 'temperature direction', however a large hysteresis is observed and does not depend on the rate of temperature change (95). What is more, the semiconductor region is not totally homogeneous. Two regions with different activation energy were identified in $NdNiO_3$. The one with higher activation energy was ascribed to a state where the nickelate is an intrinsic semiconductor and when it enters the second region at low temperature - it becomes an extrinsic semiconductor.

Vassiliou investigated the influence of the preparation method on the resistivity of the $NdNiO_3$ to study the effect of grain size. The samples were however polycrystalline and no influence on resistivity of different pressure and temperature conditions were observed. However, he still accounts the crystal structure to be an important factor.

Results of Lacorre et al. show that orthorhombic nickelates (Pr, Nd, Sm) undergo MI transition that is more sharp (few orders of magnitude drop in resistance in comparison with factor of 5 for rhombohedral phase) but the hysteresis is smaller(66).

Based on Bond Valence Model calculations for $RNiO_3$ García-Muñoz et al. suggested a R^{3+}, Ni^{3+} and O^{2-} first approximation of the electronic structure of the compounds. The distances Ni-O also suggested that it is highly unlikely that in these compounds holes are selectively localized on oxygen atoms.

It is also worth to mention the theory formulated by Zaanen, Savatzky and

Allen (ZSA) (99). It has given a straightforward method for the classification of oxides according to the interplay between Coulomb correlation energy U of d electrons and charge transfer energy Δ. Two cases are considered:

(1)when $U < \Delta$ the Mott-Hubbard $d - d$ gap with energy U is formed, with accompanying $d_n + d_n \rightarrow d_{n-1} + d_{n+1}$ charge fluctuations;

(2) when $U > \Delta$ a gap of $p - d$ type with energy Δ is formed, and compound becomes charge-transfer insulator with $d_n + d_n \rightarrow d_{n+1} + d_n L$ electronic fluctuations, along with formation of a hole L on the oxygen atom in the valence p band (28).

1.3 Metal-insulator transitions

Variety of metal-insulator transitions exist due to complicated interplay between various factors (59). In transition metal oxides the factors include the d electron bandwith, Coulomb repulsion, spin-orbit coupling. However the most basic classification is done depending on whether the primary interaction is electron-ion or electron-electron. The first group neglects existence of many electrons and their interaction and consists of:

- Bloch-Wilson (band) insulators,
- Peierls insulators,
- Anderson insulators.

Interactions of electrons give rise to group of insulators of Mott type. Especially important are electron correlations which are the main feature related to appearance of MIT. Few types of transitions in transition metal oxides (TMOs) have already been identified, although this set is not complete:

- Mott or Mott-Hubbard insulator,
- charge-transfer insulator,
- Slater insulator.

The first three appear in compounds with symmetric complexes (62) where crystal field splitting leads to partial lifting of the five-fold degeneracy of transition metal (TM) d states into t_{2g} and e_g degenerate states. The interaction of these

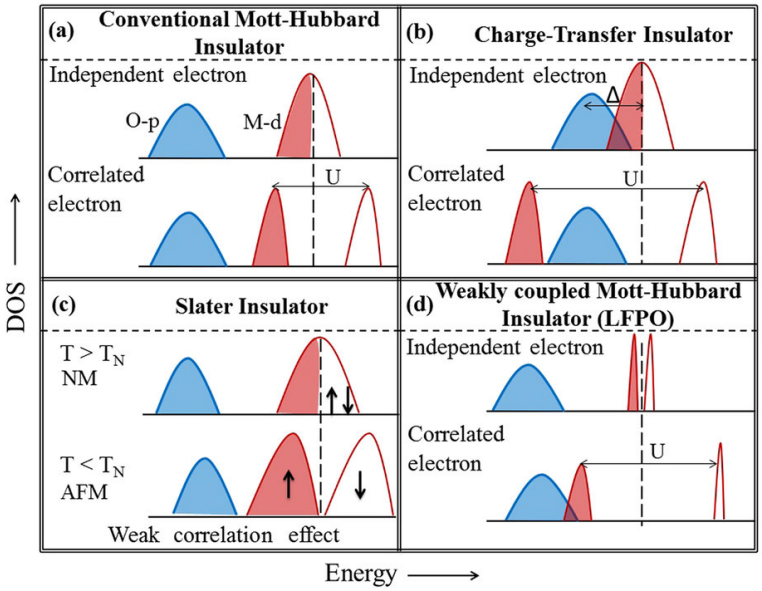

Figure 1.9: Schematic image of main metal-insulator transition types - Dependence of position of ligand p and metal d type bands is related to formation of different energy gaps. Adapted from (62)

electrons with the oxygen p electrons together with electronic correlations result in a metallic or insulating stare.

The last one is related to interaction of electrons in terms of their spin which move under different potential below Néel temperature (T_N). This applies to TM compounds whose d electrons are often weakly localized. Below the T_N the electrons that have opposite spins are stabilized by the AF ordering. The gap opens between electrons of opposite spins, while the Brillouin zone is reduced twice.

In the Mott transition only one-electron atoms are considered. The electrons are said to feel the electrostatic potential of crystal lattice which changes depending on their density in the solid state. The change in the electron density either caused by temperature or pressure induces the metal-insulator Mott transition. When the electron density is sufficiently small, smaller than a critical density, the material is an insulator. In other words, in the opposite - when the distances between atoms are sufficiently large, larger than critical distance a_0, the material is an insulator (at zero temperature). The distance must not be too large as tunnelling would be prevented. In that situation electrons are enough far apart from each other to feel only the attracting force of the positively charged nucleus.

However, when the become closer due to decrease of the interatomic distances - they for once start to feel strong repulsion from other electrons, due to Pauli principle, and stop feeling the electrostatic force from the positively charged lattice site as the force is screened by the proximity of the other electrons. As estimated by Mott, the critical density N at which the transition occurs is approximately equal to

$$N^{1/3} \approx \frac{0.2}{a_B}. \tag{1.7}$$

The formal treatment of the Mott transition was first given by Hubbard. He introduced a Hamiltonian which takes into consideration the basic tight binding approximation of band theory together with the onsite Coulomb interaction between electrons. The two terms in second-quantized version give in total:

$$H = -t \sum_{<i,j>,\sigma} (c^{\dagger}_{i\sigma} c_{j\sigma} + c^{\dagger}_{j\sigma} c_{i,\sigma}) + U \sum_{i} n_{i\uparrow} n_{i\downarrow} = H_t + H_U \tag{1.8}$$

The model, although considering still only electron in a single band, gives a good description of some materials.

In the Mott-Hubbard model the hopping of electron occurs only between the metal sites. In transition metal oxides it involves a transport of electron between d electron sites $d_i^n d_j^n \rightarrow d_i^{n-1} d_j^{n+1}$ between i and j transition metal sites. However some researchers indicate that the fluctuations are very high in energy as they require energy about 7-10 eV (for late TMs (99)), so highly improbable in some compounds. The transition occurs due to thermal fluctations. At the transition the gap between lower (LHB) and upper (UHB) Hubbard bands is closed.

The Mott-Hubbard picture explains the insulating state well but can not describe the quasi-particle peak that appears at the Fermi level in the metallic state. This state is addressed in Brinkman-Rice model assisted by Gutzwiller wave functions. This results in electron effective mass, electric susceptibility and specific heat enhancement (divergence) close to the MI transition which is according to experiments (47). The insulating state occurs for strong electron correlations with a half filled band. The occurrence of both Hubbard bands are not explained within the theory.

A different situation is considered in so called charge-transfer insulators where electron moves inside the unit cell from the ligand (anion) to the metal site. It is described by $d_i^n \rightarrow d_i^{n+1}\underline{L}$. The energy involved is denoted as δ and is related to the electronegativity of anion and Madelung potential.

The above pictures do not take into account the magnetic properties of electron, they even do not regard spin as a factor in MIT. In Slater theory of MIT the

transition is strictly connected with thermal fluctuations that destroy magnetic ordering. In the ground state, a Slater insulator consists of two sublattices with single-band described by Hubbard model - one s-electron per site. The atoms in sublattices ararranged in ABABABA... mode and are antiferromagnetically (AF) coupled. This and the repelling interaction of electrons lead to spins are arrangement of $\uparrow, \downarrow, \uparrow, \downarrow, \uparrow, \downarrow, \uparrow$... Such self-stabilizing spin density wave leads to doubling of the unit cell and halving of Brillouin zone, formation of energy gap and the system being an insulator.

As the thermal fluctuations increase with temperature the local arrangement of electrons becomes destroyed and at the critical point of Néel temperature a simultaneous magnetic and MI transitions occur because the thermal energy is comparable to the coupling energy.

Dynamical mean field theory (DMFT), as opposed to presented model, takes into account quantum effects, but neglects spatial fluctuations. The solid state is described as an effective medium, a self-consistent bath which contains all information on the interactions between atoms with a single atom, an impurity, embedded into it. The information is described by a single-particle spectral function $\Delta(\omega)$. A single-impurity Anderson model is built (detail found in (32)):

$$H_{SIAM} = \sum_{k,\sigma} [\epsilon_k a^\dagger_{k\sigma} a_{k\sigma} + V_k (a^\dagger_{k\sigma} c_{0\sigma} + h.c.)] - \mu(n_{0\uparrow} + n_{0\downarrow}) + U n_{0\uparrow} n_{0\downarrow} \qquad (1.9)$$

The Hamiltonian contains, reading from left, non-correlated electronic levels of medium, coupling of the impurity with the medium, electron-electron interactions. The hybridization parameters are the DMFT model parameters ϵ_k and V_k.

The single-particle spectral function should represent all ways than electron can travel (tunnel) from site to the medium and back. In an insulating state the function has a gap that closes at the MIT so it is taken as a order parameter for the Mott transition. Advantages of DMFT include a correct description of Fermi liquid, high-temperature behaviour of materials where spatial fluctuations are not important and correct position of quasi-particle peak in experimental spectra though the width is underestimated. The model has ability to describe very well certain materials close to Mott transition - clean systems, some TM oxides, heavy fermion materials and Kondo insulators. However for materials where spatial fluctuations are strong and important, and for explaining some physical quantities near critical point the model is not suitable.

1.3.1 Magnetism and metal-insulator transition

Magnetism seems to be an important factor in understanding MIT in RE nickelates. In $NdNiO_3$ Vassiliou obtained temperature dependence of susceptibility similar to a Curie-Weiss behaviour. They also noted that it is not strictly the behaviour as the Curie-Weiss constant is temperature dependent due to variation of crystal field, as in other Nd oxides. Depending on the selected temperature interval the results were as follows:

- 80 K to 300 K: C = 6.53 × 10^{-3} emu·K/g, T_c = 32 K, and X_0 = 2.48 × 10^{-6} emu/g,

- 120 K to 300 K: C = 7.24 × 10^{-3} emu·K/g, T_c = 44 K, and X_0 = 1.02 × 10^{-6} emu/g.

Magnetic moment per Nd atom is respectively 3.6 to 3.8 Bohr magnetons as compared to theoretical 3.62 for free Nd^{3+} ion. The results do not even support assumption of additional existence of magnetic g=2 S=1/2 Ni^{3+} ions (95). No distinct changes in susceptibility temperature behaviour was observed around the T_{MI}, while in inverse susceptibility a departure of linear behaviour in lower temperatures was evident.

Garcia-Munoz (29) discovered that in $RNiO_3$ there is a magnetic superstructure with a propagation vector $k = (1/2, 0, 1/2)$ which corresponds to magnetic unit cell of 2a × b × 2c. The nuclear scattering processes were not found to contribute to the reflections from neutron diffraction.

Some estimations and considerations were done for magnetic contribution to entropy change at the transition (36). By assuming that all Ni^{3+} spins order at low temperature the contribution to the entropy change from the magnetism would be $\delta S_M \approx -5.7 J/molK$ which is in great contrast with the experimental estimated value of total entropy change $\delta S_{TOT} = -1.73 J/molK$ for $SmNiO_3$ for example. On top of that a similarity in the experimental values of total entropy change for SNO and NNO would suggest that magnetic contribution is not significant to the phase transition. However, this would be different if magnetic correlations existed above T_{MI} or if the magnetic moment did not reach its saturated value.

1.3.2 Metal - insulator transition - explanations

Before a description of the transition itself a few models for description of electronic conductivity will be given. In MIT transitionin $RNiO_3$ compounds the correlation between nickel 3d and oxygen 2p electrons plays crucial role (97).

The $NdNiO_{3-\delta}$ oxygen deficient compounds have shown a great difference in temperature dependence of resistivity with respect to their non-stoichiometry(91). The almost stoichiometric $NdNiO_3$ had the lowest MIT temperature (180 K) and a significant hysteresis in resistivity curve with a resistivity on heating larger than that on cooling. For deficiency of over 0.2 no transition was observed up to 300 K. The metallic regime was corresponding well to linear dependence of resistivity which was attributed to electron-phonon scattering mechanism.

In relation to Zaanen, Sawatzky and Allen theory(99) the authors of (91) tried to explained the low temperature behaviour of deficient $NdNiO_3$ compounds. While the stoichiometric $NdNiO_3$ was said to show activated behaviour below 200 K (based on Zaanen), the deficient compound did not fit the theory. $NdNiO_{3-\delta}$ did not fit well the activated transport equation:

$$\sigma = \sigma_\infty exp[-\frac{T_0}{T}]. \tag{1.10}$$

where σ_∞ and T_0 are constants; neither Variable Range Hopping (VRH) conductivity

$$\sigma = AT^{-1/2} exp[-(\frac{T_0}{T})^{0.25}]. \tag{1.11}$$

where A and T_0 are constants. Instead, an empirical relation was found

$$\sigma = \sigma(0) + AT^m. \tag{1.12}$$

here $\sigma(0) > 0, A > 0, m \approx 0.3 - 0.4$ to fit very good the low temperature experimental data. A non zero 0 K conductivity was attributed to be the result of an incomplete phase transition where a metallic phase exists down to very low temperatures and contributes to conductivity. An increase of this 0 K conductivity with the increase of oxygen concentration was found. Authors concluded that this is because of increase of residual metallic phase. The parameter 'm' was found to be similar to observed in highly disordered metals, as if the insulating phase made the mixed in metallic phase disordered.

Other models of electrical conductivity at low temperatures include:

- thermally activated Arrhenius law

$$\sigma(T) = \sigma(0) exp(-E_a/k_B T) \tag{1.13}$$

where k_B is Boltzmann constant and activation energy E_a is 22 meV for $PrNiO_3$(35) (for low-T data below 100 K), and 25-28 meV for $NdNiO_3$ (36). However at lower temperature this energy increases slightly. Which is corresponding to rapid increase of the semiconductor-like bandgap.

The hysteresis in thermal dependence of resistivity in $PrNiO_3$ was explained as a gradual transition from metallic to insulating phase. The transition occurs between 130 K (T_{MI}) and around 74 K. Between 130-102 K a metallic matrix with nonmetallic inclusions is present, and between 102-74 K is more transitioning to nonmetallic matrix with metallic phase inclusions. This behaviour was consistent to the first-order character of the transition. The Seebeck coefficient measurements indicated that in both states the majority of carriers are of electron character(35).

For bulk $NdNiO_3$ the found hysteresis was from about 130 K to MIT at 205 K(36). The Seebeck coefficient measured for high temperatures is negative and has a small absolute value of about 22 μV/K at 205 K which indicates a typical metallic state with electron-like charge carriers. The Seebeck coefficient was used to determine the Fermi energy, with using the relaxation time approximation

$$S(T) = -\frac{\pi^2 k^2}{3e} T[\frac{g(\epsilon)}{n} + \frac{\partial}{\partial \epsilon} ln(\tau(\epsilon))\Big|_{\epsilon=E_F}], \tag{1.14}$$

with $g(\epsilon)$ being density of states, n - charge carrier density, E_F - Fermi energy, and $\tau(\epsilon) \sim \epsilon^\alpha$ - energy-dependent relaxation time, with α corresponding to scattering mechanism. Another assumptions included parabolic band and for the case in article the $\alpha = -1$. This lead to a Drude model relation of the Seebeck coefficient

$$S(T) = -\frac{\pi^2 k^2}{6e} \frac{T}{E_F}. \tag{1.15}$$

For the metallic region, the estimated Fermi energy was found 0.41 eV for NNO, 0.4 for PNO and 0.21 for LNO. Typical metals have a higher Fermi energy - for example Cu 7 eV and Au 5.5 eV (63). But the energy is also higher if the relaxation time is energy independent. Here as well, at low temperatures the Seebeck coefficient was negative suggesting that the majority of carriers is electron-like. However below 110 K its absolute value decreases that for the authors was an indication that dominant mechanism is not semiconductor-like or that some regime of charge compensation is present. The characteristic temperatures of the coefficient's temperature dependence are a bit shifted as compared to resistivity. For Both quantities, on heating the absolute values are greater than on cooling.

Additional characteristics of electronic structure were estimated as well based on the measurements. Density of states at the Fermi level $g(E_F)$ was estimated by assuming

- a parabolic band,

- one electron per Ni atom with the electronic configuration of Ni^{3+} ions being $t_{2g}^6 e_g^1$
- cell volume $V_c = 220$ Å^3
- carrier number $n \approx 1.8 \times 10^{22}$ cm^{-3}

and obtained $g(E_F) \approx 6.5 \times 10^{22}\ eV^{-1}cm^{-3}$ for NNO. DOS calculated for free electrons was $g^0(E_F) \approx 1.08 \times 10^{22}\ eV^{-1}cm^{-3}$. The ratio of both was said to be a measure of the effective electron mass to the free electron mass $m^*/m_0 \approx 6$. This value is similar the the values obtained for LNO. Specific heat was also predicted to be about 8.2 $mJ/molK^2$. It was inversely checked with the data for Seebeck coefficient of LNO which suggests some similarities and maybe support the picture of Fermi gas.

Authors state that the estimates should be different if the metallic state is obtained by the closing of charge-transfer gap, because therefore there should be less than one conduction electron per nickel site.

Granados argues with the model of Torrance of the metal-insulator transition that the gap of charge-transfer character closes with the overlapping of the Ni3d and O2p bands(92). Within the model that overlap would increase with temperature which would be associated to an increase in the carrier number with temperature in the metallic state. However the temperature data of Seebeck coefficient and resistivity of $NdNiO_3$ (36) does not support this expectation as both quantities show a linear dependence with temperature. An electronic conduction in a single band would overcome these troubles although the origin of that would not be easy to explain.

They have estimated as well the pressure dependence of transition temperature to be -5.4 $K/kbar$ through the use of Clausius-Clapeyron relation which agreed greatly with the experimental value of -4.2 $K/kbar$ for all nickelates.

Assuming the two different species in the volume a combination of two simultaneously acting transport mechanism was made. One is VRH and the other an activated behaviour. The VRH is supposed to be limited for high temperatures by $E_m = kT\xi_m$ where E_m is maximum energy difference between the Fermi level and the localized states involved in hopping and ξ_m is exponent of critical percolation impedance in a random network. However it was shown that in percolative systems the hopping mechanism is more occurring in sites that are closer to Fermi level than E_m so it was not considered a true limit. On top of that electron-phonon coupling which is assumed to play significant role in the conduction of nickelates, supports VRH.

The full semiconducting state is modelled well by this combination

$$\sigma \propto 1/R = Aexp(-B/T^(1/4)) + Cexp(-D/T). \quad (1.16)$$

A, B, C, D being constants.

Vassiliou gave several possible interpretations of the obtained data for $NdNiO_3$. One of them considers $NdNiO_3$ to be a Mott-Hubbard insulator. The RT half-filled metallic d-band is at the antiferromagnetic transition split into two band - one fully filled and the other one empty. The band gap emerges from this splitting. No antiferromagnetic transition is visible in susceptibility data as the paramagnetic (PM) signal of f-electrons in Nd^{3+} ions is strong enough to mask it.

Second explanation involves considering polaron formation below the MIT temperature. Room temperature conductivity of $NdNiO_3$ is above the minimal value for metals of $10^3(\Omega \cdot cm)^{-1}$. A value still so low that the mean free path of electrons is of the order of interatomic distances. With the electrons moving in a diffusive way in the narrow d-bands, the conductivity of the compound is also diffusive. The width of the d-band W would be given by uncertainty principle $W = h/t_s$, where t_s is the relaxation time. Below 130 K the localization of the electrons occur due to polaron formation, which changes the metal to semiconductor. In this state, the charge transfer is realized by the phonon-assisted hoping of the electron from site to site, and thus the relaxation time is limited by this process. A possible Jahn-Teller distortion accompanies the 3d electron localization. The hysteresis of resistivity may be an effect of hysteresis of lattice distortion.

The *ab initio* calculations revealed how DOS of the NNO thin films is influenced when strain is applied or when the film is confined along z direction(97). While compressive or tensile strain is applied by the substrate the 3d nickel orbitals become delocalized in contrast to bulk NNO. In bulk NNO the band gap forms between occupied Ni2 t_{2g} states and unoccupied Ni2 e_g states but also e_g states of both Ni1 spins. In case of confined film, there is a van Hove singularity that creates dips in Ni ions DOS and this increases the band gap. There is also a non-zero spin-polarization of Ni1 sites.

1.4 Influence of the reduced dimension on the physical properties

The crystal structure defines most of the properties of thin film materials. In NNO thin films deposited on various substrates show different structure and orientation of crystallites which involves the variation of electronic behaviour of the material

(14). A large film-substrate mismatch of 10.2% that appears on MgO(100)-grown NNO results in poor crystallinity 110 and 200 pseudocubic reflections with mostly random and partially preferential orientation, as confirmed by Selected Area Electron Diffraction(SAED) in Transmission Electron Microscopy (TEM). The lattice mismatch is much smaller for other perovskite-like substrates - less than 3%. This yields a better crystallinity and a preferential orientation matching the substrate - in that case 100 pseudocubic orientation. A doubling of the unit cell in-plane matching c axis of $NdGaO_3$ (NGO) was noticed. On MgO films grow incoherently and on other substrates coherently or semi-coherently.

Analysis of transport behaviour has shown that in the NNO films grown by PLD resistance jump and normalized resistance slope are closer to bulk behaviour when the lattice is smaller (14). The film deposited on MgO did not reveal any transition but a semiconducting behaviour in the studied temperature range. On the other substrates the T_{MI} was lower than in bulk.

There was a marked difference in the electrical resistivity vs. temperature curves and the quality of metallic state for films of different thickness. The weakest metallic state was observed for films on $SrTiO_3$ (STO), where the quality decreased with lower thickness. In general T_{MI} decreased with the film thickness decrease. The investigated $-d(lnR)/dT$ against temperature curves have revealed some maxima corresponding to MIT. Double maxima for thick films were probably corresponding to transitions in different regions of the film - close to the substrate dislocation free region and further from the substrate with smaller epitaxial strain relieved by occurring dislocations. The critical thickness that divides the two regions is given by Mathews-Blakeslee formula

$$\epsilon_m = \frac{[b_x^2 + b_y^2(1-v)b_z^2]}{8\pi(1+v)b_x}\frac{1}{t_c}ln\beta\frac{t_c}{r_0}. \tag{1.17}$$

where r_0 is the pseudocubic perovskite lattice parameter of the film, (b_x, b_y, b_z) is the Burgers displacement vector of the dislocation, v - Poisson ratio of the film, b is a dimensionless constant, and ϵ_m is the lattice mismatch between substrate and film. Typical values for perovskites are $v = 1/4$ and $\beta \approx 4$. Perovskite films on perovskite substrates usually show dislocations with pseudocubic $< 100 >$ Burgers vector (26, 68, 74). However the values obtained from this formula are an order of magnitude smaller than the values obtained from resistivity curves.

Some theoretical works have shown that structure of surface is important in consideration of electronic properties. In $LaNiO_3$(001) thin films the influence of several types of termination was studied (44). For both NiO_2 and LaO termination

an inward relaxation of topmost layers was found. However within the terminating layer the atoms behave differently. In LaO layer - O atoms relax outwards and La atoms opposite. While for NiO_2 slab the O atoms relax inwards and Ni atoms opposite. The calculated Mulliken charge transfer indicates that there is a change of bondlengths. For La the charge is reduced from $1.58e$ down to $1.30e$ with a probable elongation of La-O bond and weakened interaction. In NiO_2 terminated surface the Ni charge increases from $0.48e$ to 0.65 e which could indicate an increase contribution of Ni$3d$ electrons to electronic transport at the surface. It is reflected in calculations by increased density of states (DOS) at the Fermi level in comparison to LaO terminated surface.

Calculations of surface energy and DOS of unrelaxed, atomically relaxed and fully relaxed surfaces were done(44). It was found that within the full-relaxed surfaces LaO_3 and all Ni containing terminations like NiO_2, LaNiO, Ni, have higher surface energy than LaO termination which was 0.7 eV. The authors assumed nominal charges for the ions to discuss the polarity influence on surface stability. With these assumptions the LaO and NiO_2 terminated surfaces have a polarities of +1 and -1, respectively. An attempt to investigate the polarity effect was made. The authors claim that a surface constructed by removing 50 % of the atoms should be non-polar. For such surfaces the DOS indeed different shape, which authors contribution to polarity suppression and contribution of uncovered stated of a sublayer.

1.4.1 Crystallographic structure of $SmNiO_3$ thin films

Growth conditions play a huge role in 'inducing' crystal structure guaranteeing phase stability of thin films. Approximate analysis of thermodynamic trends was carried out based on Gibbs free energy of formation of SNO (61)

$$\Delta G = \Delta H_{LNO,1000K} - T\Delta S_{LNO,1000K} + h(r(R^{3+})) - r(R^{3+}) - (1/4)RTln(P). \tag{1.18}$$

LNO stands for $LaNiO_3$, R is the ideal gas constant, and the last term accounts for variable oxygen pressure P. The obtained calculated diagram indicates that the stability of films is best if they undergo extreme annealing at high temperature and pressure. However for typical (p $<$ 800 μbar T $>$ 800K) perovskite thin films growth conditions are insufficient to bring a phase stability.

For radio-frequency (RF) magnetron sputtered films as-grown (13 mbar (10 mTorr) total pressure, 80/20 sccm Ar/O_2 gas flow, 200 W, and 470 K) or annealed at 620 K in 100 bar O_2 - there were no peaks of film in diffraction patterns, only

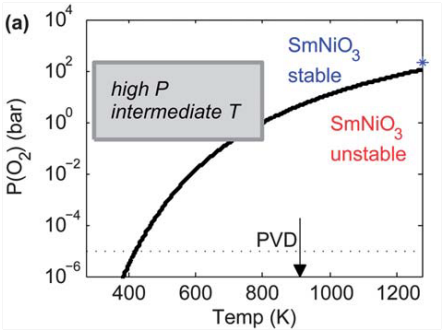

Figure 1.10: Stability of $SmNiO_3$ - Thermodynamic stability of $SmNiO_3$ (61)

amorphous halo and substrate contribution peaks(61). Therefore for the annealed films and conditions no conclusions were drawn whether there are any thermodynamically stable phases. At 770 K and in air annealed films there were found textured Ni_2SiO_4, Sm_2O_3, and polycrystalline Sm_2SiO_7 and α-quartz SiO_2. As a result of application of pressure of 10 bar O_2 no silica, silicates or NiO were found but polycrystalline Sm_2O_3. However the Sm:Ni ratio being close to 1 indicates presence of very nanocrystalline or amorphous NiO. A film annealed at 770 K, 100 bar O_2 for 24 h shows polycrystalline $SmNiO_3$. In all of the samples some amorphous halo is present. For the ratio Sm:Ni further away from 1 there appears a phase segregation, impurity phases (Sm_2O_3) and large crystallites appear on the film surface. The authors underline the importance of proper stoichiometry in the final films.

From thermodynamical point of view high pressure and proper stoichiometry seems to be crucial for phase stability and good properties of the films.

The diagrams are in agreement with the results of work by Tiwari and Rajeev (91). However the diagrams are limited by not considering interfacial reactions (oxidized substrate is ok as should be somehow inert during processing) and not considering mesoscopic effects that in general influence thermodynamic properties.

The LNO thin films were deposited by spin coating on Si, STO and $LaAlO_3$ (LAO) (001) substrates and subsequently annealed (55). Films on Si were polycrystalline and on STO and LAO were strained epitaxial. Insufficiently high temperature (below 500 °C) did not let the perovskite phase to crystallize while too high temperature (700 °C and higher) enabled formation of proper phase but with some impurity phases. High temperature also caused reduction of Ni3+ ions, decrease of oxygen amount and formation of oxygen vacancies. It was confirmed by

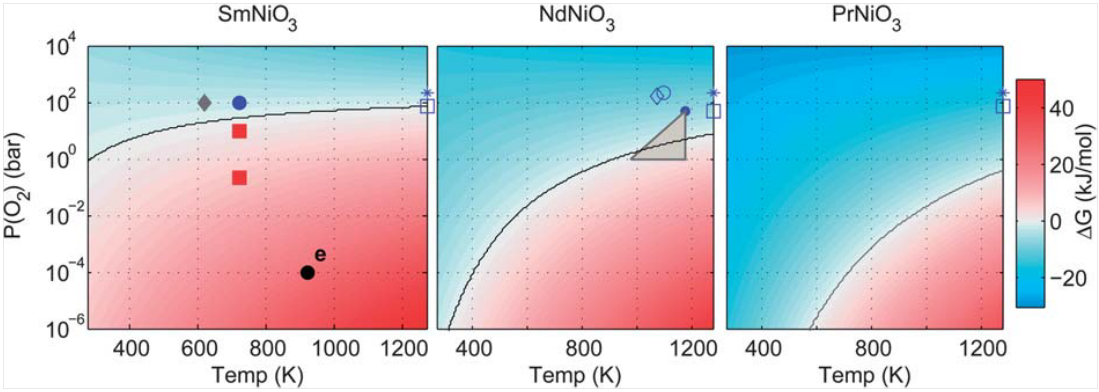

Figure 1.11: Predicted updated diagram for thermodynamic phase stability of selected $RNiO_3$ compounds - (a) $SmNiO_3$ - Annealing conditions leading to $SmNiO_3$ are indicated by the solid blue circle, conditions leading to other phases are indicated by solid red squares, and conditions that did not produce crystalline phases are indicated by the grey diamond. Black line is the calculated locus for molar Gibbs free energy of formation of RNO from binary oxides δG=0. (b) $NdNiO_3$ - Grey triangle represents the conditions used to synthesize $NdNiO_{3-x}$; blue circle represents the most nearly stoichiometric sample with x=0.08. (c) $PrNiO_3$. δG in diagrams has values corresponding to the color scale on the right with systematic error of approximately $\pm$5kJ mol^{-1}. Points placed in thediagrams indicate conditions reported in cited references. As presented in (61)

an increase of lattice parameters and change of resistivity. The crystallographic misfit of film and substrates forced a tetragonal distortion in the films and the lattice parameters values between bulk LNO and substrate. This in turn, as the authors stated, may have affected the different oxygen stoichiometry in films of different strain with compressive strain allowing more oxygen in the structure and smaller unit cell. There was a noticeable difference in resistivity vs. temperature curves. Going from rom LAO, Si, STO - i.e. from compressive strain of epitaxial film, through polycrystalline film with little strain to tensile strained film - an increase in resistivity below room temperature is observed. And also an increase in temperature of transition from metallic to insulating. Authors gave two possible causes of this resistivity 'ordering'. A limited influence of strain that could affect out-of-plane Ni-O-Ni bond angle and therefore the electronic bandwidth which increases with the angle. For compressive strain the angle is higher and for tensile it is lower than in the bulk. As a second reason for increased conductivity authors pointed at the influence of oxygen vacancies. The more compressive strain, the

more oxygen and less oxygen vacancies which increases bandwidth anch charge carrier number and therefore conductivity. The R-T measurements were done in vacuum and grazing incidence X-ray diifraction (GIXRD) after confirmed that there was a phase change from LNO to LNO(2.5) due to oxygen loss. Polycrystalline film on Si were losing oxygen much faster than the epitaxial films. And films on STO were losing oxygen slower than on LAO probably due to extra vertical pressure from tensile strain which forbid a quick escape of oxygen (55).

SNO/LAO films deposited by RF magnetron sputtering and on the same substrate not only experience about 15 % compressive strain but also exhibit different out-of plane unit cell parameters (50). The parameters increase with decreasing deposition pressure which is said to be an effect of varying stoichiometry. The lower pressure results in reduction of oxygen content and lower oxidation state of nickel ions which instead of 3+ are rather closer to 2+ and therefore having larger ionic radius and bigger unit cell. The higher pressure should therefore be necessary to stabilize Ni3+ state. The 250 mTorr film grow "cube-on-cube", with (113) pseudocubic reflection of SNO aligned with LAO(111) reflection as seen on the ϕ scans. The film is also very smooth, with a low RMS roughness of about 5Å.

1.4.2 Electrical resistivity

For SNO films annealed in different temperatures and pressures it was found that the higher the oxygen pressure the higher the conductivity (61). High temperature and low pressure inhibit appearance of metal-insulator transition. For 770 K and air-annealed films are strongly resistive, 770 K and 10 bar O_2 are semiconducting while 770 K and 100 bar O_2 have a reversible transition with $T_{MI} = 400K$ like in bulk. The authors indicated that such a temperature for a film is characteristic to unstrained and polycrystalline films. The stoichiometry-deviated films undergo a non-reversible MI transition which the authors attributed to unstable phases and loss of oxygen during cycling.

Low temperature and high pressure result in a hysteretic MI transition which is not repeatable in subsequent cycles. It has been shown that the deposition pressure influences greatly the electrical behaviour of SNO films (50). The insulating state is favoured with the low- and high-pressure deposited films, while metallic was seen for moderate pressures. The low pressure sample exhibits a transition in R(T) curve with a shift/increase in resistivity unrecoverable when returning to lower temperature, presumably due to permanent oxygen loss. The metallic phase

is not stable in such film. In the 190 mTorr-deposited films there is no observable transition and the film is reversibly metallic throughout 100-420 K temperature range. The R(T) relationship is linear which may indicate the electron scattering is the primary source of temperature dependence. Also, very low T_{MIT} can be explained by the presence of high amount of donor defects from oxygen vacancies and oxygen reduction. The defects are located in the bund gap greatly enhancing the conductivity. Sample deposited at 250 mTorr have a bulk-like stable and reversible $\rho(T)$ characteristics wih a MIT at about 400 K. The observable unit cell expansion may influence the reduction of distortion of NiO_6 octahedra and lower MIT as analog in $RNiO_3$.(50)

Typically, the MIT temperature for the $RNiO_3$ is determined by 2 methods. In first method, one could give the position of the $d(ln(r))/dT$ peak as the MIT temperature. This corresponds to the point, where the change in the resistivity is steepest. Second method is closer to the MIT definition. It is based on finding the temperature, where the sign of the dr/dT changes, thus insulating behaviour (negative dr/dT sign) changes into metallic (positive dr/dT sign) (50). For 250 mTorr the temperatures are 316 and 405 K respectively, and show a little hysteresis (2 K) as opposed to bulk (20 K). It is possible that any non homogeneous local strain resulting from mechanical and chemical defects in thin films, broaden the phase transition and increase the range of temperature with a possible coexistence of metallic and insulating phases.

A small kink in resistivity appears close to antiferromagnetic Néel transition. There is observable variation of the resistivity slope and the MIT transition temperature for films deposited with temperatures above 190 mTorr (225) up to 400 mTorr. With the pressure increase the transition becomes more abrupt (up to 3 orders of magnitude) and the transition temperature increases from 405 K to 440 K.

Two types of film were deposited by RF magnetron sputtering - $SmNiO_3$ on Si(100) or LAO(001) for - out-of-plane and in-plane devices respectively. The films were not subjected to any kind of annealing. Films on LAO are -0.15 % compressed, epitaxial and single phase(49). The films on LAO were found to be fully strained with the in-plane parameters equal to LAO. 80nm film experienced contraction of out-of plane parameter, higher Ni3+/Ni2+ XPS ratio and lower MIT temperatures in comparison to thicker 200 nm film on LAO. This was attributed to lower concentration of oxygen vacancies in thinner film. The transition temperature and resistance itself are subject to number of heating-cooling cycle and gradually increase with further cycles. T_{MI} is 85 °C at the beginning but 155

°C in the fourth cycle. The resistance ratio RMI/R(25 °C) increases as well from 1.02 to 1.25 for 80 nm film. It is even higher for 200 nm film. However, as noted down, when the cycling temperature does not exceed the transition temperature, resistivity does not increase significantly while cooling. This indicates that irreversible changes occur for the films during the metal-insulator transition. The changes are thought to be due to gradual increase of oxygen non-stoichiometry (oxygen loss) with subsequent cycles. The variation between films of different thickness are additionally bound by epitaxial strain influence which could affect Ni^{3+} state. For 200 nm film the T_{MI} is higher than in the bulk.

Similar increase of T_{MI} was observed together with increase of oxygen deficiency in $NdNiO_3$(91), therefore indeed the mechanism could be similar. Film on Si was a multi-phase with addition of SmO, NiO, NiO_2, Ni_2O_3 and Sm_2O_3. In Ni 2p XPS spectra of the film mostly Ni^{2+} peak was present with a little contribution of metallic Ni. For the film a similar cycling behaviour was observed. The change in resistivity was permanent within weeks time.

At high temperature but below MIT (300 - 430 K) the resistivity of SNO/LAO epitaxial films produced by RF magnetron sputtering was found to fit well the Arrhenius law with the calculated activation energy of 170 meV(48). Such a fit suggests that the conduction mechanism is thermally activated hopping between defect sites (ref 3-5,9 in (48)). The inclusion of VRH was not important enough to improve the data fit.

For polycrystalline films the transition occurred at 440 K, the activation energy of the multiphase film was ∼270 meV and the resistance at insulating phase also fit the Arrhenius law.

The theory behind the activation energy is indispensably related to number of donors and acceptors. For lightly doped p-type semiconductors the hopping activation energy is well approximated by following relation

$$E_{a1} \approx \frac{e^2 N_A^{1/3}}{4\pi\epsilon}(1 - 0.3K^{1/4}). \tag{1.19}$$

$K = N_A/N_D$ being a measure of compensation, N_A, N_D - acceptor and donor concentration. The relation is a difference between Fermi level and (now non-ionized) acceptor levels. This relation is valid for materials with $K \ll 1$ which then does not hold for materials which for example have a significant amount of oxygen vacancies. And oxygen vacancies behave as electron donor defects which provide the electrons for acceptor sites. In this case the compensation parameter slowly approaches 1. The Fermi level is shifted between filled acceptor (ionized)

levels and empty donor levels. For this case the activation energy is given by

$$E_{a2} \approx \frac{e^2 N_A^{1/3}}{4\pi\epsilon(1-K)^{1/3}}. \tag{1.20}$$

This was shown to be consistent for epitaxial thin films assuming coarsely that the contribution of oxygen defects to activation energy is large (48).

Type of conduction is dependent also on the level of electric field applied. A power law dependence appears for example for space-charge-limited conduction (SCLC). A power of 2 indicates that conduction is described by Mott-Gurney law and the insulator does not contain trap states. Higher power suggests that SCLC is trap-limited. Both dependencies were observed in epitaxial SNO - a linear behaviour for low fields (below 1 V voltage), and trap-limited for higher voltages (48) with the power law dependence about 3. In polycrystalline films the exponential power was about 8-14 for high field (more than 0.4 V) but again 1 for lower field.

The trap-limited conduction in a p-type semiconductor is described by a relation derived by Mark and Helfrich:

$$J_t = N_\nu \mu e^{1-l} (\frac{\epsilon l}{(l+1)H})^l (\frac{2l+1}{l+1})^{l-1} (\frac{V^{l+1}}{d^{2l+1}}). \tag{1.21}$$

where N_{nu}- valence band effective density of states, E_t - energy that characterizes the trap distribution decay, H - total trap concentration, $l = E_t/k_BT$ - slope parameter, V-voltage. The formula applied to SNO epitaxial films it has been found that there is a difference in temperature dependence of I-V slope. l is not a linear function of 1/T for these films and the trap energy is about 40 meV at RT and increases at high temperatures. While in most materials that exhibit trap limited SCLC this energy is constant. It is for example in polycrystalline SNO, and is equal about 480 meV and does not change with temperature (I-V slope is linear dependence of 1/T). This may be happening because of secondary phases contribution which may introduce trap states.

1.4.3 Metal - insulator transition in nano scale

In epitaxial $NdNiO_3$ thin films deposited on STO and LAO a critical thickness was found which separates two areas where strain and dimensionality have a competing influence of the films properties (97). Below critical thickness, which was estimated to be about 20 unit cells (u.c.), down to about 5 u.c. the covalent bandwidth is said to decrease enough to trigger NNO insulating and increases

T_{MI}. Above the 20 u.c. thickness of the film the strain becomes more important and forces Ni3d bandwidth to to increase which is said to cause metallic state and decrease of T_{MI} with decrease of thickness down to 20 u.c (97).

It was also found that for respective thickness of the films the resistivity values of compressively strained NNO films on LAO are lower than for films on STO that exhibit tensile strain. Also, an unusual thing is that while in bulk, NNO has only two phase regimes - paramagnetic metal and antiferromagnetic insulator. But the authors noticed that in the form of thin films NNO a three-phase diagram is pronounced, resembling phase diagrams of RNOs with smaller rare earth ions.

The surface effect was investigated by capping the ultrathin insulating films with a layer of the substrate material. In these films the transition was recovered and a similar behaviour to uncapped films was noticed, with the curves behaviour resembling each other for similar thicknesses. This suggests dimensionality effect rather than a surface one.

1.5 Application potential of $SmNiO_3$ thin films

The existence of MIT in $SmNiO_3$ films and other films from $RNiO_3$ family makes them perceived as candidates in numerous applications. However long this time-to-market is the predicted applications include:

- oxide electronics - neuromorphic learning circuits, capable of analog computation,

- nonvolatile memory - that require fast switching speed and scalability,

- switchable or reconfigurable interconnects and threedimensional integrated circuits - when MIT is present not only in-plane but also out-of plane (49).

In SNO/LAO and SNO/Si films a permanent change of resistivity above MI temperature was described as a memristive character of the films (49). The variation was also noticed with applying 10 V voltage in 1 s pulses to 80 nm film. Such pulses could induce a local MIT through Joule heating. Another mechanism - high current density during the pulse induces effective doping of 'the channel' as in VO_2. A gradual resistivity increase with saturation was observed at RT but at higher temperature the resistivity did not saturate after the applied 8 pulses. Authors postulated that it may be possible to induce MIT with applied voltage. This behaviour might be of memristive type, however as it is probably related to permanent oxygen loss, it is not reversible which is not of interest for electronic devices.

SNO film was used to manufacture a MOSFET transistor. The film deposited by RF magetron sputtering was not phase pure, as apart from the main phase contained Sm_2O_3, NiO, $Sm_2Si_2O_7$, Sm_2SiO_5 (56). It had a MI transition at 130 °C and a surface roughness of R_a = 1.32 nm and RMS = 1.88 nm which is acceptable for film gate insulators.

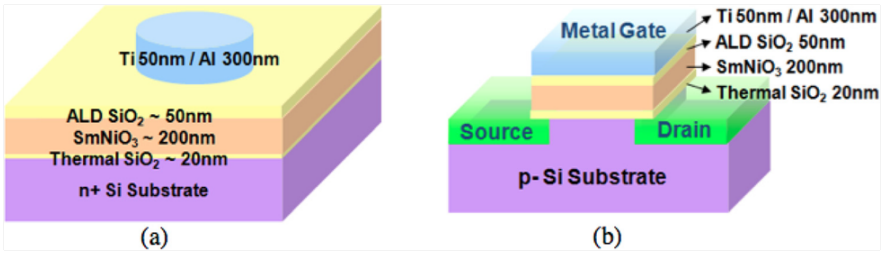

Figure 1.12: Application of the SNO film as a transistor and capacitor - Prototypes of a MOS capacitor (a) and MOSFET transistors (b) based on thin film of SNO as a gate material (56)

The measured structural parameters and capacitance allowed estimation of dielectric constant as 26 and equivalent oxide thickness t_{SNO} x (k_{SiO_2}/k_{SNO}) as 100 nm. Capacitance vs. gate voltage curves were found to be asymmetric and hysteretic and temperature dependent as well. The asymmetry was seen as a shift of curve towards lower gate voltages, with a peak capacitance at -1.9 V at all temperatures (RT up to 415 K). It was explained to be a result of nonuniform work function of electrodes and internal electric field. The hysteresis occurred with the direction of sampling of the gate voltage. By analogy to $SrTiO_3$ the authors ascribed the hysteresis to excess space charge (SC) caused by oxygen vacancies. The oxygen vacancies would occur due to instability of Ni3+ ions. Application of external electric field would de-trap electron and make the otherwise neutral vacancies - positively charged. Thus variation of internal electric field by the vacancies would influence polarization and reduce the dielectric permittivity of the crystal.

Both in MOS and MOSFET with $SmNiO_3$ the gate capacitance is hysteretic and frequency dependent. However in MOSFET device the hysteresis is counterclockwise, which is opposite to MOS. This was written to be consistent with polarization switching, alike in C-V characteristics of a transistor. It was said to be a gate-field effect as there was a treshold voltage shift with absence of channel current. It occurs also at room temperature. All this was explained as effect of space charge polarization in SNO film. Also the state retention was seen to decay

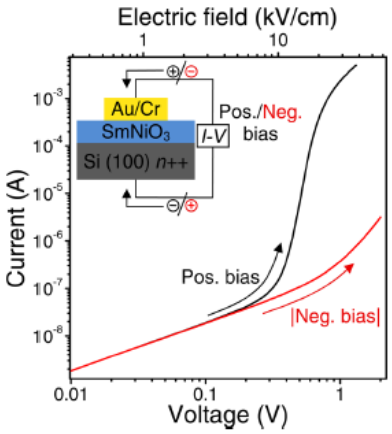

Figure 1.13: I-V characteristics of SNO rectifying device - The possible application of the SNO thin film deposited on Si. The graph shows I-V characteristic in log-log plot, showing rectification above certain voltage, negative data is ploted in the absolute values in order to clearly show the differences in the currents between positive and negative polarization. As presented in (48).

with time probably due to depolarization field due to finite dielectric constant of silicon which would degrade polarization of SNO film. The retention time of 10 s at RT is longer than the time of transistor-capacitor based silicon dynamic memory even though it is based on a single transistor.

2

Experimental methods

2.1 X-ray Diffraction

Until the Röntgen's discovery of X-rays in 1895, the diffraction phenomena was mainly implemented in diffraction gratings or focusing optics for the light in the visible range. It was first discovered in 1912 by Max von Laue that X-rays can be diffracted on crystals and that it is possible to obtain information from structures smaller than one nanometer. Therefore, thanks to the small wavelength of X-ray radiation (ranging from 0.1 nm to 10 nm) it became possible to 'see' the details of the structure of a matter. Nowadays, the X-ray diffraction method is one of the most basic, standard and popular methods to characterize and investigate materials structure.

The X-ray diffraction (XRD) is a technique that allows determination of the interior structure of many materials, including thin films. It is based on phenomena of elastic scattering of X-rays by electron clouds surrounding atoms in a given material. When this scattering (also called Thomson scattering) occurs in the periodic lattice of atoms, the interference results in the formation of the diffraction pattern. X-ray diffraction is ruled by a few equations which are fundamental for the technique and proper description of the investigated crystal structure. Thus, the X-rays irradiating any material will be scattered by atoms (or electrons surrounding atoms) in analogy to how visible radiation is scattered when passing through a slit. The beams incident on the material's surface under angle θ are scattered within the same plane and under the same angle to the surface, preserving the law of reflection. The diffracted beams interfere constructively only if they are in phase, i.e. if the path difference between beams is a multiple of the

radiation's wavelength. This diffraction condition formulated by William Henry Bragg and William Lawrence Bragg, called therefore the Braggs' law, is written as

$$n\lambda = 2d \sin\theta. \tag{2.1}$$

where interplanar distance d and incident angle θ of X-ray radiation λ are related as depicted in figure 2.1.

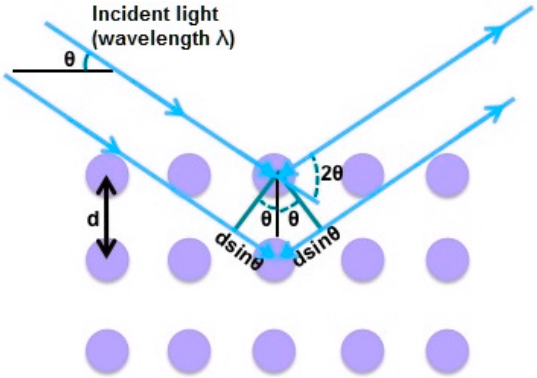

Figure 2.1: Diffraction of X-rays by a perfect crystal. - As featured in (19) p.84.

Although scattering event can occur in virtually any material, it is very strong only in the ones that are crystalline. In non-crystalline materials the d parameter is not constant, thus the requirements for constructive interference are not met.

2.1.1 X-ray diffraction on bulk materials

Bulk materials are characterized in 3 dimensions, however, our explanation on the X-ray diffraction topic shows an only 2-dimensional picture. In practice, bulk crystals have many diffraction planes depending on their orientation relative to the X-ray beam. Those planes are directly related to the crystal's symmetry group and for this reason it is crucial to observe diffraction patterns from many angles. By collecting diffraction patterns from all crystal orientations one can reconstruct the reciprocal lattice of the crystal. The reciprocal lattice is an inversion of the real lattice, and thus by Fourier transform a real lattice of a crystal can be obtained. This requires to collect 2D diffraction patterns for a number of crystal orientations and yields bond distances and symmetry information as well as the

spatial positions of atoms. However this technique requires a single crystal sample, which can be difficult to obtain, and is costly both in terms of time (analysis) and equipment (expensive setup).

It is easier to measure a polycrystalline material, most often powder, where the crystals are randomly oriented in space. This allows for relatively quick and very accurate identification of substances with known structures and is called X-ray Powder Diffraction sometimes abbreviated also as XRPD. Thus, by scanning the sample through the 2θ angles all possible diffraction directions of the lattice should be obtained. Resulting diffraction pattern consists of a set of separated diffraction peaks. The peak positions and intensity are representative mainly of the type of crystalline structure and unit cell parameters. Peak width is mostly a result of incoming beam geometry, size of the smallest crystal unit in material and its shape, as well as possible internal strains. The background may hide information about amorphous phase presence. Other information includes atomic positions, thermal scattering coefficient (Debye-Waller coefficient), and texture.

Any powdered sample requires careful preparation before a successful experiment. A powder sample should be ground well in order to let all the incoming radiation through. The grain size and careful radiation choice can account for absorption contrast effects. When investigating powder material it is necessary to take the following things into consideration: the homogeneity of the powder (if not homogeneous some phase may be underrepresented, a others may be falsely overrepresented), powder grain size (important when measuring materials that strongly absorb X-ray radiation, when the grain is small enough for such materials - the radiation goes through many grains and the phases are properly represented in the diffraction pattern), proper mounting of material into sample holder (this may account for creation of powder texture).

2.1.2 X-ray diffraction on thin films

Diffraction on thin film materials is more difficult than standard XRD measurements on bulk material. Some of the most prominent issues that need to be taken into account are - film texture, absorption contrast, film (sample) positioning and film inhomogeneity. What is more, due to the small thickness of thin films and the presence of substrate, the intensity of the obtained diffraction pattern is mostly dominated by the substrate. In order to increase the signal coming from the thin film itself one can increase the optical path of incoming X-ray radiation by lowering the incidence angle to a so-called grazing incidence (Seeman-Bohlin

geometry). For example with incident angle equal to 5°, the effective film thickness is 12 times larger than in standard geometry (83). However, it is not always possible (or necessary) to employ grazing incidence set-up. A good example is the measurements presented here, which were made with the use of X-ray diffractometer XRD-7 from Seifert-FPM, Freiberg. Cobalt anode radiation was used ($\lambda_{K\alpha_1}$ = 1.788965 Å), which was filtered through the iron foil. The diffracted beam was detected by a scintillation counter. A standard Bragg-Brentano θ-2θ geometry was used. This caused the inevitable contribution of the silicon substrate, but the Bragg reflections of the substrate did not interfere with the reflections from the films. The analysis was made by comparison of the obtained intensities of diffraction peaks with reference patterns from the PDF-2 database from ICDD in Seifert software. Diffraction patterns were analyzed by Rietveld method with the use of FullProf software (86) and crystallographic information files (cif) from COD database (22, 37, 38, 39, 40, 79, 85).

The crystalline structure of coatings or films, especially thin films is a result of complex interplay of the crystalline structure of substrate, deposition technique and conditions, subsequent post-treatment and film thickness. These factors decide what phases are being formed on the substrate, crystallinity, the type of crystal structure and its parameters as well as possible preferred orientation. Therefore care should be taken while analyzing the patterns. A standard powder pattern for a perovskite-type $SmNiO_3$ compound is shown in the figure 2.2.

The films were sputtered from a target that is composed of $SmNi_2O_4$ and NiO pellets. Therefore when grown as thin films, the Sm-Ni-O films may shown presence of other phases - unreacted NiO binary oxide or $SmNi_2O_4$, products of $SmNi_2O_4$ decomposition or Ruddlesden-Popper phases. Also phases that occur from interaction of the impinging species with the substrate may occur. Their formation is dependent on the availability of nucleation sites mainly due to crystal surface structure of a substrate and favourable thermodynamic conditions. Some conditions may also favour formation of Ruddlesden-Popper phases that share a general formula of $A_{n+1}B_nX_{3n+1}$, where A, B are cations and X is an anion, n$\in \mathbb{N}$. The n-th phase would consist of n layers of ABX_3 and a AX layer on a stack. In case of an infinite n, the structure becomes the perovskite type ABX_3. Regardless of the structural similarities between the Ruddlesden-Popper phases, their X-ray diffraction patterns may be quite different - as shown in figure 1.5.

Another important factor is the crystalline orientation of the deposited film. It is known that the crystalline structure of thin film materials depend strongly on the substrate and manufacturing parameters. The difficulty lies in the proper

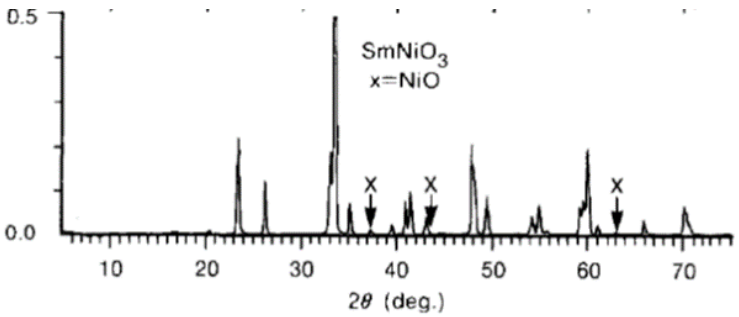

Figure 2.2: XRD patten of SNO powder. - The pattern presents intensities of Bragg reflections of a proper polycrystalline sample. A bit of NiO impurity is also visible. As featured in (66)

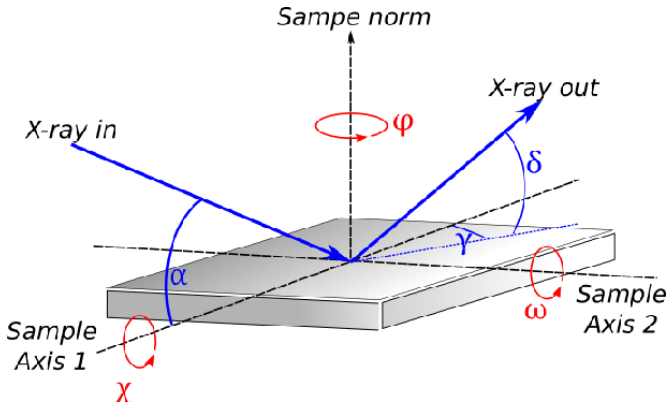

Figure 2.3: Axes and angles in an XRD measurement - The standard reflected and diffracted beam angles as well as other angles used in pole figure measurements are explained.

identification of obtained diffraction peaks. For polycrystalline structure there is by far less uncertainty than when a film is strongly textured. A strong crystalline texture may result in suppression of most of the diffraction peaks regardless of their intensity. A careful determination of the peak origin is therefore necessary. The appearance of a strong texture in the investigated films lead to further investigation through a pole figure method. It is a basic method for investigation of epitaxial or textured materials. The idea behind the method is to measure the intensity of a selected diffraction peak present in the standard pattern, in 3D space by varying the angular position of the sample: Ψ and Φ as in figure 2.3. The obtained intensities are depicted as a stereographic or equal-area projection.

2.2 X-ray Fluorescence Spectroscopy

X-ray Fluorescence Spectroscopy (XRF) is a fast and informative technique to analyse the chemical composition of an unknown material. The core phenomena underlying the measurement technique is the fluorescence of atoms of a sample, induced by irradiation with intense X-ray radiation of wide range of wavelengths. The electrons in sample are excited to higher energy level which is a photoelectric effect. The relaxation of the atom is done by relaxation of electrons to lower energy levels with simultaneous emission of X-ray radiation. The emitted set of wavelengths is corresponding to the structure of electronic levels in an atom and thus is characteristic of the chemical composition of material. Once the radiation is absorbed it can further interact with the sample's matter and become attenuated or amplified. Reliable quantification of elemental content requires to have a numerical determinant of the strength of those phenomena. This is well realized by application of mass absorption coefficient.

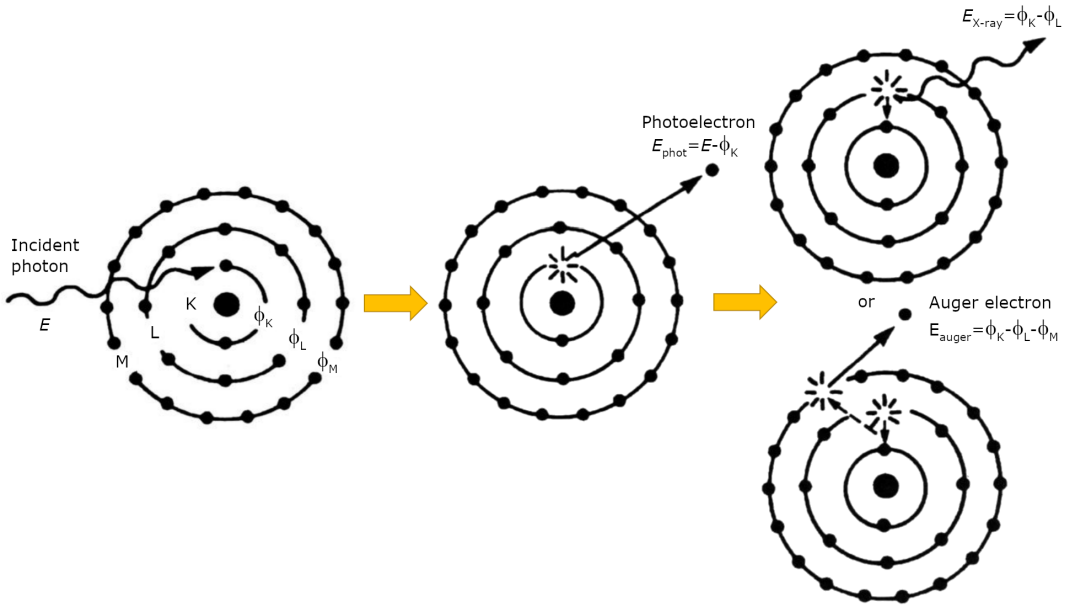

Figure 2.4: Scheme of generation of fluorescent radiation - A core level electron is excited by absorbed X-ray or gamma photon. Photoelectric ionization can be followed by either radiative relaxation, causing the emission of characteristic fluorescent X-rays or non-radiative relaxation, involving the emission of Auger electrons. As presented in (31), p.370.

The coefficient is a weighted sum of mass attenuation coefficients of all elements present in a sample. However, the coefficient depends on the energy of radiation. This results in varying sensitivity of detection of elements.

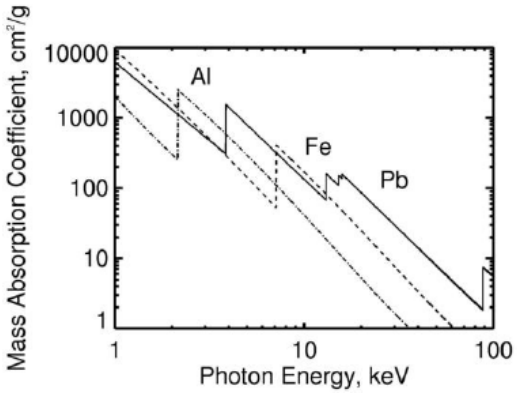

Figure 2.5: Energy dependence of the mass absorption coefficient μ for several elements - Show elements such as Sm, Eu, Ni, O, Cr, and photon energy of rhodium radiation. Adapted from (31), p.368.

The intensity of the fluorescent X-ray radiation is proportional to the concentration of an element in a sample. Typically, in order to correctly assess the concentration of elements in the unknown sample, it is necessary to use a calibration curve. The curve is a relation between intensity fluorescent radiation and the elemental concentration and is obtained for known standards. Nowadays, theoretical intensities can be also obtained, and reliable XRF analysis can be performed without measuring any additional standards.

However, one has to remember that proper sample preparation is becoming critical for obtaining good results of the sample composition. Typically sample should be ground finely without any selective losses of chemical elements and the powder should be mixed thoroughly to obtain a homogeneous mixture. On the other hand, thin film materials cannot be ground and mixed. This is an advantage and disadvantage at the same time. Despite the fact that the sample cannot be made homogenous, high energy X-rays can penetrate into the bulk (depending on the energy). What is more, knowing the composition of the material, one can calculate the decrease in the radiation intensity due to the absorption of the material.

The XRF measurements in this work were performed with the use of ZSX Primus II from Rigaku equipped with 4 kW X-ray tube with Rh anode. This

equipment allows for the analysis of the elements starting from Be to U thanks to wave-dispersive analysis and two detectors - proportional and scintillation. The typical measurements errors were estimated to be around 5% of relative error. Besides standard measurement, it was possible to investigate thin films and to perform mapping with 0.5 mm resolution. The thin film investigation was able to detect the thin film thickness in a reliable way, which was confirmed by additional experiments - that is AFM profile on ion-etched samples.

2.3 Time-of-Flight Secondary Ion Mass Spectroscopy

Mass spectrometry is a group of techniques that involve analysis of mass of particles that are ejected from investigated solid material and based on that reconstruct the chemical composition of material. The ejection of atoms and ions is caused by a focused beam of so-called primary ions that have a certain amount of energy sufficient for sputtering. The ions that leave the material of interest are accelerated into mass spectrometer and further analyzed in terms of their mass-to-charge ratio. In order to obtain a meaningful quantitative information on atomic concentrations it is necessary to use data for standard materials.

The primary ion beam has a small size (diameter) and its position can be controlled, that facilitates a scanning movement of the gun and gives a possibility of surface imaging so a 3D maps of chemical composition, that is depth profiling. The large advantage of the technique is that it can detect ions with a very small detection limit in ppb-ppm range and can detect hydrogen atoms and ions (protons). Depending on the diameter of the primary ion beam the lateral resolution may be as small as 20-50 nanometers, whereas the depth resolution is even higher - 2-30 nm.

Depending on type of mass spectrometer used in the equipment a variations of technique exist such as Quadruple Mass Spectrometry, Magnetic Sector Mass Spectrometry or Time-of-Flight Mass Spectrometry which was used in current work. The TOF-SIMS, as it is called, utilizes a measurement of time of ion's flight to the detector through an area where electric field of known strength is applied. This enables to calculate the mass-to-charge ratio from equation 2.2

$$t = \frac{d}{\sqrt{2U}}\sqrt{\frac{m}{q}} \tag{2.2}$$

where t - time of flight of ion of mass m and charge q through a path of length d after being accelerated by a potential difference U.

The chemical composition and structure of the obtained films were studied by surface sensitive technique Time of Flight Secondary Ion Mass Spectroscopy (TOF-SIMS) using IONTOF TOF-SIMS.V spectrometer (ION-TOF GmbH, Münster, Germany). By rastering a fine-focused, pulsed bismuth ion beam over a predominated area, the mass spectra of secondary ions, as well as secondary ion distribution maps, can be obtained with the depth resolution of 1-3 monolayers. High surface sensitivity provided by primary bismuth ion beam together with low energy sputtering Cs gun allows to obtain spectral, imaging and depth information. In the executed experiments, the depth profile measurements were performed in dual beam mode. Here two beams, sputter beam (Cs, 2 kV, 100 nA) and analytical primary ion beam (Bi_3^{++}, 30 kV, 1 pA), were operated alternately in the non-interlaced sub-mode (12 frames for analysis, 2s for sputtering). The analysis was performed from 500 $\times$ 500 μm areas. Both beams hit the target at an angle of 45°. The negative mass spectra were collected at each step of the depth profile. The mass spectra were calibrated using H^+, CH_3^+, $C_2H_3^+$, $C_3H_3^+$ and $C_3H_5^+$ ions. The analysis was executed using Surface Lab 6 software.

2.4 X-ray Photoelectron Spectroscopy

During the metal-insulator transition of a compound, the electronic structure of constituent elements changes. In order to get insight into the chemical composition and electronic structure of a material, X-ray Photoelectron Spectroscopy (XPS) is the best choice for laboratory technique when studying thin films. It uses soft X-ray radiation as a "pump" source to "probe" the energy of electrons excited from the sample. By applying a relatively high energy X-ray radiation, such as monochromatic Al Kα (1486.7 eV) or Mg Kα (1253.6 eV), not only the valence but also the core electronic levels of atoms may be investigated. The excited electrons hold information about their origin and thus may give information intrinsic to internal electronic structure of the investigated material. The information is retrieved from the well-known Einstein formula which equates the energy of impinging X-ray quanta $h\nu$ to binding energy (BE) of electron E_B, work function of the investigated material ϕ and kinetic energy of electron which escaped from the material.

$$h\nu = |E_B| + \phi + E_{kin}. \tag{2.3}$$

The equation states that an electron that has a binding energy E_b with respect to Fermi level, and is irradiated by a photon with energy $\hbar\omega$, leaves the system with kinetic energy E_{kin} if the photon energy is high enough to be used to overcome the energy barrier Φ_w between the solid surface and vacuum, called the work function. This simplified picture of a single-particle system does not take into account the complexity of any solid-state system. An important role is also played by other effects that influence the energy and thus energetic distribution of electrons. They involve Auger effect, multiplet splitting, shake-up process and any other interaction of the photoelectron with electrons and ions in the system.

By analysing the kinetic energy of electrons excited by a discreet wavelength - the binding energy of electrons in the investigated material is retrieved. The obtained spectrum of binding energies is unique for a given material and serves as a tool to identify chemical elements, based on the approximation that electrons in a solid are reside in orbitals. This is the most basic use of XPS method and explains the early acronym of the technique - ESCA - Electron Spectroscopy for Chemical Analysis.

In samarium nickelate the basic, survey spectrum collected for Al radiation reveals (figure 2.6) several important features characteristic to XPS such as

1. main photoelectron emission lines for oxygen (O*1s*, O*2s*), nickel (Ni*2s*, Ni$2p_{3/2}$, Ni$2p_{1/2}$, Ni*3s*, Ni*3p*), samarium (Sm$3d_{3/2}$, Sm$3d_{5/2}$, Sm*4s*, Sm*4p*, Sm*4d*, Sm*5s*, Sm*5p*)

2. Auger electron peaks that arise from secondary excitation of electron due to filling of PE hole by an electron from higher level. Their energy depends only on the difference between certain electronic levels. These appear for nickel (LMM series $L_3M_{23}M_{23}$, $L_2M_{23}M_{23}$, $L_3M_{23}M_{45}(^1P)$, $L_3M_{23}M_{45}(^3P)$, $L_2M_{13}M_{45}(^1P)$, $L_3M_{45}M_{45}$), oxygen (KLL series KL_1L_1, KL_1L_{23}, $KL_{23}L_{23}$), samarium (MNN series $M_{45}N_{45}N_{45}$)

3. carbon contamination line C*1s* and its Auger line KVV

4. background formed due to inelastically scattered photoelectrons.

Because the irradiated material is a many-body system, the photoionization process causes several final state effects that in XPS cannot be disregarded. The

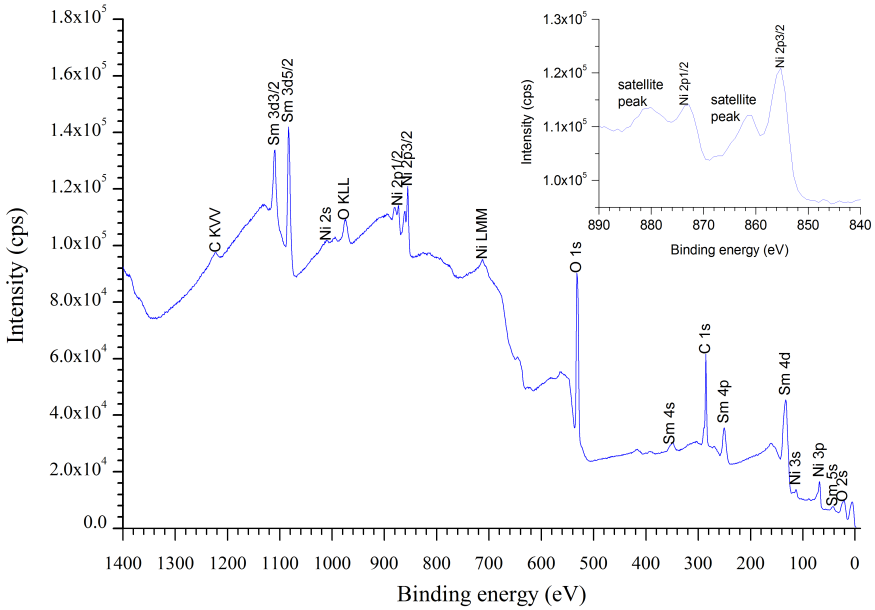

Figure 2.6: XPS survey spectrum of $SmNiO_3$ - The main photoelectron emission lines, Auger series are evidenced as well as the shake-up satellites in the nickel $2p$ spectrum as shown in the inset.

positive potential of a core hole created in the primary process influences the behaviour of surrounding electrons. The electrons try to relax in the intra- or extra-atomic mode depending on the origin of the electrons. The relaxation processes are visible in the form of satellite peaks, which arise from a photoelectron with slightly lower kinetic energy, therefore higher binding energy and appear as peaks at the higher BE side of the mainline. The satellites may come from shake-up or shake-off processes, or plasmon losses. The photoionized electron interacts with one of the bound electrons and excites it to higher state. Shake-up satellites arise when the bound electron is excited to a higher unoccupied state. Shake-off satellites appear when the electron obtains enough energy to leave the ion into the vacuum. A collective excitation of valence electrons, namely a plasmon, occurs either during the propagation of energetic photoelectron through the solid (extrinsic plasmon) or as a response to the formation of a core hole. As plasmon is an oscillation quantized in terms of energy, the plasmon loss peaks are shifted towards higher BE by by $n(\hbar\omega_p) + m(\hbar\omega_s)$, where n, m are integers, being a sum of energies of bulk and surface plasmons.

More sophisticated use of XPS is related to the fact that electrons feel the environment and react to it. This phenomenon is called a chemical shift and means

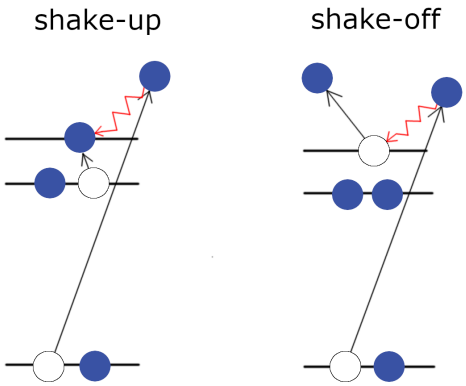

Figure 2.7: Shake-up and shake-off satellites. - they originate from an abrupt change in the Coulomb potential as the photo-electron travels through the valence band.

that simply put, the binding energy of an electron may shift depending on the *chemical* surrounding of the atom/ion it originates from. In that way, an assessment of energy of chemical bonds is made. In XPS the energy of radiation is high enough to probe both valence and deep core electronic states. Whereas in UPS (Ultraviolet Photoelectron Spectroscopy), an associate technique, the ultraviolet radiation is only sufficient to pump/probe the electrons from valence levels down to about 20-40 eV binding energy. Also because of increased energy resolution, UPS offers much more detailed analysis of valence levels than XPS.

In rare-earth nickelates the nickel - oxygen bond is important in view of their metal-insulator transition. They are the elements of which Ni2p and O1s electronic levels may overlap and enable transition of electrons above the Fermi level. Possible variation of electronic levels of nickel and oxygen at the transition temperature is important to investigate. Nickel and oxygen atoms in crystal lattice are arranged in octahedra with four oxygen atoms in nickel plane and two atoms perpendicular to that plane. This configuration leads to the formation of a minimum of two different bond lengths. While monoclinically distorted, the nickel atoms occupy different positions in crystallographic lattice and ”hold” various charge on each site. The XPS study of nickel electronic structure involves mainly investigation of Ni2p line which in nickelates has many features that complicate the analysis.

The investigation of the electronic structure of nickel is not a straightforward

task. In order to obtain meaningful information, usually, the multiplet Ni2p spectra are analyzed, which contain the spin-orbit coupled components from originating from 2p3/2 and 2 p1/ 2 levels, - satellites assigned to excitations within the valence band and/or plasmon excitations - plasmon loss satellites. Clean oxygen-free metallic nickel has its main Ni2p line at about 852.6 eV *et al.*(43). It is accompanied by two satellites at about 3.7 and 6 eV higher BEs. In $RNiO_3$ the nickel line is split into two components - the Ni $2p_{3/2}$ and $2p_{1/2}$. This multiplet splitting occurs due to presence of unpaired electrons in nickel 3+ ions. In the early 1970s Matienzo studied by XPS almost seventy nickel compounds and noticed that binding energy of nickel in its compounds can have a wide range of values (73). Especially for the octahedrally coordinated nickel ions. The binding energy is correlated with ligand electronegativity and their ability to remove electron from metal ion. For oxygen it is larger than for fluorine or bromine. The binding energy itself was said to have no confirmation in the oxidation state of nickel in the different compounds. It is because the differences in binding energy - in for example compounds with Ni2+ ions - were noticed to be as large as 4 eV.

The nickel structure is rather complicated and its analysis requires a careful deconvolution.

The shake-up satellites that appear in the spectra were discussed to follow some rules depending on the coordinated ligand as well (73). In paramagnetic compounds where nickel is octahedrally coordinated with oxygen, the satellites usually appear one for each of the Ni2p main line components (C type satellites). In diamagnetic compounds these should not appear. The stereochemistry was not seen to play a major role in the qualitative character of the nickel spectra. However the shake-up satellite separation from the main line might comply with the degree of covalency of a bonding, with the bonding being more covalent for satellites further apart (73). For the qualitative information on the bonding, the binding energy should be also considered.

As calculated by Veenendaal and Sawatzky, a main xps line of nickel ion surrounded by NiO_6 clusters reflects well spectrum shown by nickel oxide (94). The structure of $2p_{3/2}$ line is complex. It consists of main line, additional high BE line resulting from screening by an electron originating from oxygen orbitals from a neighbouring NiO_6 unit rather than from around the Ni atom with a core hole.

For a polycrystalline NiO, the main multiplet line could only be fitted with at least four components from 853 up to 857 eV. This creates a large difficulty in fitting and differentiation of specific oxidation states of nickel. The calculations

performed by Gupta and Sen (GS) reveal that the spectra are quite complex, however in their case the crystal field was neglected (46).

Investigation of oxygen is realized by looking at O1s orbitals, however this is not an easy task. Oxygen is a reactive element and forms bonds with many other elements. Therefore O1s spectrum is often composed of several lines that may as well correspond to surface contamination from water, organic compounds, etc. These form broad peak components that impede a unique fitting with a reliable analysis of oxygen chemical states.

Another case is with thin films. Due to their confined dimensions in one direction additional difficulties might appear. Film surface may have broken bonds, and the need to minimize the energy can cause surface reconstruction and variation of bonding and binding energies. On the other hand, the interface is also a complicated region where atoms of two different compounds meet, most often also with a different crystal structure. In between the two, in the "regular" part, the appearance of such phenomena as strain and relaxation may be expected. The XPS spectra of very thin films are a combination of constributions from the surface, near-interface region and the "regular" middle part. Depending on the substrate, the spectra of $SmNiO_3$ thin films can differ a little. The perovskite-like substrates such as LAO, SLAO or STO, help preserve similar structure in the films. Therefore in stable epitaxial films, the observed binding energies of Ni*2p* spectra are attributed mostly to Ni^{3+} state with a small addition of Ni^{2+} state occurring at 855.5 and 854/854.5 eV, respectively (9). With tensile strain and lattice mismatch the lower oxidation states of nickel are favoured and so lower binding energies. This is often related to multiphase crystal structure and contaminant phases. In films deposited on silicon or sapphire, the SNO phase is a minor phase in comparison to other binary oxides and nickel states found in the material are composed of 854.5 eV and 852.5 eV peaks.

The X-rays from Al or Mg radiation can travel far into the sample, the absorption depth can be several micrometers. However the escape depth of electrons is limited, therefore XPS is a mostly surface sensitive technique. Several monolayers, up to a few nanometers is available for the investigation. The depth depends on the inelastic mean free path (IMFP) of a certain electron in a material of a certain density and electronic structure. Still most of the studied samarium nickelate thin films were too thick to obtain the information from the whole film. This was overcome by applying argon ion etching followed by XPS analysis, which is called depth profiling. Although it provides information on chemical composition in greater depths into the sample, the technique is not good for analysis of chem-

ical bondings. It is known that argon ions may cause reduction of metallic ions in many metal oxides such as Fe_2O_3, Fe_2NiO_4, Fe_2ZnO_4 (90). This should be taken into account because analysis of metal spectra is highly disturbed after ion sputtering. Lowering the ion beam energy or using ion clusters (18) may minimise but not eliminate the reduction effect.

The main emission line is dealt with in two ways. On the one side, it is assumed that each contribution to the mainline (photoelectron) of the spectrum is solely dependent on the oxidation state of nickel ion. Thus the Ni^0, Ni^{2+} and Ni^{3+} states are identified at 852.6, 854.6 and 856.1 eV to Ni $2p_{3/2}$ XPS, respectively in compounds such as oxidized Ni, oxides, hydroxides and oxyhydroxides (43). This is a simplified picture often used to enable comparison between various materials. However, the assumptions should be based on theoretical predictions which yield rather complicated spectra for nickel states. Many factors such as crystal field may have a strong effect on the shape of the spectra. Gupta and Sen (46) have used the free-ion Hartree-Fock approximation including crystal field and spin-orbit splitting effects to calculate the p-vacancy levels of some transition metals. Several ground state configurations were considered such as: p5d1 and p5d9, p5d2 and p5d8, p5d3 and p5d7, and p5d6 and p5d4, and yielded complex nickel spectra. Grosvenor et al. have used the calculations to investigate the Ni2p multiplet envelopes of nickel hydroxide and oxyhydroxides spectra (43). They have used sets of components respective to Ni^{2+} and Ni^{3+} states with only relative proportion allowed to vary. The results on $Ni(OH)_2$ and γ-NiOOH indicate the oxidation state to be in agreement with what is derived from stoichiometry. However in β-NiOOH the spectra indicate a mixture of Ni^{2+} and Ni^{3+} species which agrees with literature reports of decomposition to $Ni_3(OH)_4O_2$. All of the presented spectra needed an additional broad peak at the higher binding energy side. The peak was ascribed to surface loss phenomena. The GS calculations cannot well represent the complex structure of NiO, where non-local screening effects and intersite charge transfer of $d^{n+1}d^{n-1}$ need to be taken into account.

Below are presented some exemplary nickel 2p spectra of various nickel-bearing compounds. A spectrum of clean nickel metal does not contain a single photoelectrom emission line but shows a contribution of two more - satellites (figure 2.9 a.). Spectra of NiO (figure 2.9 b.) and $Ni(OH)_2$ (figure 2.9 c.) are more complicated and have been fitted with a multiple peak envelopes based on the Gupta and Sen calculations of 2p core multiplet structures (45, 46). Four different cases of multiplet structure of nickel 2p vacancies, the results of calculations, are presented in figure 2.8. A complex structure of multiplet spectra is evident for each

of the nickel state. Those calculations were the basis for analysis of spectra for certain nickel compounds in other works, for example Grosvenor *et al.* (43). The results of their work is presented in figure 2.9. Further work on quantification of the chemical states in nickel compounds is done by Biesinger *et al.* (11).

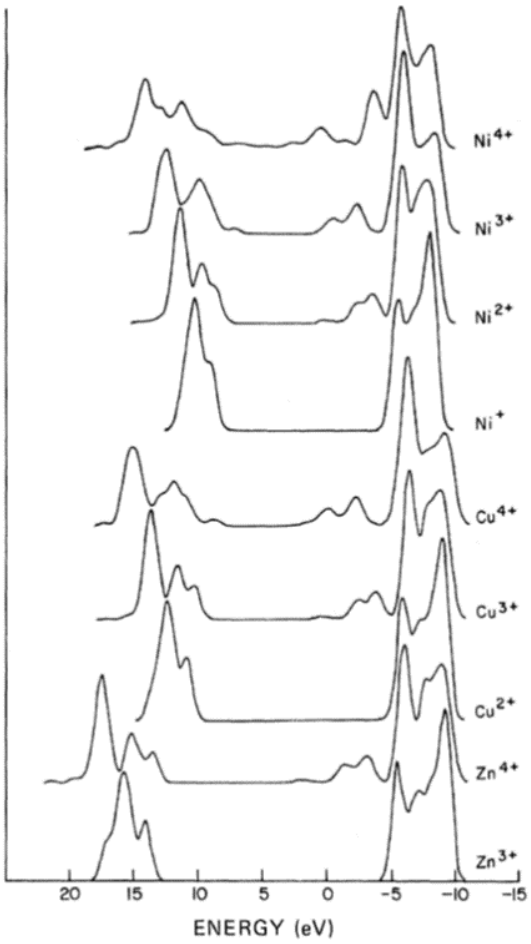

Figure 2.8: Multiplet structure of 2p vacancy in nickel spectra - Zero energy is an arbitrary point. Intensity is normalized in the same manner for all spectra. As presented in (46)

In the primary work by Gupta and Sen, several spectra for multiplet structure of 2p vacancies created in TM ions were calculated. The calculations took into account spin-orbit splitting (interaction). However crystal field effects were substituted by some approximation by Löwdin, and ground-state configuration was used instead of other (therefore satellites are not correctly predicted).

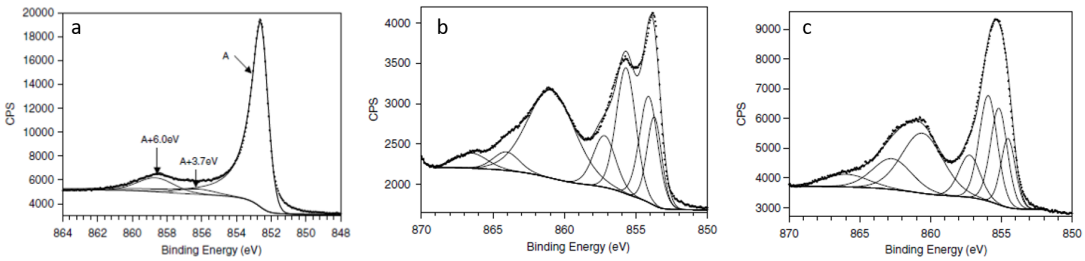

Figure 2.9: Exemplary XPS spectra of Ni2$p_{3/2}$ that show a complicated composition of the nickel envelope - The presented envelopes come from a. clean nickel metal, b. NiO fitted with Ni(II) multiplet structure, c. $Ni(OH)_2$ fitted with Ni(II) multiplet envelope. As presented in (43)

From these spectra one can conclude that it is almost impossible to ascribe a single peak to one particular ionic state. In order to resolve the spectra, a whole envelope of peaks corresponding to a particular ionic state should be taken into account. Only such envelopes in total should contribute to quantitative investigation of chemical state of a transition metal ion (11).

The measurements described in this work were taken with multi-technique electron spectrometer, model PHI 5700/660 from Physical Electronics. The monochromatized Al Kα radiation was used. It enables probing the core electron states down to 1486.6 eV reduced by the work function of the spectrometer. The energy resolution depended on chosen parameters of the spectrometer, the measurement range and specific spectral lines. In order to investigate the transition, spectra were recorded at various temperatures starting as low as about the liquid nitrogen temperature up to over 400 K, that is below and over metal-insulator transition for $SmNiO_3$. All experiments were conducted in ultra-high vacuum. The electrons that left the surface at a take-off angle of 45° were detected.

In XPS, the weakly or non-conducting materials are more difficult to study as there is a common risk of charge build-up which can mask the true electronic structure. If there is not enough of delocalized, conduction electrons to fill the photoelectron holes, the near-surface positive potential arises. This potential acts on the escaping electrons and modifies their kinetic energy. Such are the $SmNiO_3$ films and most of $RNiO_3$ compounds in a wide temperature range, below MIT. The effect may be overcome by supplying slow electrons just above a sample surface to neutralize the artificial positive potential. However this raises questions on a proper neutralization of the artificial positive potential. The charging effect depends also on the sampling depth. It is important to provide a good electrical

contact between the sample, i.e. thin film, and the underlying sample holder. For metals in general the issue does not appear. However for semiconducting and insulating materials it is necessary to ensure the contact between bottom of the sample and top of the holder, as well as provide additional 'tracks' for electrons by applying conducting silver paste glue at sample edges or even glue the sample to the holder.

Because below the MI transition the films were semiconducting it was necessary to prevent the positive charge build-up at the films' surfaces. A low incidence stream of low energy electrons was used to compensate for the charge of ejected photoelectrons. The compensation was verified by looking most often at carbon C 1s or oxygen O 1s spectral line. Both the emission current and electron energy were adjusted.

The multiplet spectra of nickel were most often measured with pass energy 23.5 eV. Fitting of spectra was made with a constant number of lines. For main multiplet line it were 4 components, while for the $2p_{3/2}$ and $2p_{1/2}$ satellites - 3 components were necessary. The same set of components was used for fitting spectra obtained at every temperature. At initial stages of each fitting procedure constraints were set for the multiplet splitting energy and ratio between $2p_{3/2}$ and $2p_{1/2}$ lines . The background was fitted with iterated Shirley model. Due to charging effects it was sometimes necessary to use the low energy electron gun. This however was not always sufficient to neutralize the measured surface. Therefore a post-processing procedure involving spectra shift with respect to a certain XPS line was done. The reference peak was either the C1s line of carbon or Sm $3d_{5/2}$ line of samarium which is not expected to vary with temperature. For each fitted nickel dataset the line position, FWHM, $Ni^{3-\delta}/Ni^{3+\delta}$ area ratio, $Ni^{3+\delta}$-$Ni^{3-\delta}$ energy displacement, spin-orbit splitting, were extracted and compared.

Obtaining good quality nickel spectra of $SmNiO_3$ thin films was not an easy task due to a layer of contaminations of the surface. Long several-hour experiments, especially at lower temperatures, were necessary to increase the statistics and signal-to-noise ratio. Temperature was kept constant during each experiment. Prolonged spectra aquisition time and irradiation by X-rays have at times caused charging effects that were adjusted for before the measurement. At the beginning of each experiment any changes were monitored and if necessary, additional adjustments were made. It was necessary for some of the samples to mechanically modify the surface by scraping with an alumina blade.

2.5 Atomic Force Microscopy

Scanning Probe Microscopy (SPM) is a tool that enables probing structure, mechanical, electrical or even magnetic behaviour. It allows for the investigation of surfaces, especially the surface of thin films, providing unique information in nanoscale.

The most basic use is to visualize the material's surface - topography. Atomic Force Microscopy (AFM) is only one of the many variations of the Scanning Probe Microscopy methods to do that. The principle of operation is to use a atomic sharp tip and scan the surface as closely as possible in order to detect the required interaction. With the use of electronic equipment the interaction is obtained as an electric signal and is further transformed to meaningful data. The interaction between the scanning tip and the sample surface is mainly due to Pauli principle at very short distances, and van der Waals forces at longer distances.

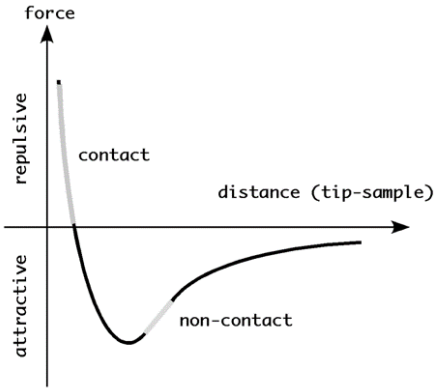

Figure 2.10: Force between the sample and the scanning spm tip as a function of their separation distance - At short distance the tip and sample are in contact mode and the interaction force is repulsive. With the increase of distance, the force becomes attractive and scanning is performed in non-contact mode in a range where the relationship is close to linear.

At short distances the interaction is repulsive due to overlapping electronic orbitals of scanning tip and atoms of the scanned surface. The Pauli principle is in operation, and further approach of the tip to the surface is stopped by strong repulsive forces whose magnitude depends on the distance r as $1/r^{12}$. In this region the tip is almost "touching" the surface so the working mode is called **contact mode**. With increase of the distance between scanning tip and sample surface the forces are becoming attractive and are mainly van der Waals forces.

These forces have its origin in three types of interaction and are connected with polar nature of matter and dipole moments. This attractive interaction has a $1/r^6$ dependence on the r distance between sample and the tip.

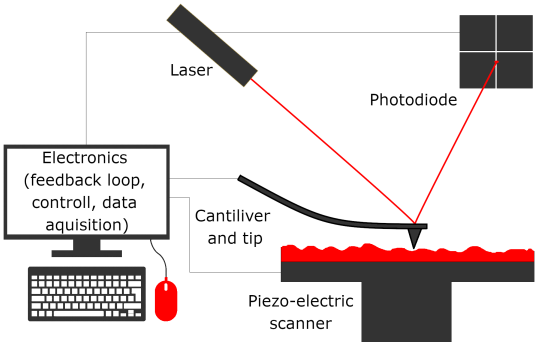

Figure 2.11: Schematic view of AFM set-up - Basic components of atomic force microscope include cantilever with a sharp tip for scanning of the sample surface. Its movement is detected by a laser radiation reflected from the top of cantilever and detected by a position sensitive photodiode. The signal is then converted by electronics and a feedback signal is sent to cantilever controller. The scanning movement is realized by piezoelectric elements connected either with the cantilever or the sample table.

In contact mode the tip is so close to the surface that actually a direct contact is provided, and what follows electrical contact as well. This allows for measuring the electrical response of the sample to an applied potential and the variation of the method to do that is called Local Conductivity AFM (LC-AFM) or CAFM (Conductive AFM). In this set-up this is a two-contact method, one electrode being the sample surface and second being the scanning tip. When both electrodes are conducting, the applied voltage triggers flow of electric current which is measured by electronic system. In experimental setup application of positive (negative) bias voltage means that there is positive (negative) potential on the scanning tip and the electron current induced with the bias voltage flows from sample surface to tip (tip to sample surface).

In fact, most often in LC-AFM method the sheet resistance of a thin film is measured. A sample, that is film on a substrate, is placed on a metal holder and clamped with a metallic element in order to prevent movement. The clamp is most often placed at the top of the sample, i.e. film's surface. What follows is that the current between the two electrodes will go only in the strictly in the interface region. It is mainly due to a large gradient of potential drop from the

contact point into the film's volume.

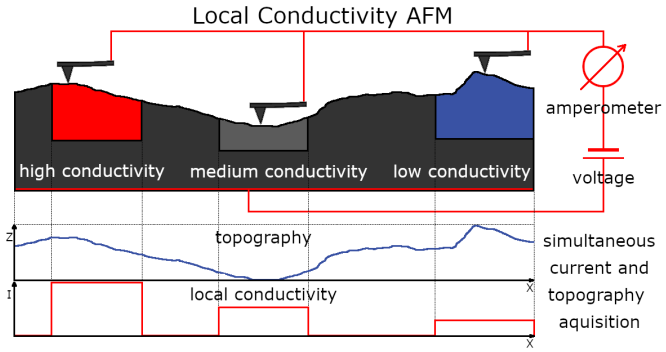

Figure 2.12: Schematic view of local conductivity AFM measurements - Additional bias voltage is applied between the scanning tip and sample. While standard topography scan is performed, the bias triggers current flow and its value is measured at each point of sample surface. This way both topography and local current map are collected.

Scanning tip is in general made of silicon and its electrical conductivity is provided by a metallic coating of the tip. There are other options, like full metal tips, heavy doped silicon, or other materials, however, they are not as popular as standard metal-coated Si tips. In case of performed local conductivity measurement a silicon Pt-Ir coated tips were used from various manufacturers, mostly Budget Sensors.

In several cases, a non-contact mode was applied to obtain a better resolution of the film's surface topography. In no-contact (or tapping) mode, the tip oscillates near its resonance frequency. The interaction with the surface shifts the oscillation frequency of the tip, the shift is higher the smaller is the tip-surface distance. This can be used for the AFM feedback loop. For these measurements typical silicon tips are used due to their sharpness (tip apex <10 nm) and prevalence.

Microscopic investigation of samples topography and local conductivity measurements were taken with AFM/STM VT from Omicron and RHK AFM. RHK is a special microscope with Besocke-type head. All experiments were performed in an ultra-high vacuum of the order of $10^{-9} - 10^{-10}$ mbar. Obtained data were analysed with the use of Vernissage (mostly I-V curves and data export), WSxM (the I-V maps) (52, 53) and Gwyddion (topography and local conductivity maps) software (64, 81). Measurements were taken at different temperatures in order to investigate the variation of current response to applied voltage below and above expected metal-insulator transition.

2.6 Raman Spectroscopy

Raman scattering is a vibrational spectroscopy sensitive to molecular vibrations. The incident radiation absorbed by a molecule induces a polarization according to equation 2.4

$$P = \alpha E. \tag{2.4}$$

where P is the strength of induced polarization, α is the polarizability of the molecule and E is the impinging oscillating electric field (75). The polarized molecule, a dipole, radiates a light scattered in various directions in an elastic or inelastic way. Once the ultraviolet (UV), visible or near infrared (NIR) radiation falls on a material, the vibrational levels of molecules are excited to virtual levels. While the molecule transitions back to molecular energy levels, a radiation quantum is emitted. Such scattering may occur in three different paths depending on the energy of emitted radiation - elastic Rayleigh scattering, and non-elastic Stokes and anti-Stokes scattering type. The frequency of radiation scattered by the molecule ν_R, the Raman shift, is calculated from equation 2.5

$$h\nu_R = h\nu_0 - h\nu_L. \tag{2.5}$$

where ν_0 is the frequency of incident radiation, ν_L - frequency of selected energy level, ν_R - frequency of Raman shift. In anti-Stokes scattering, the transition is from higher to a lower vibrational level, while in Stokes scattering transition occurs from lower to higher energy level. The collected variation of scattered intensities as a function of frequency represents the values of Raman shift that occur in the studied material. In normal conditions, it is more probable to collect Stokes than anti-Stokes Rayleigh scattering (98). Comparison between transitions in various types of vibrational spectroscopy are depicted in 2.13.

The exciting radiation in vibrational spectroscopy is usually laser radiation. The laser radiation should be of intensity high enough for the Raman effect to be visible because the Raman scattering is typically about 10^{-10} the intensity of mid-IR absorption (75).

Structural analysis in temperature-dependent mode (2 K/1min, about 1 K stabilization) has been performed from 293 K to 473 K (during the heating and cooling) using WITec confocal Raman microscope CRM alpha 300 R equipped with an air-cooled solid-state laser ($\lambda = 532$ nm) and a CCD camera. The excitation laser radiation was coupled into a microscope through a single-mode optical

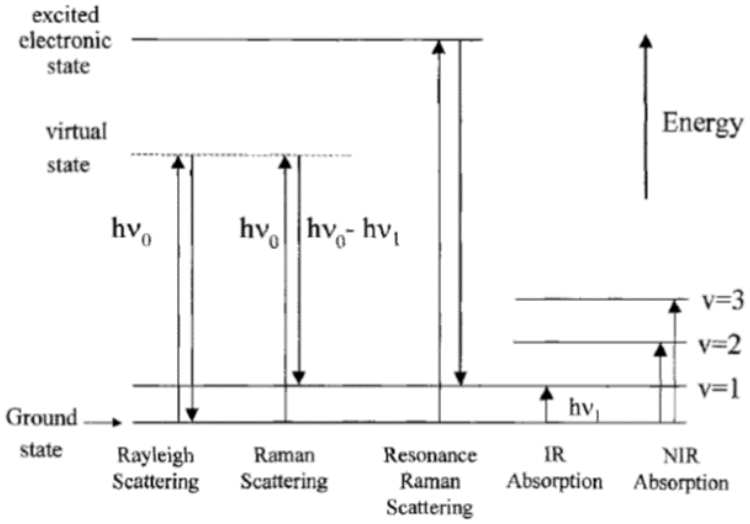

Figure 2.13: Transitions in vibrational spectroscopy - Raman non-elastic scattering is compared to other transitions. ν_0 is the frequency of exciting incident radiation and ν is vibrational quantum number. As featured in (75) p.2.

fiber with a 50 mm diameter. An air Olympus MPLAN (100x/0.90NA) objective was used. Raman scattered light was focused on a multi-mode fiber (100 mm diameter) and monochromator with a 600 line/mm grating. The excitation power of laser was 1 mW on the sample. Raman spectra were accumulated by 20 scans with an integration time of 20 s and a resolution of 3 cm^{-1}. The spectrometer monochromator was calibrated using the Raman scattering line of a silicon plate (520.7 cm^{-1}). The baseline correction, cosmic ray removal were done using WitecProjectFour software, while peak fitting analysis was performed using GRAMS software package.

3

Film characterization

3.1 Fabrication process

Rare-earth nickelate thin films can be obtained with a variety of techniques such as sputtering (67), pulsed laser deposition (15). However the preparation of stoichiometric compounds was proven to be difficult, both as bulk (powders) (13) and as thin films (RF sputtering) due to demanding preparation conditions. Formation of the stoichiometric phase requires either high oxygen partial pressure during growth or during subsequent post-annealing. The details can be found in an updated diagram for thermodynamical phase stability of $SmNiO_3$ assembled based on thermodynamical calculations conducted by Jaramillo et al. and on results obtained for different preparation conditions (61). What follows is that hardly any single process is able to produce stable $SmNiO_3$ thin films.

Standard DC magnetron sputtering uses plasma generated by direct current between the cathode (target) and anode. It is the most basic of sputtering methods that allows for fairly easy, fast deposition of metallic layers. However, it is not suitable for insulating compounds for which a positive charge build-up may arise due to anode ion bombardment and subsequent electron depletion in the target material. In that case the radio frequency (RF) magnetron sputtering method is used. Basic scheme of the method is presented in figure 3.1. This technique was applied for deposition of $SmNiO_3$ films in Université du Maine, Le Mans, France.

$SmNiO_3$ films were deposited on monocrystalline silicon Si(100) substrates. Silicon wafers are widespread materials of choice in the electronics industry for applications as chips and microchips in a variety of products to serve a variety of purposes. In view of possible applications of $SmNiO_3$ films it is reasonable to

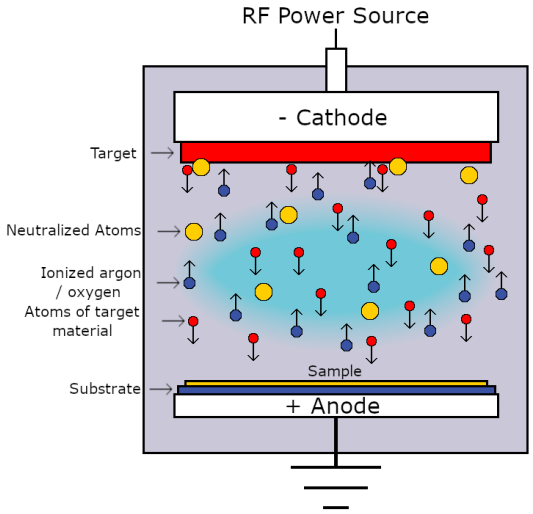

Figure 3.1: Scheme of Radio Frequency magnetron sputtering experiment - The argon/oxygen atoms are ionized in the deposition chamber, accelerated to the target material from which they sputter away the materials particles. The particles are deposited on the substrate which is at the same time the anode of the set-up.

study their properties as deposited on silicon. However, it was shown, that the growth of RNO phase is much easier on a substrate with a matching perovskite-like structure. In general the $SmNiO_3$ films have been grown by RF magnetron sputtering on various substrates like $SrTiO_3$, $LaAlO_3$, $SrLaAlO_4$ (9, 96) or by MOCVD on LAO(001) (57). The epitaxial SNO films were found to be stabilized easily on $LaAlO_3$ (LAO) with only a minor addition of other phases (33), due to the very small lattice mismatch that averages 0.1 %. Other perovskite-like substrates are not easily implemented, and the growth of a pure SNO phase without the large contribution of binary oxides like NiO or Sm_2O_3 was impossible, with an example of $SrTiO_3$(STO) (33). In order to improve the phase stabilization methods such as MOCVD band-flash injection were introduced (17).

A chemical route was also applied together with spin coating deposition of lighter rare-earth nickelates on LAO and STO (001) (72). La- and Nd-based nickelates were observed to grow epitaxially with small amount of polycrystalline phase, while films with Pr and Sm contained some binary oxide impurities in epitaxial films. In general, the single-phase was found to be stable up to 200 nm on LAO, while films with 500 nm thickness exhibited a significant amount of

Sm_2O_3 and NiO (33).

As for the monocrystalline silicon (100), the literature reports formation of several phases, such as polycrystalline SNO phase with a significant amount of binary R_2O_3 and NiO oxides which was attributed to larger lattice mismatch between film and substrate. However the films were deposited at low total pressure of 0.01 mbar ($Ar:O_2$ gas flow equal 1:1) at 923 K with no subsequent high-pressure annealing (9). In view of thermodynamic studies by Jaramillo et al. these conditions are not sufficient to form a stable $SmNiO_3$ phase, especially on a substrate with the non-matching crystal structure (61). The MOCVD technique on Si(001) gave similar results (substrate temperature of 680°C at 10 mbar of Ar and O_2 atmosphere at 1:1 ratio (57). Intermediate temperature and high oxygen pressure seem to be the best for stabilization of the proper phase.

For this work, thin films were deposited in pure argon (about 94 sccm gas flow rate) or in a mixture of argon and oxygen (flow rate of 60 and 12 sccm, respectively) atmosphere. The deposition time varied from 4 to 42 minutes. On average the working pressure inside the sputtering chamber during film deposition was about 5×10^{-2} mbar and the substrate temperature was held at about $870 \pm 5K$. The details regarding the deposition process are collected in table 3.1.

As of thermodynamic calculations data shown by Jaramillo et al. (61), the boundaries for the applied conditions are 600 K - 16 mbar and 800 K - 1.11 bar. Hence, the deposition conditions in this work were insufficient to form a stable $SmNiO_3$ phase. Therefore following the deposition, the samples were annealed under high oxygen pressure of about 180 mbar at about 1073 K. Initial applied pressure was 68 bar and was increased through heating of the chamber. The details of the process are given in table 3.2. The applied conditions allowed for the perovskite phase stabilization.

Manufactured films on silicon substrate are referenced with code names that include information about the sputtering duration in minutes, type of plasma composition ($Ar/Ar+O_2$) and the presence (w) or absence (n) of subsequent post-annealing. For example S-30AOn is a SNO film sputtered for 30 minutes in mixed argon/oxygen atmosphere and not subjected to annealing procedure.

Table 3.1: Details of magnetron sputtering process of $SmNiO_3$ thin films. Two groups of samples were deposited either in mixed argon and oxygen atmosphere or pure argon. For each atmosphere the deposition time was varied. Also, one sample from each group was not annealed - that is S-30AOn and S-42An. (*) additional cleaning in ultrasonic cleaner in methanol, (+) minor instability of incident power, (-) gauge off. Sample code name includes information about the sputtering time value in minutes, type of plasma composition (A/AO) and the presence (w) or absence (n) of subsequent post-annealing.

Stage	Parameter	S-4AOw	S-12AOw	S-24AOw	S-30AOn	S-30AOw	S-36AOw	S-42AOw	S-5Aw	S-42An	S-42Aw
Substrate	cleaning mixture ratio	1:1	1:1	1:1	1:1	1:1	1:1	1:1	1:1	1:1	1:1
	(methanol-sulphuric acid)										
cleaning	cleaning duration, min	15	15	15	15	15	15	15	30	15	15
	comments	(*) 5min	(*) 10min	(*) 5min	(*) 3min	(*) 3min	-	(*) 5min	-	-	-
Preparation	preliminary pressure, mbar	3.2×10^{-6}	4.2×10^{-6}	2.0×10^{-5}	4.3×10^{-6}	4.3×10^{-6}	6.0×10^{-5}	3.7×10^{-6}	3.4×10^{-6}	-	-
to sputtering	plasma cleaning of target, min	10	10	10	10	10	10	10	10	10	10
	pressure, mbar	0.102	0.1	0.1	0.1	0.1	0.1	0.1	0.1	0.1	0.1
	T_{substr}, K	862±5	803	869±5	850±5	850±5	869±5	865±5	873±5	869±5	869±5
magnetron off	Ar flow, sccm	94.1	94.4	93.9	93.9	93.9	94.1	94	93.9	93.8	93.8
	(O_2 flow was zero)										
	Pump speed, krpm	41	41	41	41	41	41	41	41	41	41
	Incident Power, W	50	55-50	50	50	50	50	50	50	50	50
Magnetron on,	Circuit Voltage, V	160	210	160	160	160	160	160	160	160	160
O_2 flow off	Comments	-	-	(+)			(+)		-	-	
	pressure, mbar	0.102	0.1	0.1	0.1	0.1		0.1	3.1×10^{-6}	(-)	(-)
	Ar flow, sccm	60.1	59.80	60	60	60	60.1	60.1	-	-	-
	O_2 flow, sccm	12	12.00	12	12	12	12.1	12	-	-	-
Magnetron on,	Atmosphere	$Ar+O_2$	$Ar+O_2$	$Ar+O_2$	$Ar+O_2$	$Ar+O_2$	$Ar+O_2$	$Ar+O_2$	Ar	Ar	Ar
O_2 flow on	Incident Power, W	45	50	50	50	50	50	45	nd	nd	nd
	(Reflected Power was zero)										
	Circuit Voltage, V	200	200	200	200	200	200	200	nd	nd	nd
	T_{substr}, K	870±5	869±5	869±5	868±5	868±5	871±5	870±5	(-)	(-)	(-)
	sputtering time, min	**4**	**12**	**24**	**30**	**30**	**36**	**42**	**5**	**42**	**42**
	Working pressure, mbar	5.5×10^{-2}	5.2×10^{-2}	5.22×10^{-2}	5.3×10^{-2}	5.33×10^{-2}	5.3×10^{-2}	5.3×10^{-2}	(-)	(-)	(-)
	Comments	-	(+)	(+)	(+)	(+)	(+)		-	(+)	(+)
	final pressure, mbar	-	2.7×10^{-3}	-	-	-	-	4.4×10^{-3}		3.6×10^{-6}	3.6×10^{-6}
	T_{substr} at evacuating sample	364	309	355	298	298	363	363	303	303	303

Table 3.2: Details of annealing process of $SmNiO_3$ thin films. Three sessions of annealing procedure were held. (*) 2 min O_2 spraying in pressure reactor, additional cleaning in ultrasonic cleaner in ethanol for 15 min. (**) initial 4h 15min sample spent at 295 K and 68 bar O_2 with no heating. Sample code name includes information about the sputtering time value in minutes, type of plasma composition (A/AO) and the presence (w) or absence (n) of subsequent post-annealing.

Stage	Parameter Atmosphere	S-4AOw $Ar+O_2$	S-12AOw $Ar+O_2$	S-24AOw $Ar+O_2$	S-30AOn $Ar+O_2$	S-30AOw $Ar+O_2$	S-36AOw $Ar+O_2$	S-42AOw $Ar+O_2$	S-5Aw Ar	S-42An Ar	S-42Aw Ar
	interval between deposition and annealing	1d 5h	4d 20h	7d		4d 1h	4d 12h	7d	7d		1d 5h
	annealing session	1.	2.	3	-	2.	2.	3	3	-	1.
Initial parameters	T_{set}, K	1073	1073	1073	-	1073	1073	1073	1073	-	1073
setup	temperature increment [K/min]	5	5	5		5	5	5	5	-	5
	preliminary operation	(*)	(*)		(*)	(*)	(*)			-	(*)
	$T_{initial}$, K	295	299	298	-	299	299	298	298	-	295
	$p_{initial}$, bar	68	68	68	-	68	68	68	68	-	68
Annealing	p_{anneal}, bar	182	175	180		175	175	182	180	-	182
	T_{anneal}, K	1068	1066	1068	-	1066	1068	1068	1068	-	1073
	T_{final}, K	296	nd.	nd.	-	nd.	nd.	nd.	nd.	-	296
	p_{final}, bar	60	nd.	nd.	-	nd.	nd.	nd.	nd.	-	60
	Comments	(**)	-	-		-	-	-	-	-	(**)

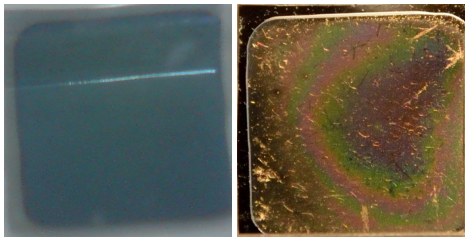

(a) **(b)**

before annealing after annealing

Figure 3.2: Comparison of macroscopic optical images of sample S-12AOw surface before and after annealing. The streak in the surface before annealing is an artefact, the colour and resolution are blurred by the sample plastic packaging.

The target material for thin film deposition was prepared by Peccini sol-gel method, which was burnt afterwards to obtain a powder. The powder was next pressed in the isostatic press and sintered at 800°C for 12 hours into pellets, which were used as a target (Sm_2NiO_4 and NiO mixture). Three additional nickel pellets of 4 mm in diameter were added on top of the target in order to obtain films with Sm/Ni ratio close to 1.

All substrates used for deposition were at first cleaned *ex-situ* by wet chemical methods. Wet chemical etching with a mixture of methanol and sulphuric acid should remove several nm of the outer layer (mostly SiO_2 along with contaminations). After the etching substrates were washed with distilled water. Next, the substrate was transported into the deposition chamber and heated up to the deposition temperature in approximately 30 minutes. Simultaneously with substrate heating, neutral argon gas was introduced into the chamber. When the desired substrate temperature was reached, the magnetron was switched on and argon formed plasma which was used for 10 min cleaning of the substrate. Subsequently, the oxygen was flown to the chamber and after about 3 minutes the deposition started.

Although the annealing process allows for achieving the required structure stabilized, it is highly unfavourable. The extreme conditions during annealing limit some of the future uses of the films. On top of that, the process is highly destructive to the surface of the film. It also has some other disadvantages such as chromium contamination (from the sample production chamber). The applied process required putting the film in a small closed vessel where the extreme conditions could be obtained.

The surface of the film just after deposition is macroscopically even, flat and reflecting. The exemplary surface of S-42An sample is presented in figure 3.4(left). The surface is 'colourful', where different colours form waves on the sample surface. It is the microscopic differences in surface thickness that manifest in colour variations which will be discussed later. Annealing process enhances these visible irregularities. The process is also more damaging to the surface. Microscopic observations indicate that the surfaces contain various species formed in the shapes of capillaries and bubbles as seen in figures 3.4(right) and 3.3. Some of the tubes seem to be located under the films surface and others are partially under and partially at the surface. The front and back of the tubes indicate they might be small capillaries - empty inside. The bubbles are made of spherical grains surrounded by the film's matrix in the form of concentric spheres which may be a form of diffusion zone of the material. The structure of the film is modified around them which is demonstrated in the change of the film's colour. These species may also be of different crystallographic phase, however, this was not to be confirmed by the used experimental techniques.

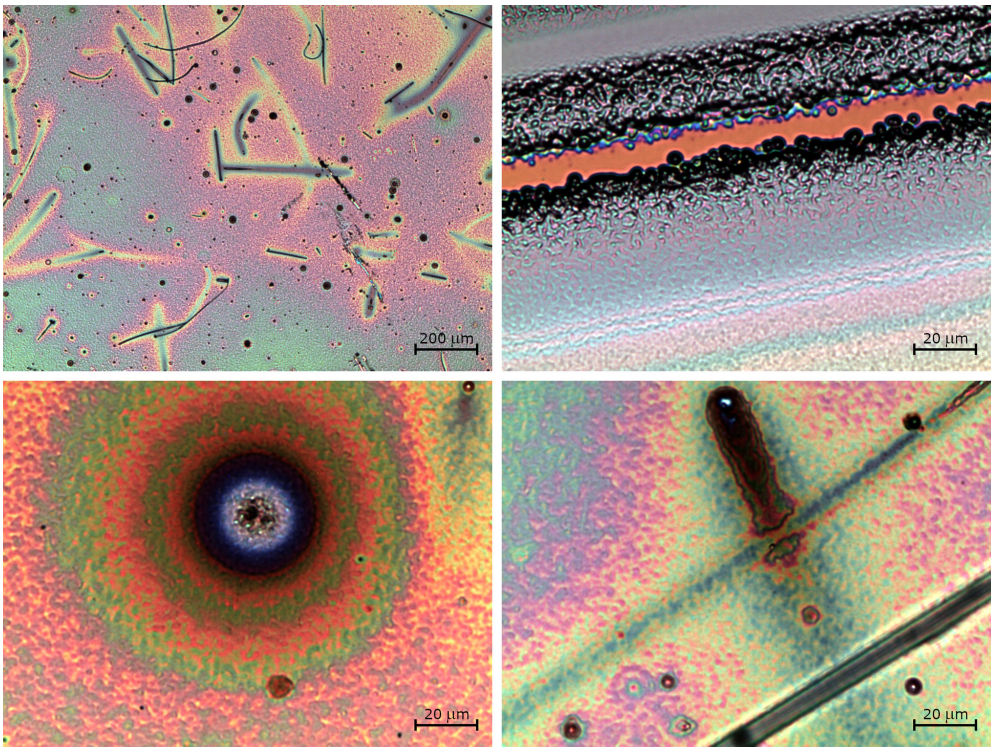

Figure 3.3: Surface after annealing - Microscopic image of S-12AOw film after annealing.

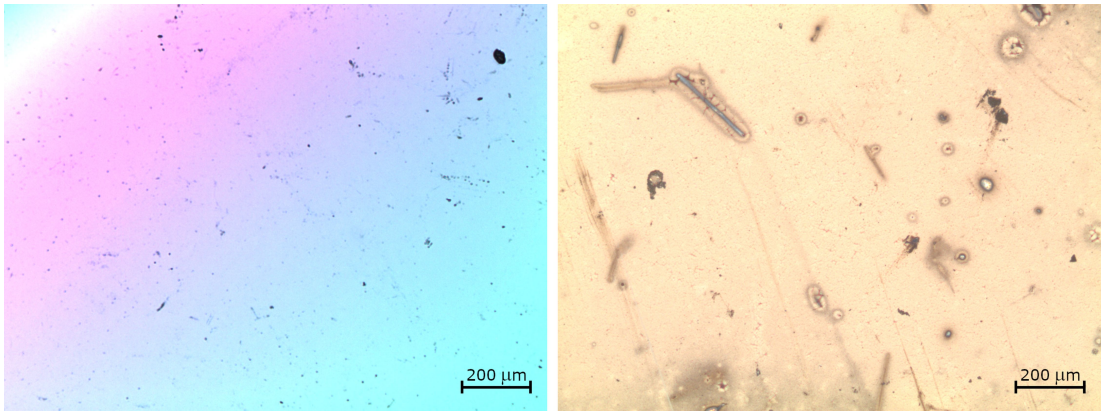

Figure 3.4: Surface images of S-42An film - Microscopic images before (left) and after annealing (right) process. As-deposited sample is smooth and has minor defects, whereas defects in structure of the annealed film are much larger and inhomogeneous.

3.2 Chemical composition

The applied measurement techniques allowed for comparison of chemical composition of the films treated as a bulk with data obtained from microscopic techniques which gave more insight into the details of elemental distribution. X-ray Fluorescence Spectroscopy was used as a bulk measurement technique, whereas X-ray Photoelectron Spectroscopy and Secondary Ion Mass Spectroscopy were used to investigate the chemical composition in more detail at the surface and as spatial distribution.

3.2.1 Bulk chemical composition

The macroscopic investigation of the chemical composition of thin films was done by XRF. It allowed for mapping surfaces of the obtained samples with respect to the distribution of nickel and samarium as well as relative composition of the two elements. In figure 3.5 images of the distribution of main constituent metal element oxides in the sample S-12AOw is displayed. The distribution of samarium oxide and nickel oxide is quite homogeneous. The relative distribution of Sm_2O_3 and NiO seems homogeneous as well.

The correlation of quantitative content of the two metals in the film indicates that the amount of samarium is slightly larger than nickel, however, the ratio is

over 0.95 for the sample S-12AOw. The differences appear in spatial dependence of film thickness - there is a gradient of film thickness, and the absolute thickness ranges from about 100 to 130 nanometers. The thickness evaluation was done using XRF Fundamental Parameters method and the resulting data was processed using Origin software. The raw data measured with 250 μm resolution, however, it was smoothed and reconstructed for clarity (the resolution was artificially increased and the data was averaged over the nearest neighbour points).

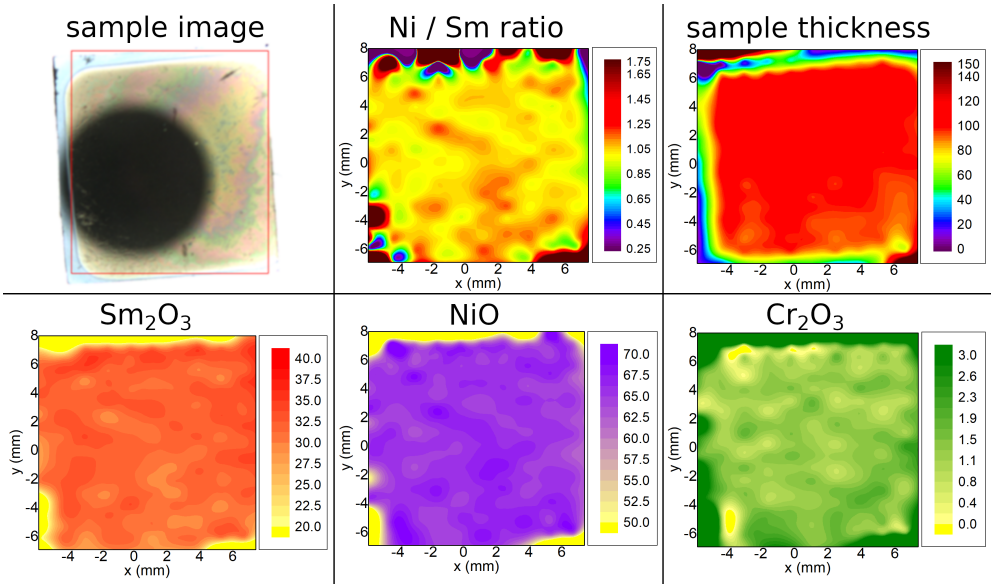

Figure 3.5: Macroscopic elemental distribution and thickness of S-12AOw thin film - Calculated from XRF and visualized by estimation and approximation by nearest neighbours. Distribution of nickel, samarium and chromium element is shown. Additionally Ni:Sm atomic ratio and sample thickness distribution as well. The sample as seen on XRF camera and analysis area defined in red rectangle in the first image.

Sample S-24AOw exhibits a gradient in chemical composition as well as in thickness (figure 3.6). The differences, however, are relatively small. The biggest variation of the thickness can be found on the edge of the sample, while in the centre of the sample, there is very little variation.

It should be noted that there was only a part of the sputtered S-30AOn film that was cut away in order to investigate the material before high temperature and pressure annealing. Therefore what is presented is an unannealed part of S-30AOn sample. The distribution of elemental concentration is quite homogeneous,

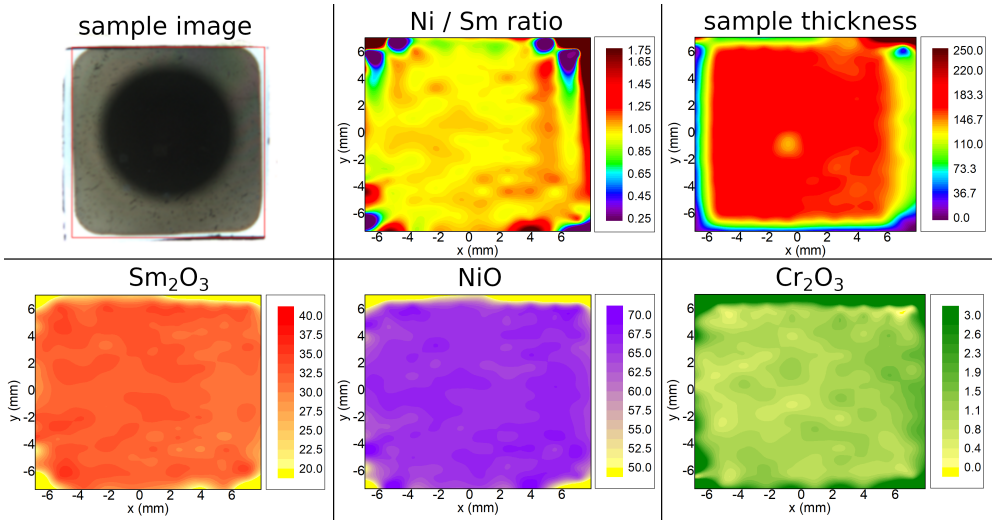

Figure 3.6: Macroscopic elemental distribution and thickness of S-24AOw thin film - Calculated from XRF and visualized by estimation and approximation by nearest neighbours. Distribution of nickel, samarium and chromium element is shown. Additionally Ni:Sm atomic ratio and sample thickness distribution as well. The sample as seen on XRF camera and analysis area defined in red rectangle in the first image.

however, for NiO, a small gradient in concentration is evidenced (figure 3.7). The amount of chromium oxide is close to zero at the film's surface. Again, there is some thickness variation, however, it is limited to the edge of the sample.

The S-42Aw sample deposited in pure argon plasma had been exposed to high temperature and high pressure of oxygen which affected the film stability. The sample after deposition nor after 38-hour annealing did not show any signs of damage, surface discontinuities or sharp changes of structure or colour. However subsequent experiments in high vacuum caused partial defragmentation of the film. A closer look under the microscope reveals a puzzle-like structure with the surface being formed of little polygons 3.8. These are parts of the defragmented film. The closer to the film interior, the further away the polygons are of each other. The closer to the film edge, the film becomes more continuous and is more coherent. Also, every uncommon part of the surface is a source of film damage. For example, the film is more damaged around capillary and bubbles. A possible explanation for that would be the film is too thick and has too low density in order to stabilize the structure and adhesion to the highly mismatched substrate. It is worth noting that although silicon wafers were used as a substrate, most

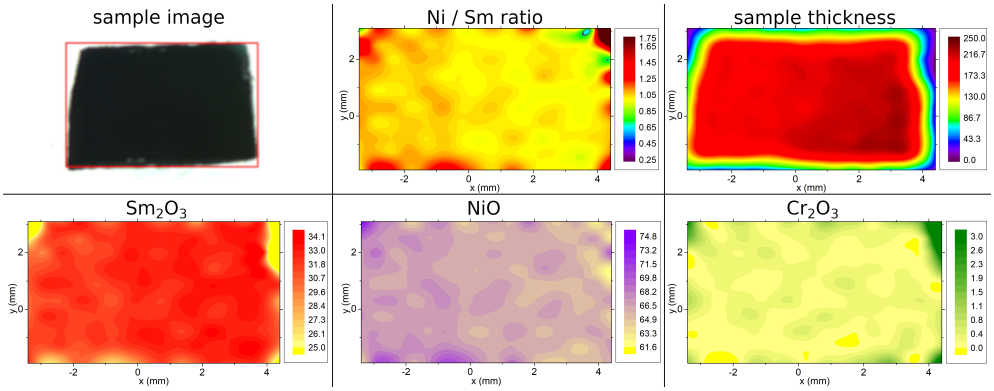

Figure 3.7: Macroscopic elemental distribution and thickness of S-30AOn thin film - Calculated from XRF and visualized by estimation and approximation by nearest neighbours. Distribution of nickel, samarium and chromium element is shown. Additionally Ni:Sm atomic ratio and sample thickness distribution as well. The sample as seen on XRF camera and analysis area defined in red rectangle in the first image. Chromium content is very low, below 0.4 at.% in comparison with the annealed samples.

probably at the interface there is an oxidized layer of silicon of unknown crystal structure.

The distribution of samarium and nickel, as well as other maps, are presented in figure 3.9. The distribution of the chemical elements appears to be rather homogeneous. Only thickness is not homogeneous in all films which is a common feature of films deposited by a sputtering method (especially at the film edges).

As one could expect, the film thickness increases with sputtering time as evidenced in figure 3.10. The thickness for films deposited in argon atmosphere (A) is about twice as large as of the films deposited in a mixed atmosphere (AO). The dependence of film thickness on sputtering time is rather monotonic, however, it varies more for the samples deposited in argon. At small deposition times, the film is growing fast but quickly reaches the maximum point from which the growth speed decreases. This would suggest that the film exhibit an island growth at the beginning. The islands start to form, they attract new impinging species and grow fast. After some time most of the impinging atoms locate themselves in between the island forming layers, which is a slower process. This type of growth is called a mixed layer-island or Stranski-Krastanov type of growth (42). In Volmer-Weber type of growth, the interactions between the impinging atoms (adatoms) are stronger than the attraction of adatoms to the surface, therefore it

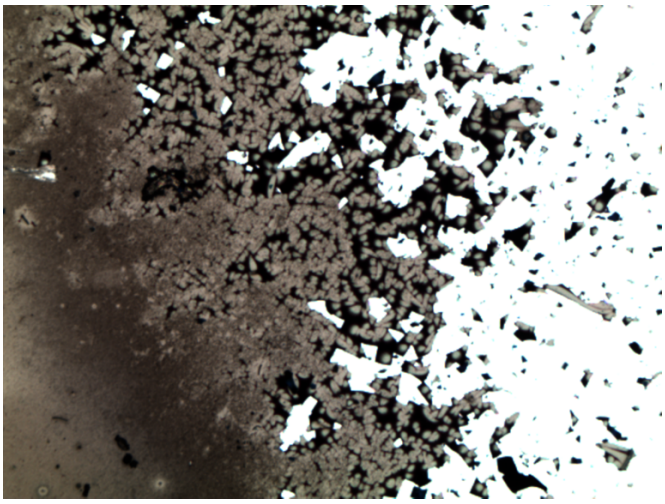

Figure 3.8: Miscroscopic image of S-42Aw film after damage under high vacuum conditions - A gradient of sample damage is shown, where the most damaged part is separated into many small polygonal pieces.

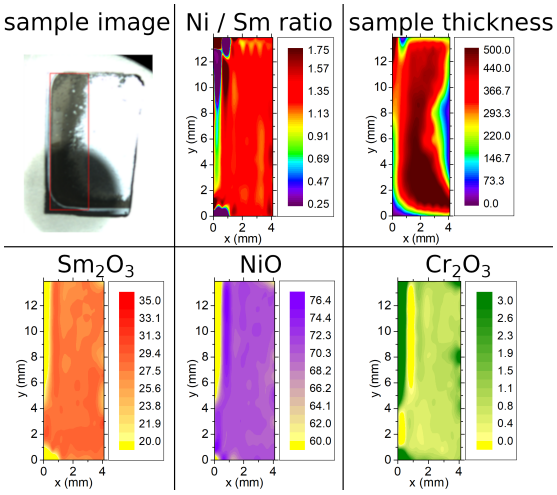

Figure 3.9: Macroscopic elemental distribution and thickness of S-42Aw thin film - Calculated from XRF and visualized by estimation and approximation by nearest neighbours. Distribution of nickel, samarium and chromium element is shown. Additionally Ni:Sm atomic ratio and sample thickness distribution as well. The sample as seen on XRF camera and analysis area defined in red rectangle in the first image.

is easier to form a 3-dimensional cluster of adatoms/ islands. In this mode, rough multilayer films are grown. This has not been observed for Ar films due to lack of data (samples), however, the estimated film growth speed has also diminished for argon films. Assuming equal sputtering rate, this implies that the thicker films are denser than the thinner films.

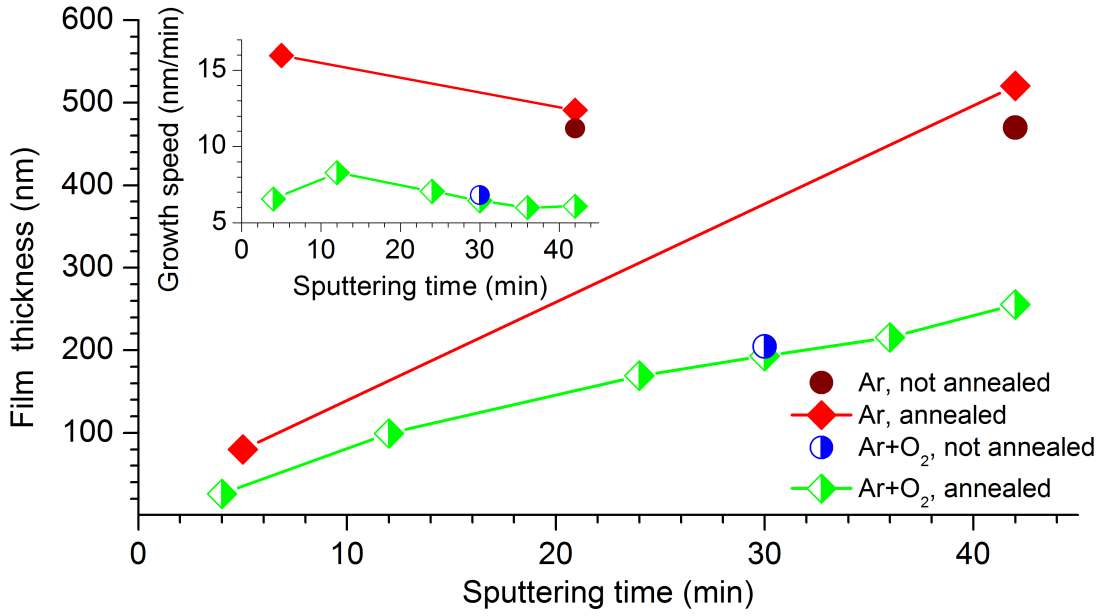

Figure 3.10: Growth speed of $SmNiO_3$ thin films - Calculated from XRF.

What is more, the experiments revealed that the films contain additional elements such as chromium and iron, which are deposited on the film during the high-pressure annealing process. The contaminants are not present in films that did not undergo annealing. However, the annealing procedure was essential to obtain the proper crystallographic phase.

The elemental distribution was found to be quite homogeneous in all films, with very slight variation of the composition as shown in the maps. However a significant influence of the sputtering atmosphere was detected, as evident from the Sm:Ni atomic ratio (figure 3.11 c). For the films grown under $Ar+O_2$ atmosphere, the ratio is only slightly below 1 with a small surplus of nickel with respect to samarium atomic content. Whereas, the films grown in pure argon have a large Ni surplus and the Sm:Ni ratio varies from 0.75 to 0.85. Additionally, the Sm:Ni ratio depends slightly on the film thickness, and approaches 1 for thicker films. The annealing process did not affect neither the thickness nor the Sm:Ni atomic

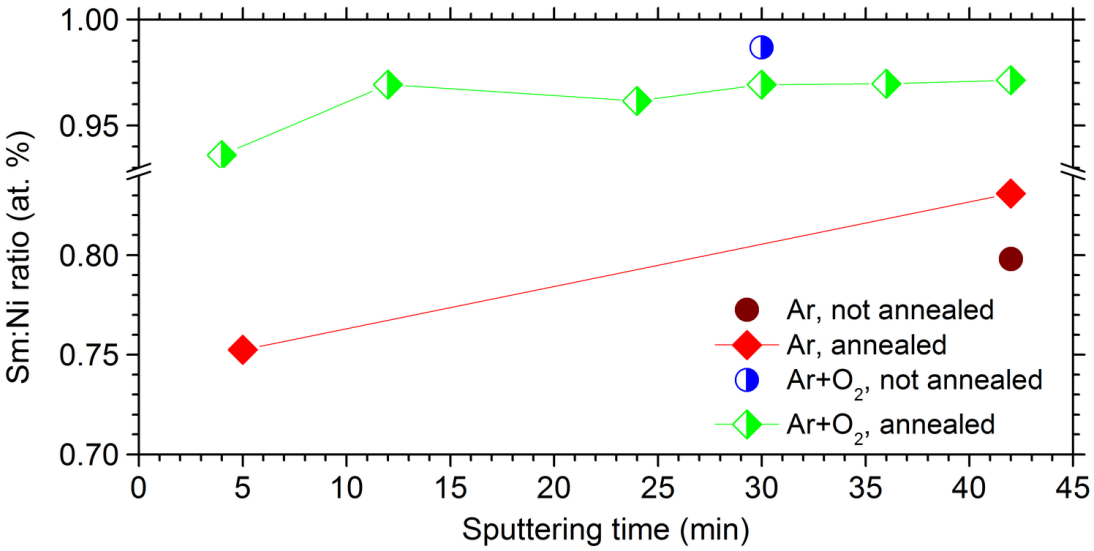

Figure 3.11: Sm/Ni atomic ratio in $SmNiO_3$ thin films - Calculated from XRF measurements.

ratio significantly.

3.2.2 Surface chemical composition

Detailed investigation of chemical content of SNO films was done with XPS and TOF-SIMS.

The films are rather homogeneous in-plane (figure 3.12) but mostly also along the z-axis as depicted in figure 3.13. Distribution of samarium is homogeneous. However, the surface region contains less nickel than the lower layers of the films, also close to interface there is an increased SIMS intensity for a nickel. The surface region is probably full of carbon and oxygen-based contaminants. Chromium is located mainly in the surface region, however, the atoms seem to have diffused or had been pressed inside the films' structure as a result of the prevailing conditions in the high-pressure chamber. That drew limitations on the subsequent experiments. The silicon atoms which form the substrate are found in some quantity in the film's volume. Interestingly there are more silicon atoms on the surface and in the vicinity of the interface at the film's side than dispersed within the film capacity. The interface is not distinctly defined but rather there is a wide diffusion zone.

XRF studies revealed that the process of annealing apart from stabilizing

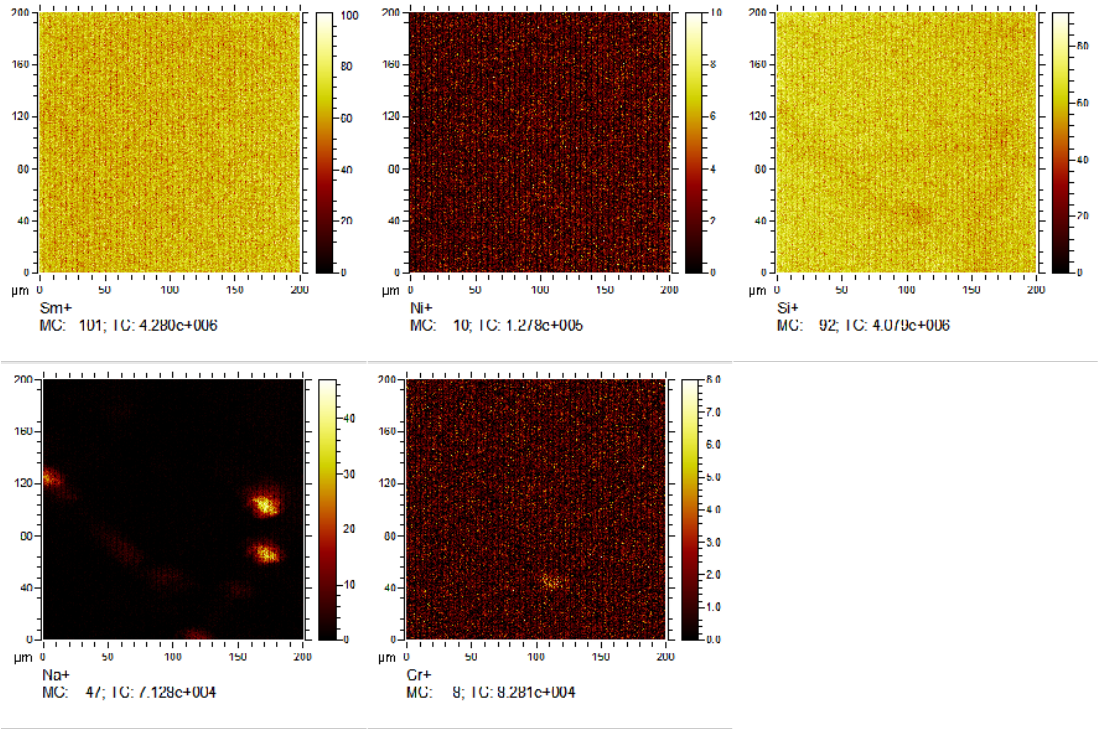

Figure 3.12: Surface distribution of elements in sample S-12AOw. - A homogeneous distribution of samarium and nickel, with a slightly depleted surface area in favour of oxidized chromium presence.

the distorted perovskite structure of samarium nickelate, also causes build-up of contaminations on the surface of deposited films. Contamination of annealed film includes mainly chromium. However XRF experiments do not specify in what chemical form chromium is present on the surface. That was resolved by X-ray photoelectron spectroscopy experiments. As shown un comparison between survey spectra of S-42Aw and S-42An samples (figure 3.14) there is a difference in composition between the annealed and as-deposited sample. The main $2p_{3/2}$ chromium line was resolved and according to literature its components correspond to, among others, chromium oxides Cr_2O_3 (54), CrO_3 (10), Cr_2O (58) or complex metal oxides (10). The fitting of chromium spectrum in sample S-42Aw is shown in figure 3.15

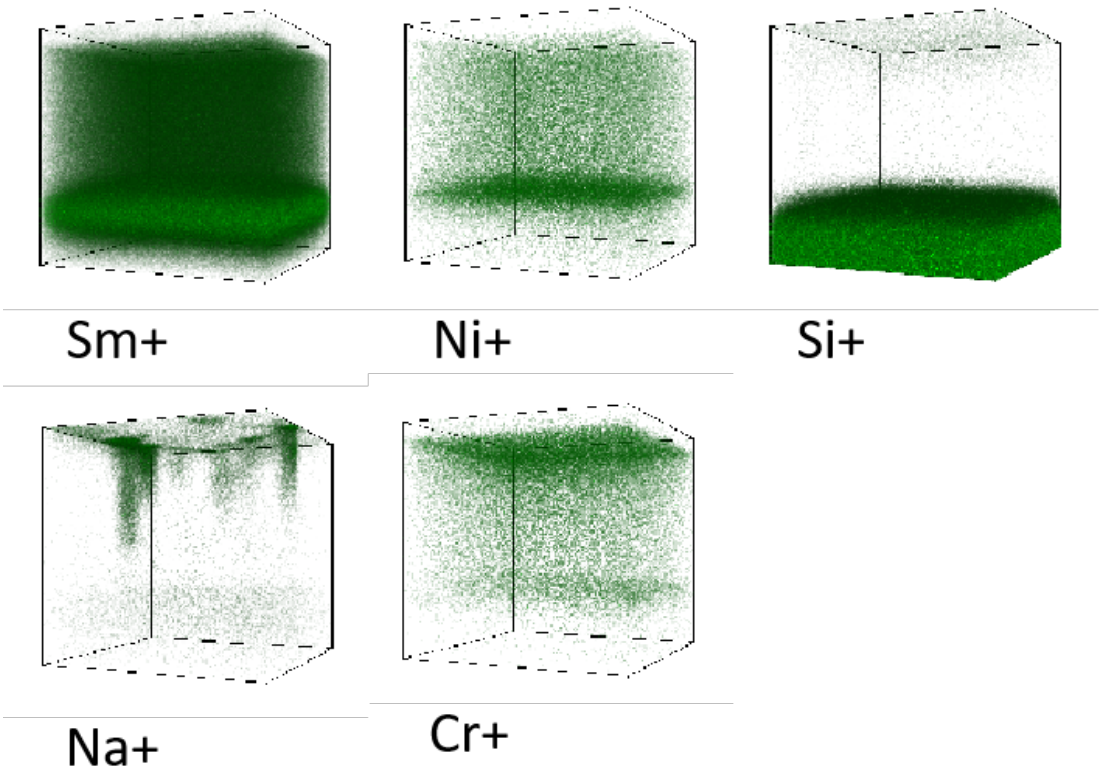

Figure 3.13: Spatial distribution of elements in sample S-12AOw. - A homogeneous distribution of samarium and nickel, with a slightly depleted surface area in favour of oxidized chromium presence. Chromium, silicon as well as other elements are found partially in the film's volume.

3.3 Structural characterization

Thermodynamic conditions during the deposition process as well as further post-treatment or the lack of it, have greatly influenced the structure of obtained $SmNiO_3$ films. Films were deposited on silicon (100) substrates, which is the first obstacle to obtain the proper crystallographic phase. The structure of silicon crystal is an fcc cubic diamondlike structure while the nickel-samarium perovskite oxide crystallizes in orthorhombic/monoclinic structure. A comparison of their lattice parameters yields a certain lattice mismatch parameter which is larger for silicon than for example for perovskites like substrates such as $LaAlO_3$ or $SrTiO_3$. When the mismatch is high, there is not enough nucleation site for a

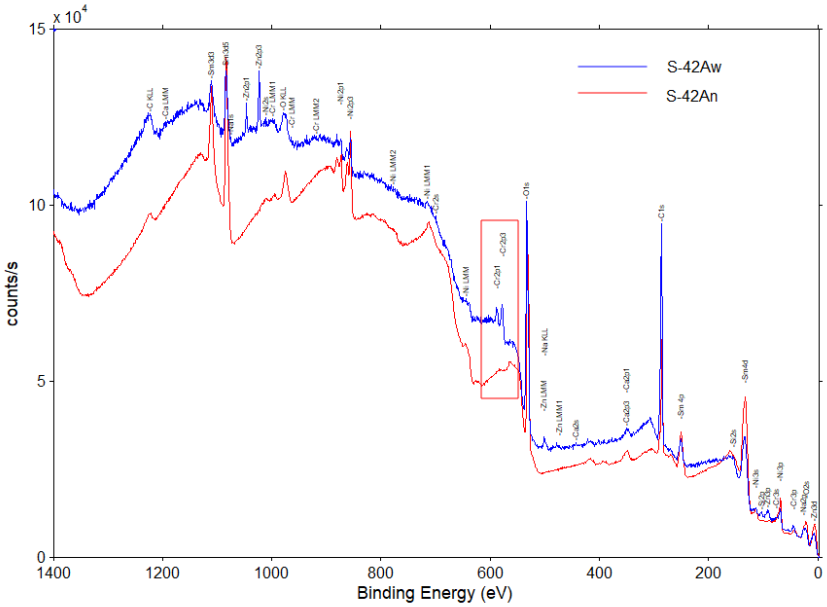

Figure 3.14: Survey spectra of sample before (red) and after (blue) annealing of S-42Aw and S-42An deposited in pure argon atmosphere - Apart from clear presence of samarium, nickel and oxygen elements, the spectrum of annealed sample contains chromium (in red frame) and other contamination.

proper structure to crystallize, this leads either to a strong structural distortion or formation of different crystallographic phases.

$SmNiO_3$ films were deposited under various atmospheres. For most of them, argon/oxygen atmosphere was used, because as expected and proven the mixed plasma yields more stoichiometric films. Pure argon plasma was used for deposition very thin and thick films - 4 and 42 minutes deposition time. Out of curiosity, some of the newly deposited films were cut into two parts in order to investigate their crystalline structure before high-pressure oxidation. The 30-minute film deposited in $Ar+O_2$ plasma and 42-minute Ar deposited film were chosen. The rest of the samples were taken to the high-pressure chamber and annealed in high temperature and high oxygen pressure.

In figure 3.16 the diffraction patterns of each of the prepared thin films are collected and compared according to the preparation conditions. A reference pattern of a measured pure $SmNiO_3$ powder is given. It is easy to see that there are substantial differences between the patterns. Description of each of the pattern is given below. Films that were deposited with magnetron sputtering after depo-

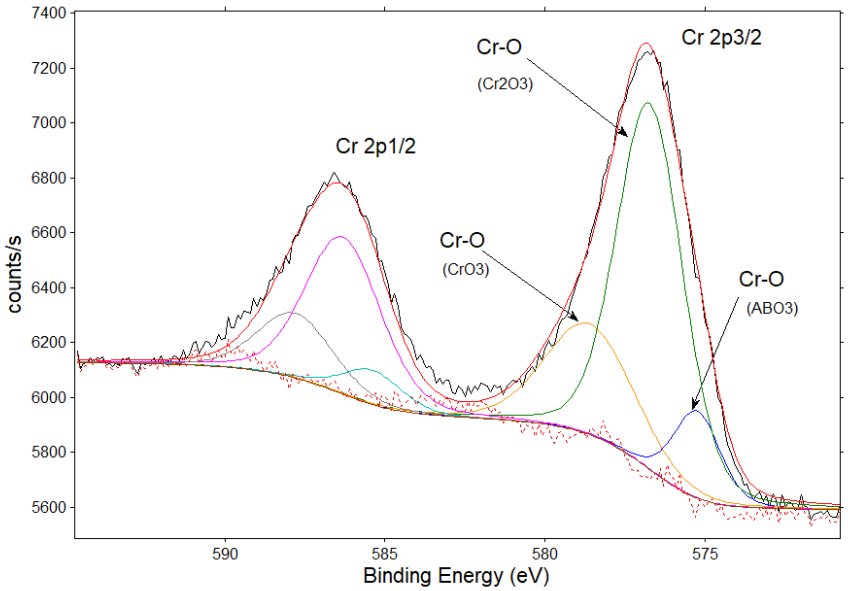

Figure 3.15: Chromium 2p XPS envelope in sample S-42Aw. - Apart from clear presence of samarium, nickel and oxygen elements, the spectrum of annealed sample contains chromium (in red frame) and other contamination. Chromium is present in oxidated form as Cr_2O_3, CrO_3. Small component of the spectrum corresponds to a ternary or quaternary compound.

sition do not present any diffraction peaks coming from the film that would be equivalent to long-range crystallographic order. Instead, a pattern with a broad ridge around 29 and 31 degrees 2θ is evident. Those ridges are quite close to the (110)(002) and (111) Bragg reflections from the orthorhombic form of $SmNiO_3$ compound.

The three peaks that appear at about 44, 51 and 76 degrees 2θ are best described by the aluminium sample holder shifted due to its spacial position in the measurement table of diffractometer. During the deposition, the temperature of the substrate is about 600 °C which gives a thermal energy k_BT equal to 0.075 eV. The thermodynamic conditions - temperature and partial oxygen pressure - are not enough to form a well-crystallized film. It does also matter whether the atmosphere is pure argon or mixed argon-oxygen.

Diffraction patterns of films deposited in an argon atmosphere for 5 and 42 minutes are presented in figure 3.17. The films were further annealed. Both samples present a polycrystalline film pattern with no evident crystalline texture. The

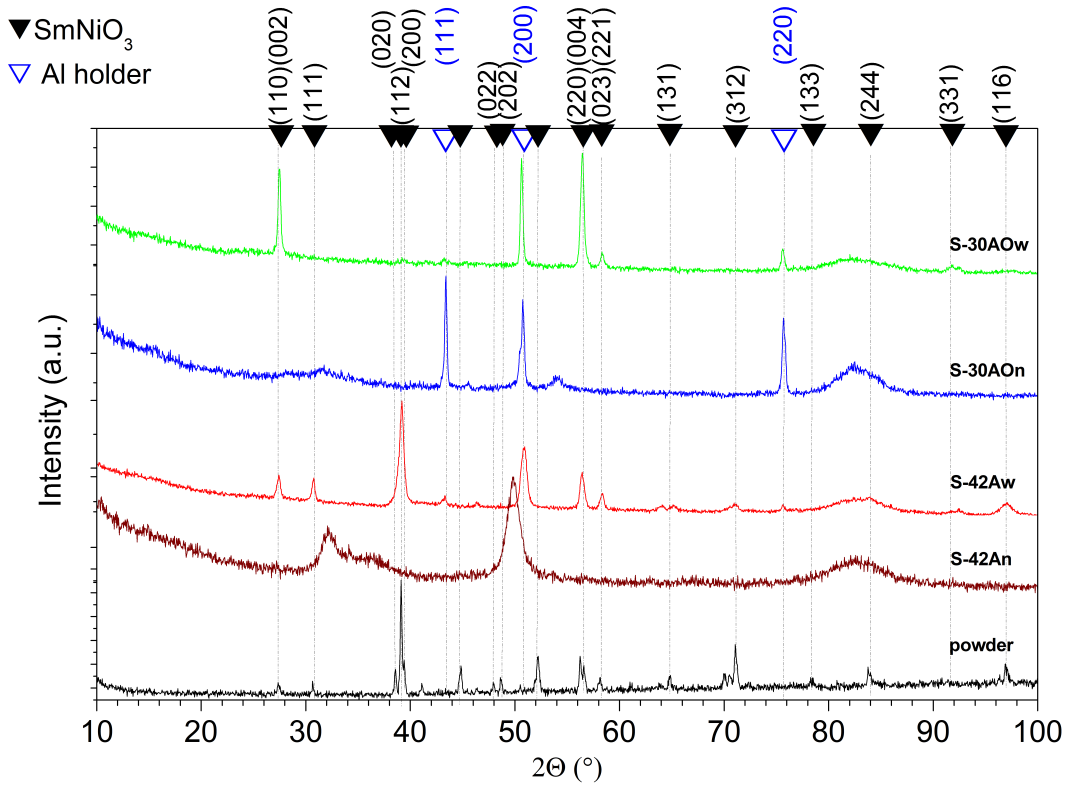

Figure 3.16: X-ray diffraction patterns of $SmNiO_3$ - Comparison between diffraction patterns obtained in various conditions yields that only annealed films have the distorted $SmNiO_3$ perovskite structure stabilized, while the as-deposited do not show almost any crystal structure. Deposition in pure argon atmosphere yields a polycrystalline film while films deposited in mixed $Ar+O_2$ atmosphere show strong crystalline texture.

thinnest film is very transparent and a strong contribution from silicon substrate at about 82 2θ is present. According to XRF measurements, the film is only as thin as 80 nanometers, which is possibly not that small as to uncover the substrate however during annealing the surface of the film was strongly damaged. For the thinnest film it is also evident that a broad ridge appears between 20-30 degrees 2θ, that could be an indicator of the presence of amorphous silicon dioxide.

A very different crystallographic structure is observed for the films deposited in the atmosphere of a mixture of argon and oxygen plasma gas, after annealing. Most of the films, apart from the thinnest one, shows a very strong crystallographic texture. The intensity is enhanced for the peaks identified as (110)(002)

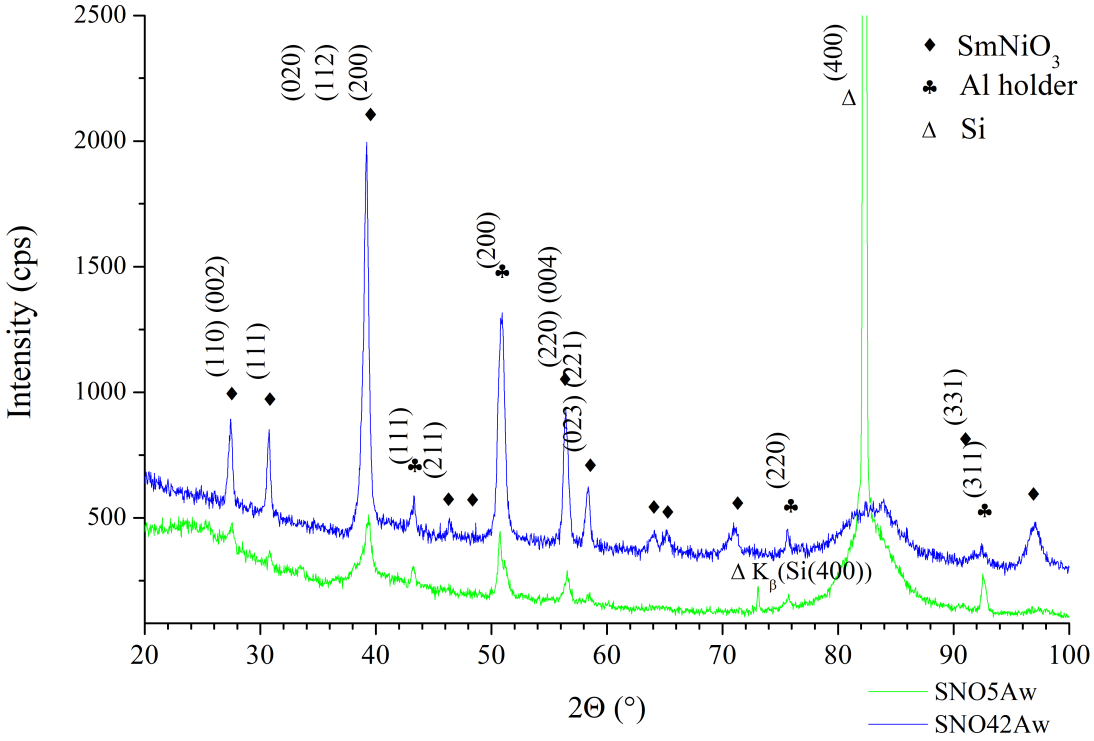

Figure 3.17: X-ray diffraction patterns of $SmNiO_3$ thin films deposited in argon plasma and annealed. - Both samples present a polycrystalline $SmNiO_3$ structure. The Bragg peaks are wide most probably due to, apart from strain, nanometric size of crystallites they are build of.

and (220)(004) when compared to the polycrystalline pattern displayed for example by the $SmNiO_3$ powder. Large peak broadening does not allow to resolve peaks (110) from (002). The thinnest film shows also some other peaks that have not been ascribed to any crystalline phase. This film seems to have a high amorphous phase contribution, given the broad hump between 35-65 degrees 2θ.

The crystallographic texture was investigated with X-ray diffraction pole figure method. Pole figures of (110)(002) planes were recorded at 27.24 °2θ. The obtained figure is a combination of signal obtained from the film and from the monocrystalline silicon substrate. In the description of pole figure measurements, it is important to note that the X-ray radiation used for the experiments was only filtered. Therefore most of the $K\beta$ radiation was filtered out, but a significant component of $K\alpha_2$ contributes to some smearing of the obtained intensity. It is also important to note that the focusing plane during X-ray diffraction ex-

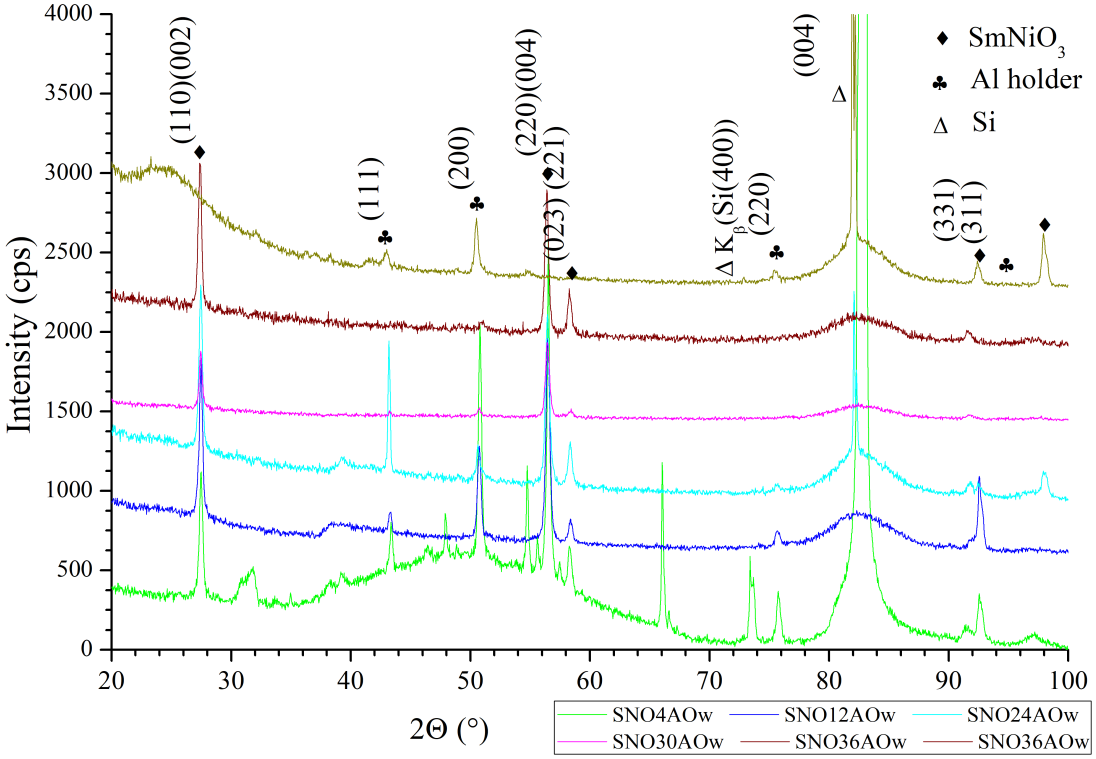

Figure 3.18: X-ray diffraction patterns of $SmNiO_3$ thin films deposited in argon-oxygen plasma and annealed. - A strong crystalline texture is evident for most of the samples. The thinnest one shows additional contribution of amorphous phase and other unidentified crystalline phases. The thickest one due to some damage does not present a strong intense Bragg peaks.

periment is at the specimen surface, which is the top layer of the deposited film. The surface of the silicon substrate is tens or hundreds of nanometers below the focusing plane. This should result in an unavoidable shift/displacement of the signal obtained from the silicon substrate.

When the pole figure is collected for (220)(004) planes, i.e. at 56.28°2θ the pole figure looks quite different (figure 3.21). The signal from the four distinct spots at about 45°2θ is very large and reaches about 23k counts. This alone suggests that the signal comes from a highly crystalline phase with cubic crystal symmetry. It is fair to assume that the signal comes from the monocrystalline silicon substrate and can be identified as 111 set of crystal plane normals in reciprocal space. According to the (The Rigaku Journal, 27(2), 2011, the technical article entitled "X-ray thin film measurement techniques VII. Pole Figure Mea-

Table 3.3: Orthorhombic unit cell parameters of refined diffraction patterns of all obtained $SmNiO_3$ thin films and the silicon substrate. Mean pseudocubic parameters $\overline{a_p}$ and lattice mismatch are given. All samples present tensile strain, larger for more ordered films deposited in mixed argon-oxygen atmosphere.

sample	a, Å	b, Å	c, Å	$\overline{a_p}$, Å	lattice mismatch, %
S-4AOw	5.309(6)	5.411(6)	7.55(2)	3.786	1.40% (tensile)
S-12AOw	5.321(6)	5.404(6)	7.57(2)	3.790	1.30% (tensile)
S-24AOw	5.335(3)	5.401(3)	7.58(2)	3.793	1.21% (tensile)
S-30AOw	5.334(4)	5.402(4)	7.57(2)	3.792	1.25% (tensile)
S-36AOw	5.327(3)	5.406(3)	7.55(1)	3.789	1.32% (tensile)
S-5Aw	5.313(3)	5.433(3)	7.602(8)	3.800	1.03% (tensile)
S-42Aw	5.328(2)	5.411(2)	7.576(2)	3.794	1.19% (tensile)
Si	5.4301(2)	5.4301(2)	5.4301(2)	3.840	-

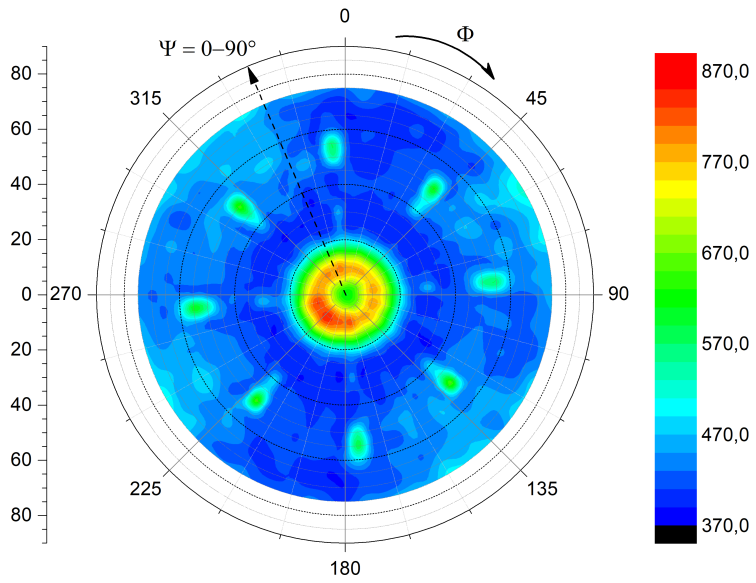

Figure 3.19: 110 Pole figure of S-36AOw - Data showing cubic symmetry and fiber texture.

surement" by Keigo Nagao and Erina Kagami) this is very similar to (110) pole figure of PLT ((Pb,La)TiO_3) thin film deposited on silicon substrate measured with in-plane pole figure measurement method. This would agree with the experimental setup because the goniometer was set at 56.28 °2θ which is the position of (220)(004) plane of $SmNiO_3$ pattern and which is also pretty close to the literature value of 55.53 °2θ for the position of (220) plane of silicon crystal powder. This film had, however, some platinum buffer which was also visible on different pole figure measurement. The authors do however attribute the present intensity spots to the epitaxial films. The shift in position may be a result of smearing due to nonmonochromatic radiation, defocusing of the radiation spots and also due to an obvious shift in focusing plane with respect to silicon substrate surface.

Further enhancement of the pole figure intensity reveals some structure at low angles (3.21). Four discreet spots of intensity are found at about 27 degrees. Their intensity is over a hundred times smaller than the intensity of 111 set of planes of silicon. In the middle of the pole figure, a broad ring of intensity is detected. The maximum intensity is about 1 k counts, which is four times larger than the discreet spots but still about 23 times smaller than the maximum signal of the 111 silicon planes. The ring in a pole figure visualized along the normal direction is a sign of a wire(fiber)-type texture (chapter 2. in (89)).

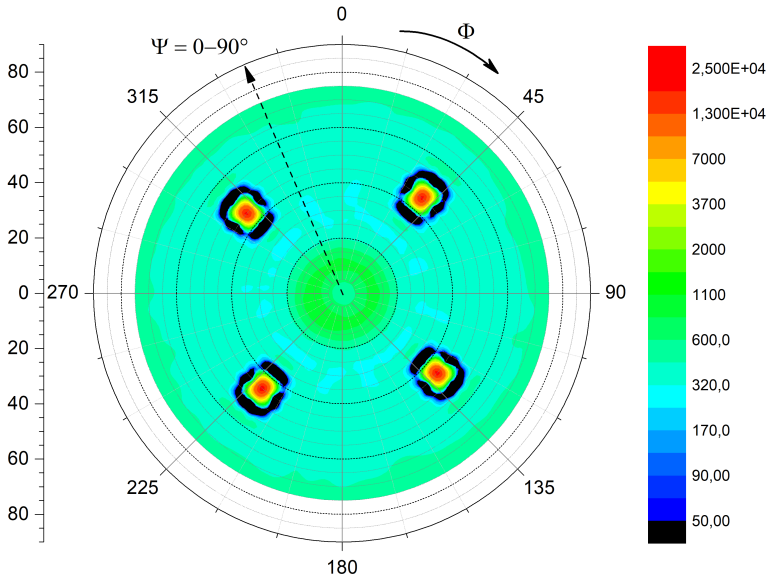

Figure 3.20: 220 Pole figure of S-36AOw - Data for the most intense spots attributed to the silicon substrate.

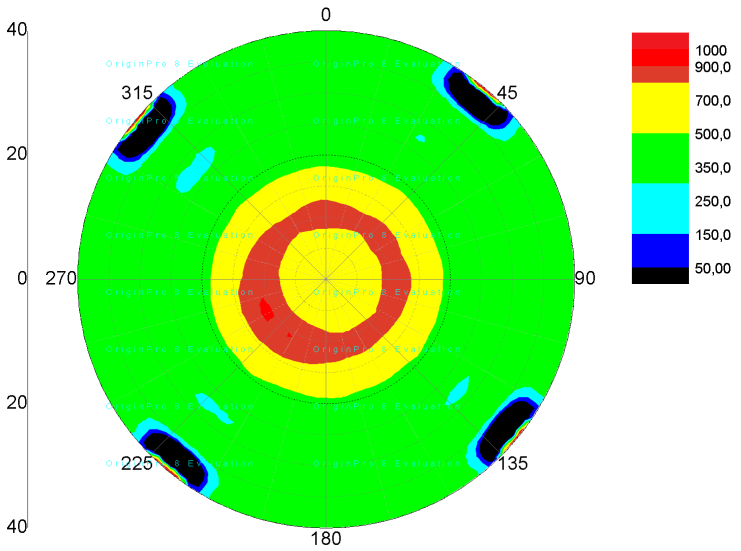

Figure 3.21: Pole figure of S-36AOw - Enhancement of the low angle region showing cubic symmetry.

For both preparation routes, the annealing procedure was held with the same parameters and the only difference was the composition and pressure of the plasma gas mixture. It is a known phenomenon for oxide thin films to have a crystallographic orientation dependent on the atmosphere of deposition, specifically the gas ratio between argon and oxygen. The change of orientation had been reported for nickel oxide films, whose orientation changes from (111) to (200) with the increase of oxygen content on the deposition chamber from o to 100% (16).

Another example is the ZnO films in which the increase of oxygen partial pressure-induced deterioration of the intensity of (002) Bragg peak and evolution of mixed texture (69). In work of Czternastek *et al.* the texture of ZnO films was investigated with respect to total pressure of the Ar+O_2 mixture (20). At low pressures no texture is observed and with the increase of pressure the ZnO crystals grow with c-axis perpendicular to the substrate surface (which was Corning glass). In SnO_2:Sb films the films are oriented preferably depending on the change of oxygen gas amount in the deposition chamber. Increase of oxygen is parallel to change of preferred orientation

It is also related to modification of the surface: the (101) oriented film is reduced while the (110) is oxidized and the ionization potential increases by over 1 eV (80).

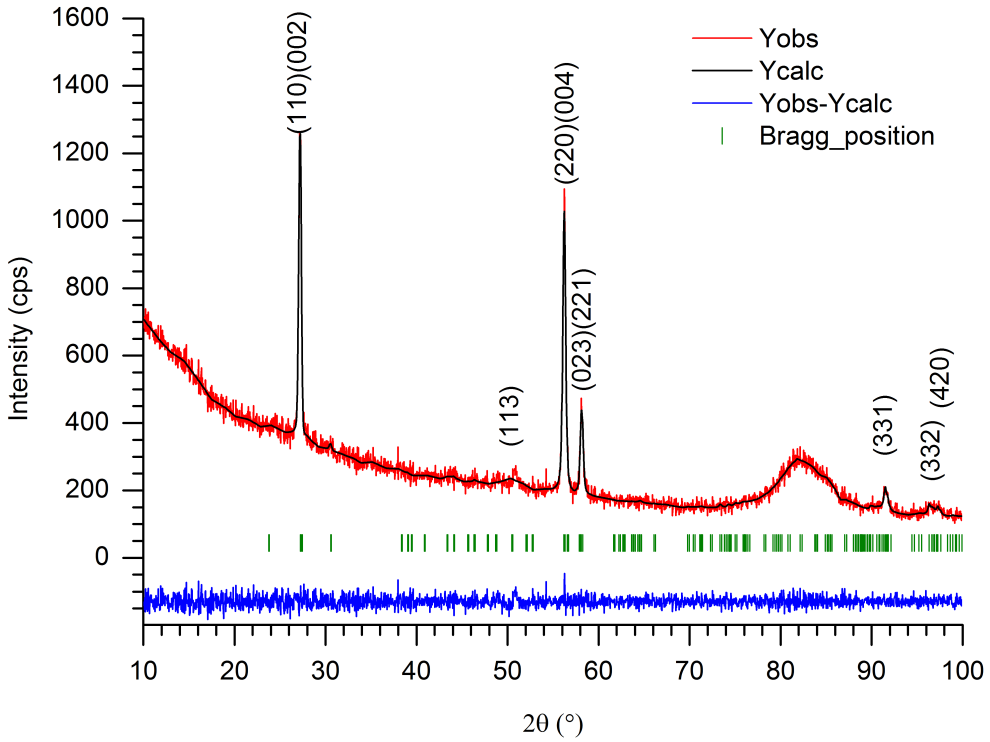

Figure 3.22: Rietveld refinement of S-36AOw diffraction pattern. - Strong texture of the actual $SmNiO_3$ phase led to amplify the intensity for only several Bragg peaks, The main (020)(112)(200) peak of the orthorhombic structure does not appear in the pattern.

The macroscopic investigation of $SmNiO_3$ film surface done by optical microscopy has revealed that the surface has a rich characteristic. Different kinds of species are a result of high-pressure annealing. This was described at the beginning of the chapter while describing the deposition process. The morphology of the films in micro and nanoscale was measured with atomic force microscopy. This technique was used to investigate both the topography and the electric behaviour of the film (using LC-AFM mode) during a temperature change in the measurement chamber. Therefore, in general, a conducting Pt coated silicon tip for contact mode was used. In some experiments, a non-contact tapping mode was applied which enabled to obtain a higher resolution of topographic images.

Before annealing, the films are quite smooth with small grains, as seen for S-30AOn sample in figure 3.23. The surface roughness is about a few nanometers. One can also notice large grains as well as ridges. The large objects observed under

the optical microscope were not identified here. There are some areas of higher contamination formed in tens of parallel paths of grains. The high temperature and pressure during annealing process change both the films crystal structure and morphology. The samples were annealed for 48 hours which is enough time to observe the grain grow. Together with grain growth also the roughness of the surface increases up to tens or hundreds of nanometers.

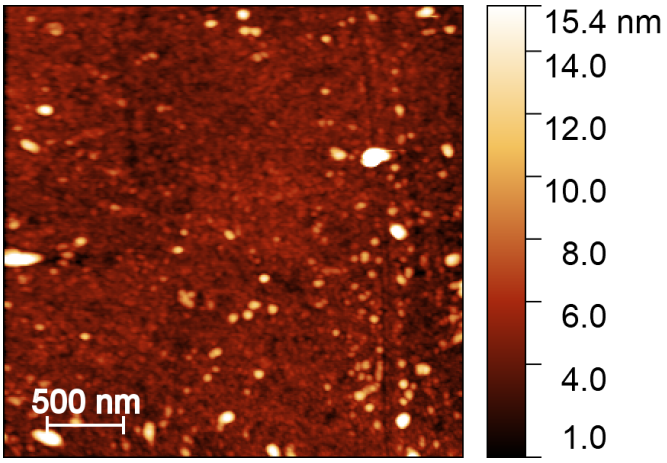

Figure 3.23: AFM image of surface topography of S-30AOn film, 3×3 μm^2 scan. - Surface of the film before annealing, the grains have about 40-50 nm in diameter, surface is smooth with low roughness. Image obtained in contact mode.

Images of the surface obtained in contact mode AFM show a grainy surface with grains diameter from 50 to 200 nanometers in sample S-36AOw (figures 3.25). However, in tapping mode, the resolution is higher and reveals that the objects perceived as grains in contact mode actually have their inner structure to it. For sample, S-36AOw images show that grains are in fact as small as 10-15 nanometers of diameter.

One can also notice the difference when comparing films obtained under various atmosphere.The films deposited in pure argon have higher surface roughness with many more irregularities and various features. After annealing of the Ar films, the grains appear significantly larger than for Ar+O_2 films. They may form column-like structures.

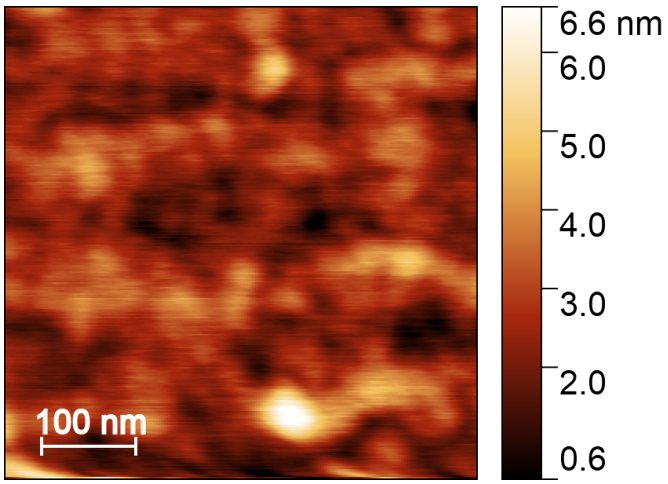

Figure 3.24: AFM image of surface topography of S-30AOn film, 500×500 nm^2 scan. - Surface of the film before annealing, the grains have about 40-50 nm in diameter, surface is smooth with low roughness. Image obtained in contact mode.

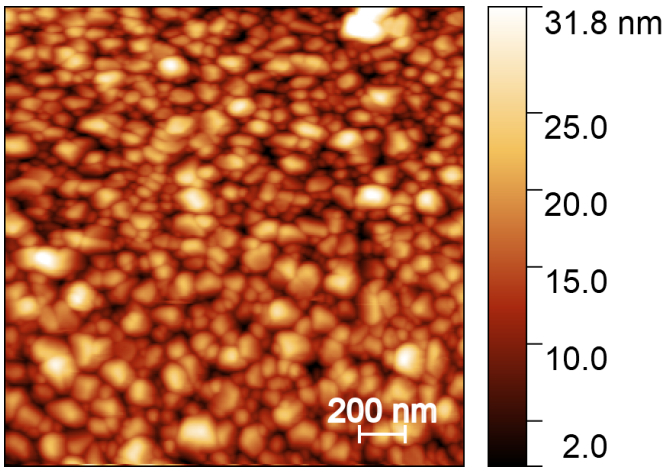

Figure 3.25: AFM image of surface topography of S-36AOw film. - Image obtained in contact mode.

4

Investigation of metal-insulator transition

In principle metal-insulator transition is related to a rapid change in electrical resistivity even by a few orders of magnitude. This sudden change is most often induced by temperature, but may also be triggered by electrical field or pressure. Most common way of investigating the presence of MIT is by measuring electrical resistivity as a function of temperature. The task is fairly easy for macroscopic bulk samples for which the electrical contact are of minor size with respect to the dimensions of a sample. Whereas for thin film materials the size of a contact starts to play a role. On top of that the volume of bulk material that is studied is in general more homogeneous than a thin film.

When performing traditional four-point method resistivity measurements on thin film materials the surface becomes a critical area for the measurement. In bulk material the surface can always be cleaned or polished so to present a pristine material. If not prepared in clean conditions, the electrodes deposited on thin film surface will always have a layer of foreign material between them and the sample surface. This may strongly influence the absolute values of measured resistivity.

The $SmNiO_3$ films deposited by magnetron sputtering exhibit the proper crystalline structure only after high-pressure oxygen annealing. Unfortunately this technological step results in formation of chromium oxide deposits on the surface as well as other elements such as aluminium, sodium and carbon. The impurities reduce the area of surface that is made of the given film material, and in turn the temperature behaviour of the material is investigated not only in the proper samarium nickelate perovskite phase but also in the impurity phases. All

methods of surface cleaning leave a significant mark or destroy the surface in a way that it would no longer be suitable for AFM measurements. The easiest method would be mechanical cleaning by rubbing away surface material with a tool that has higher hardness. However the tool's roughness would definitely increase the roughness of the film's surface which would cause serious difficulties in AFM measurements such as alteration of film surface morphology, creation of gaps and discontinuities/voids or possible tip breaking due to increased surface roughness. Higher quality of surface, sufficient for force microscopy imaging is obtained with ion beam polishing or ion beam etching. A beam of argon, neon or xenon ions in vacuum is directed onto a surface, when the energy of the ions is sufficient the surface deposits are etched with the impinging beam, uncovering the lower layers of sample. The AFM method is appropriate when studying the morphology and structural properties of the surface, or electrical/magnetic properties of metallic surfaces. For non-metallic surfaces a known phenomena is reduction of cation oxidation state by the ion beam. This may influence the variation of electrical properties and is not recommended when performing local conductivity measurements.

On the other hand, it is obvious that resistivity measurements require electrical contact between the used electrodes to ensure a good unobstructed charge flow. However a certain amount of impurities may block percolation of electrical current through the grains of investigated phase and inhibit possibility of long range charge transport. This is the case in investigated thin film materials. Performed four-point probe resistivity measurements did not yield much valuable information. The measurements were performed in the UHV conditions and the observed temperature dependence of resistivity was often irreproducible.

Similar challenges are present in atomic force microscopy in local conductivity mode, however they can be overcome by the specific character of the technique. Electrical contact between the scanning tip of the microscope and outer electrode should be insured to investigate metal-insulator transition properly. AFM tips have either cone-like or pyramidal shape, this allows for a tip to dive into the material. The tip can penetrate through the layer of adsorbates and probe the material below. This way the electrical contact is maintained not only with the sole surface but also with a few of the sub-surface layers of material, and is increased due to increased area of contact. This way there is a possibility that the interior of material is mostly of the proper structure and a long range paths of the material exist. The idea of the experiments was to investigate whether this is true and study the sample behaviour in such limited conditions.

4.1 Local conductivity of $SmNiO_3$ thin films

Local conductivity measurements were performed between room temperature 293-305 K and 453 K, which is well above the transition temperature for bulk $SmNiO_3$ compound ($T_{MI} \approx 400$ K). For each temperature several images of surface morphology as well as local current maps were collected. On top of that in specific areas I-V curves were collected in order to further investigate the electrical character of the area. In certain areas also I-V curve maps were collected, that is a map of regularly placed points in which I-V curves were measured and then saved together with the location on the surface for further processing.

The first decision to make when measuring local conductivity is the value of bias voltage that is applied between the sample and the scanning tip. If the bias is too small, the current does not flow through the sample or is below detection limit. In such case only a 'topographic' current map is obtained. The image is then only made of charges that are formed on the surface and strongly resembles the surface topography. The bias voltage cannot also be too large, so that the detector is not saturated and the response is possible to be measured. This is a difficult task for some of the materials, either strong insulators or for example topological insulators. The electrical behaviour will also change with temperature, which cannot always be taken into account especially for unknown materials.

In order to successfully visualize changes in conductivity at the surface region, for as-deposited sample S-30AOn, a bias voltage of 2.5 V was used. When using smaller voltages, the image was only mimicking surface morphology. Selected images of local current distribution on the surface of sample S-30AOn for various temperatures is depicted in figure 4.1. Although the surface is not very homogeneous in terms of electrical behaviour, it is evident that despite temperature increase there is no clear change of electrical behaviour. Randomly picked images show a very similar range of current values. No distinct features with temperature change are observed. The images also depict some artefacts such as gradual current increase or stripe-like current pattern that are discussed later.

The current measured after applying certain bias voltage was averaged over each whole image, and further those averaged values were averaged over several images taken at a certain temperature. The idea was to detect any changes of the conductivity as a function of temperature. The dependence was plotted in figure 4.2 a. Due to locality of the measurement the scatter of the current values is quite large. There is however a very minor trend visible - the value of the current increases slightly with temperature.

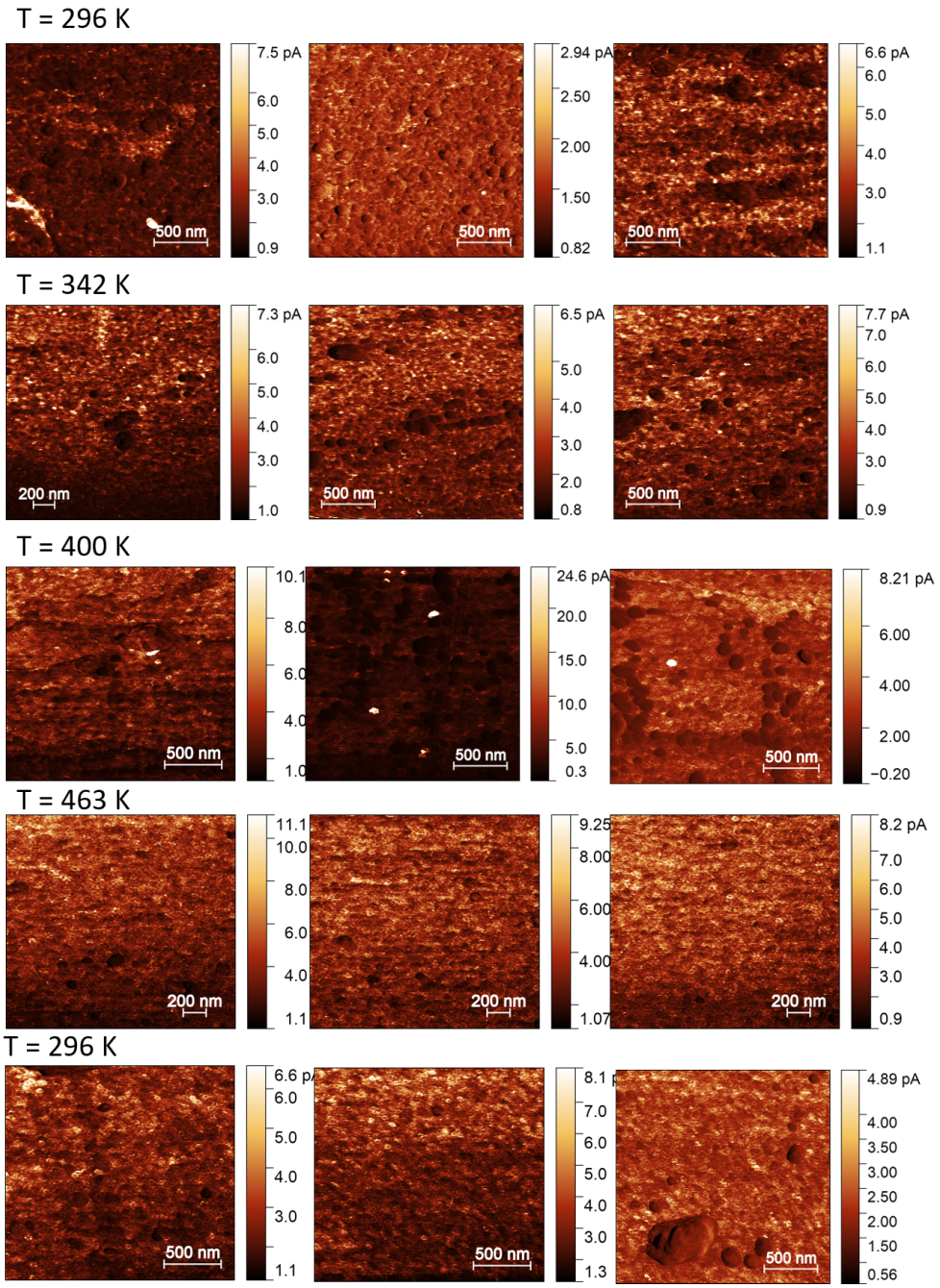

Figure 4.1: Selected local current maps in sample S-30AOn obtained in various temperatures. Scan size - 2×2 μm^2. - Some selected images of current distribution as a response to applied bias voltage of 2.5 V obtained for different areas of the sample surface. There is no clear increase in current value with temperature increase, investigation of average current versus temperature is necessary.

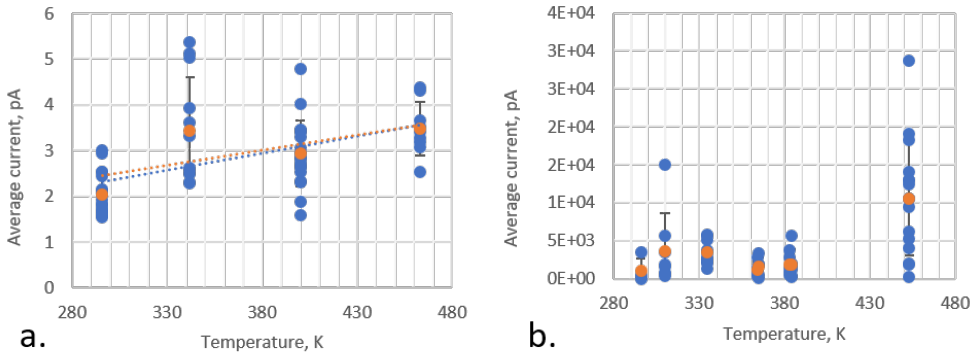

Figure 4.2: Average current as a function of temperature in sample before and after annealing - Data was taken for samples S-30AO deposited for 30 minutes in argon-oxygen atmosphere. Data collected for measured current maps show quite a large scatter, however a mildly increasing trend is evidenced. For every temperature the value of current was averaged and the points are marked in orange colour with standard deviation errors. a. Data for as-deposited film, bias voltage 2.5 V. Current is at the level of few pA. b. Data for the same sample but after annealing procedure, bias voltage 0.1 V. Current at the level of a few nA.

Sample S-30AOn after being annealed presents much better electrical properties - that is conductance of S-30AOw is a few orders of magnitude higher than before annealing (for sample S-30AOn). The result is even more surprising because bias voltage in measurements of as-deposited sample was 2.5 V, and after annealing bias voltage of 0.1 V was found to be sufficient and the most appropriate. Each of the image was scanned with the voltage and several maps of local current were collected for a certain temperature. For each current map the current value of each measurement point was averaged over whole image. The resulting average values of current were depicted versus temperature in figure 4.2 b. The first noticeable feature is a large scatter of data.

There are two main causes for that, which are as an example depicted in figure 4.3 for sample S-36AOw. For one thing, the surface of the sample, although in vacuum, carries various impurities which often build up on the surface of the scanning tip. Such impurity when present between the scanning tip and the surface impedes a proper flow of electrical current. The images of current distribution show that there often appear broad horizontal stripes of image where the current is lower or higher, without associated change in the surface morphology. Unfortunately it is quite difficult to remove such impurities, the most effective method

seems to be increased or prolonged friction while scanning. The second cause is related to the inherent properties of the sample. During scanning movement of the microscope, the bias voltage is applied continuously until the end of measurement. In many of the images of current distribution, a gradual increase of current together with the scan progression is observed. Such behaviour indicates that the applied voltage may change the state or resistivity of the material. In fact it has been possible to switch the resistivity of a chosen scanned area so that it shows a different response to applied bias voltage (figure 4.4). Not only the scanned area presents a change in current response but also the area surrounding the scan is affected.

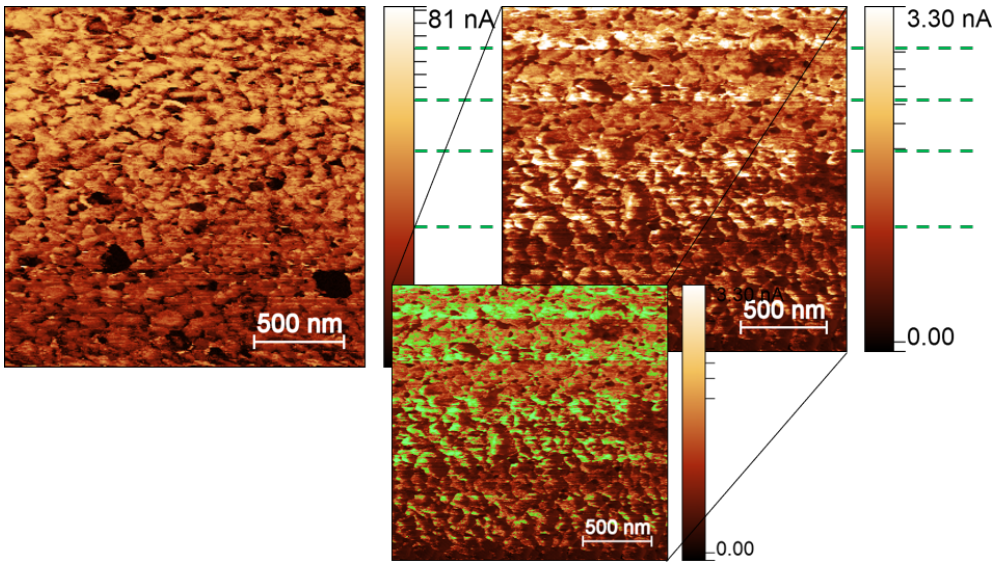

Figure 4.3: Phenomena during local current mapping in sample S-36AOw. - Gradual increase in detected current while scanning is connected to the inherent properties of material (left). At the same time a noticeable variation of values of current is detected in areas that form stripe-like pattern (right), this on the other hand related to possible surface contaminants that get stuck to the scanning tip. The borders of the stripes are noticed with green dashed lines. Images collected at different temperatures: left - 453 K, right - 305 K.

In order to get insight on the temperature character of resistivity of the sample surface, the averaged current was divided by the applied bias voltage. The results are depicted in figure 4.5. The line connecting points is a guide to the eye.

For the S-36AOw film, that is also one of the thickest ones, the bias voltage of 0.1 V was sufficient to image the changes in electrical conductivity. Due to the

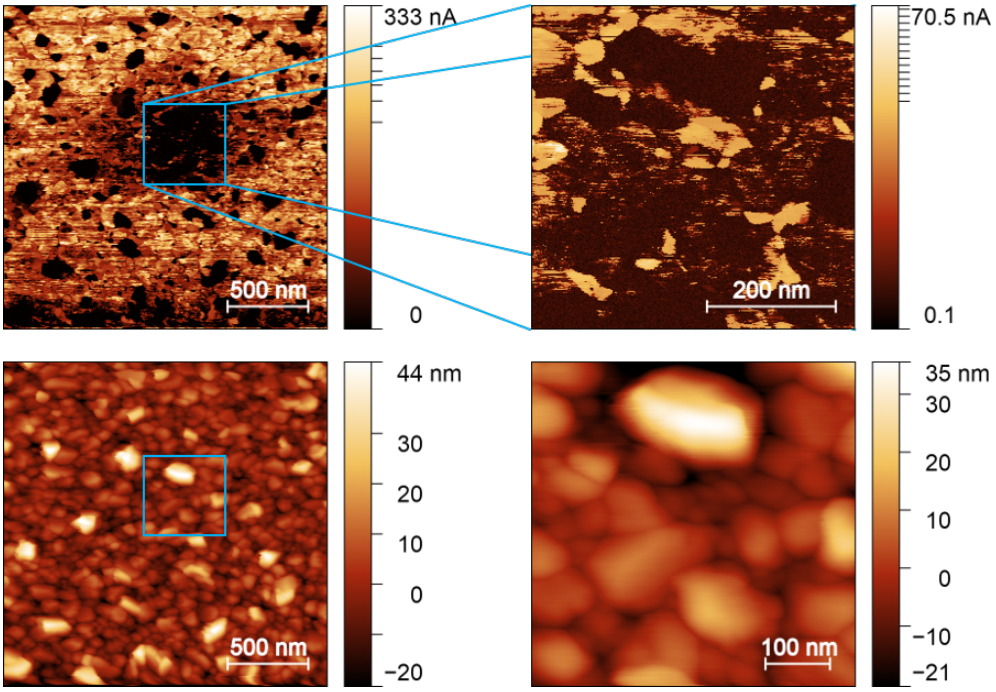

Figure 4.4: Resistive switching in S-30AOw at 453 K. - A small area scanned with 0.1 V applied bias voltage and further a larger 2×2 μm^2 area scanned with the same bias voltage. In the large area scan it is evidenced that the resistance of the incorporated part of the material is changed. The difference in mapped currents is not sharp, as the area surrounding the smaller scan area is also affected. It is related with the effect of the local electric field.

presence of the described measurement artefacts, among all scanned images the ones that had the least artefacts were chosen for further analysis. The relationship between temperature and the value of current averaged over scanned image shows a large scatter (figure 4.6). At lower temperatures the behaviour is somewhat erratic. Large differences in measured currents may stem from measurement artefacts or the varying spacial composition of the film. However it is very possible that the sample is undergoing temperature changes locally at various rates. Averaged values reveal that there is a slight increase of the current with temperature rise (decrease of resistance). One cannot forget about the surface contamination of mostly chromium oxides that has its important contribution to the measured current values. For example, sputter deposited chromium oxide coatings have the electrical conductivity several orders of magnitude lower than SNO thin films (65, 93). Therefore they will suppress the behaviour of SNO compound.

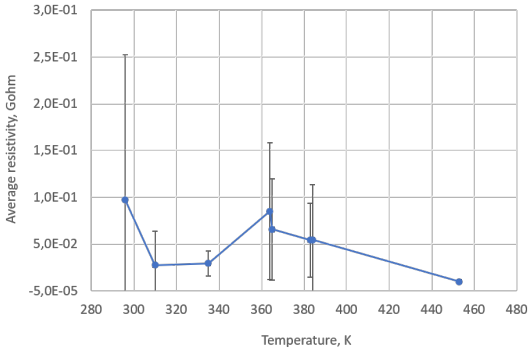

Figure 4.5: Average resistance versus temperature in sample S-30AOw. - Collected data for measured current maps shows quite a large scatter, however a slightly increasing trend is shown. The data was averaged for every temperature and depicted in orange. Over 330 K the current value seems to increase slightly but further decreases above 360 K.

Careful investigation of current maps shows that conductivity of some particular grains at the film's surface is much lower than that of the matrix. Separate analysis conducted for the matrix and individual grains reveal that indeed their behaviour is distinct. Images of a exemplary area and current map as well as the averaged electrical current and resistance as a function of temperature are shown in figure 4.7. In the presented images the well-conducting matrix is marked with a green mask, while poorly-conducting grains stay unmarked. Both areas show increase of value of electrical current and decrease of resistance value. However for the unmasked region the changes are more steady and less erratic. What is also noticeable is that in unmasked region, the current is smaller that in the masked region by an order of magnitude at higher temperature. These grains might be a different phase of chromium oxide that is even less conducting than Cr_2O_3.

For much thinner films such as S-12AOw, it was necessary to apply 2 V bias voltage in order to obtain reasonable current values. Data for that thin film shows the temperature dependence of electrical current does not follow a stable monotonic curve and is rather erratic. The relationship is plotted in figure 4.8.

This effect is possibly a result of averaging of electrical properties of areas marked as areas of higher and of lower current. Again, their temperature behaviour was determined separately. Comparison of current measured in both areas as a function oof temperature is depicted in figure 4.9. The results show that in well-conducting areas current shows a slight increase with temperature, while

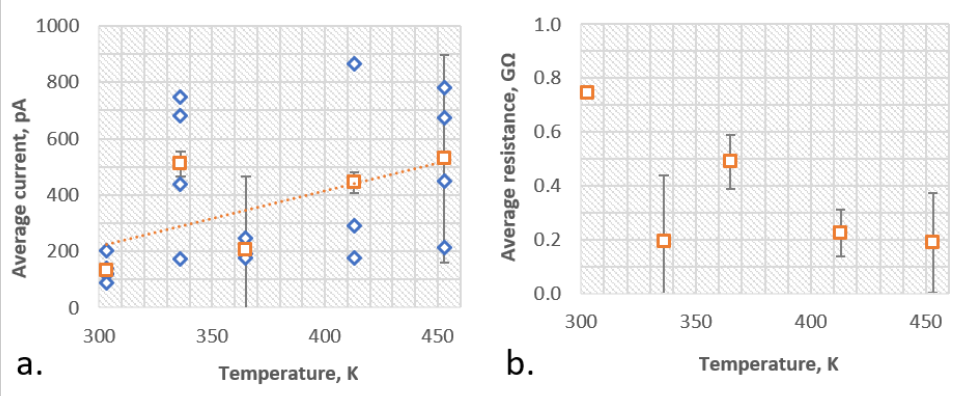

Figure 4.6: Average current and resistance as a function of temperature in sample S-36AOw. - a. Values of current averaged over scan area. The square orange points show a mean value of current for each temperature, together with standard deviation error. b. Mean averaged current converted to resistance with respect to Ohm's law. The bias voltage is 0.1 V.

in the poorly-conducting areas the current is rather stable. However the data scatter is very high. On top of that there appear to be two critical temperatures at which the electric current is erratic - at about 354 K and 413 K. This sample might be too thin, and the observed effects are in great deal masked by the effects of surface contamination. On top of that the sample exhibited resistive switching behaviour as well. The resistance was calculated to be of the order tens of GΩ.

At that point it is clear that surface contact methods do not give the possibility to properly investigate the properties of magnetron sputtered $SmNiO_3$ films. The main reason is surface contamination that was deposited on surface during necessary annealing procedure. It was presumed that for each annealed film, the material underlaying the surface layer of contamination is the proper $SmNiO_3$ phase that possesses the interesting properties such as metal-insulator transition.

That argument was verified during investigation of sample S-24AOw, where 'bare' areas of sub-surface layer of material appeared together with normal sample surface. Example of surface topography where those two regions are present are shown in figure 4.10. Images depict surface morphology and topography of surface area (marked in blue rectangle) as well as sub-surface area (marked in green rectangle). It was found that in sub-surface areas of sample the current was higher by about two orders of magnitude than in surface areas.

The temperature variation of local conductivity is best visualized in the I-V

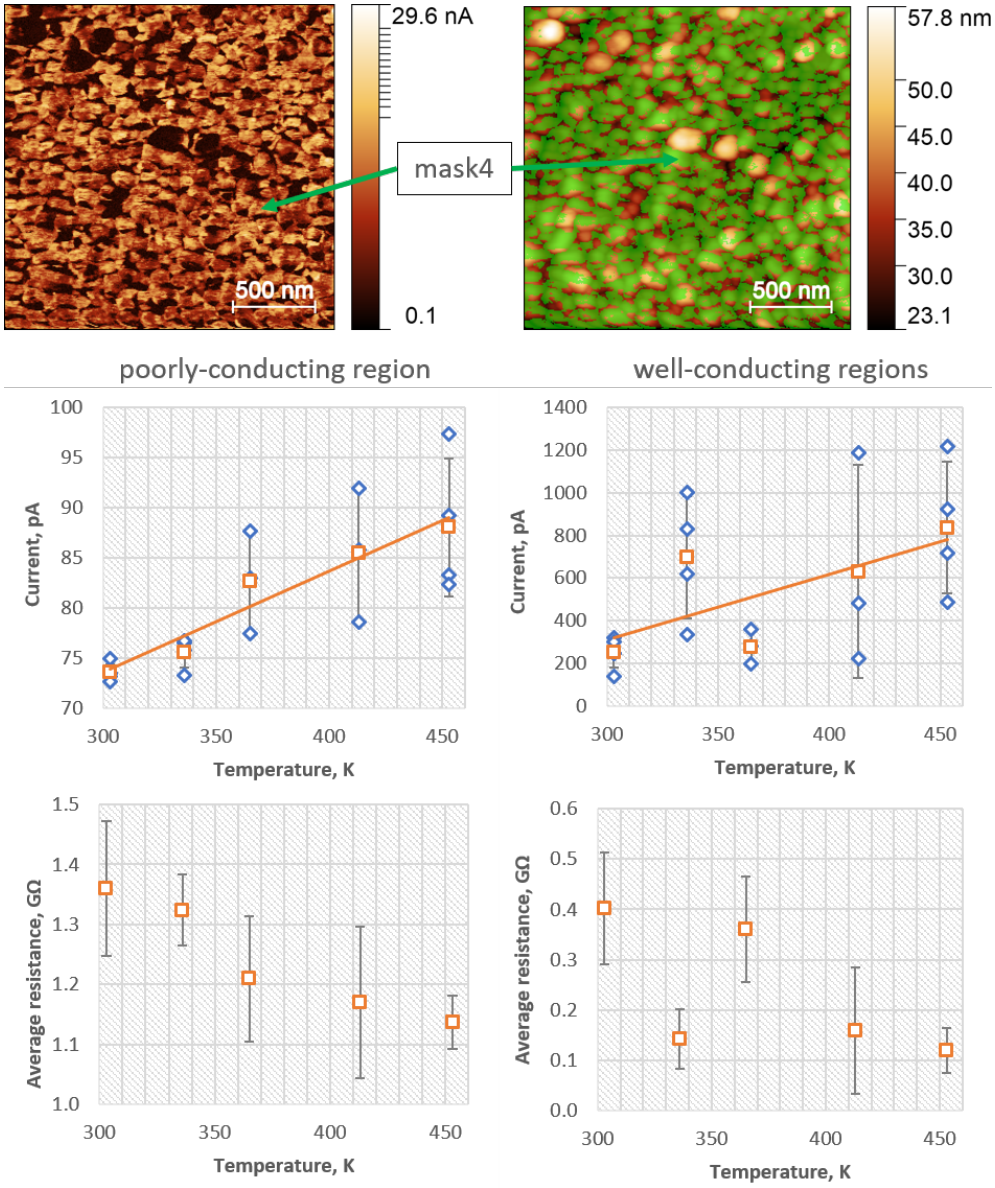

Figure 4.7: Local conductivity in certain regions of sample S-36AOw surface. - Local current map in the sample revealed a distinct behaviour of some of the surface regions. Some, predominantly large rounded grains (unmasked region), appear to have a significantly smaller conductivity that the majority of grains at the surface (region of the surface masked with green overlayer). Left - local current map, right - topography image with masked well-conducting region. The images were collected at 336 K. The comparison between the data shows that well-conducting region has a several times higher average current than the poorly-conducting region, and the difference increases with temperature. The bias voltage is 0.1 V.

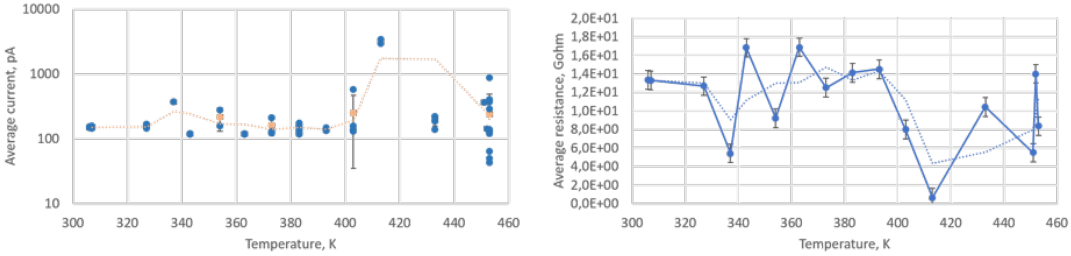

Figure 4.8: Average current and resistance versus temperature in sample S-12AOw. - Left: Presented data is selected so that images with least amount of artefacts and errors were taken for analysis. Right: Averaged current converted to resistance with respect to Ohm's law.

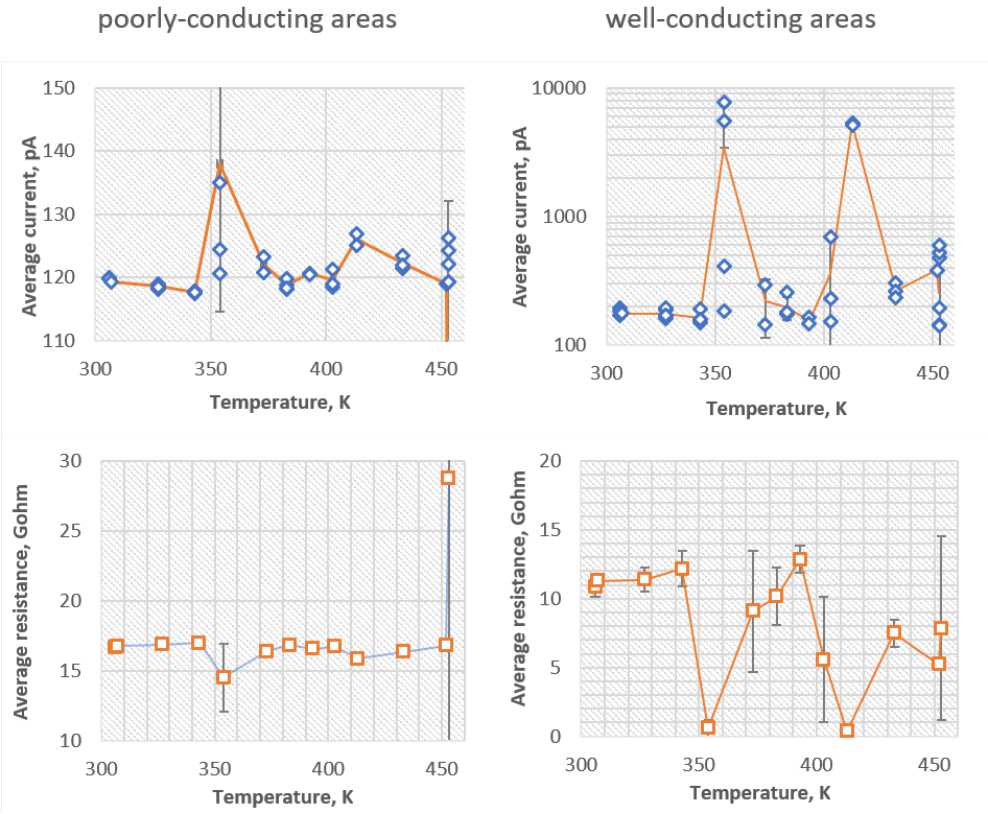

Figure 4.9: Local conductivity in certain regions of sample S-12AOw surface. - A comparison between regions of higher and lower conductivity.

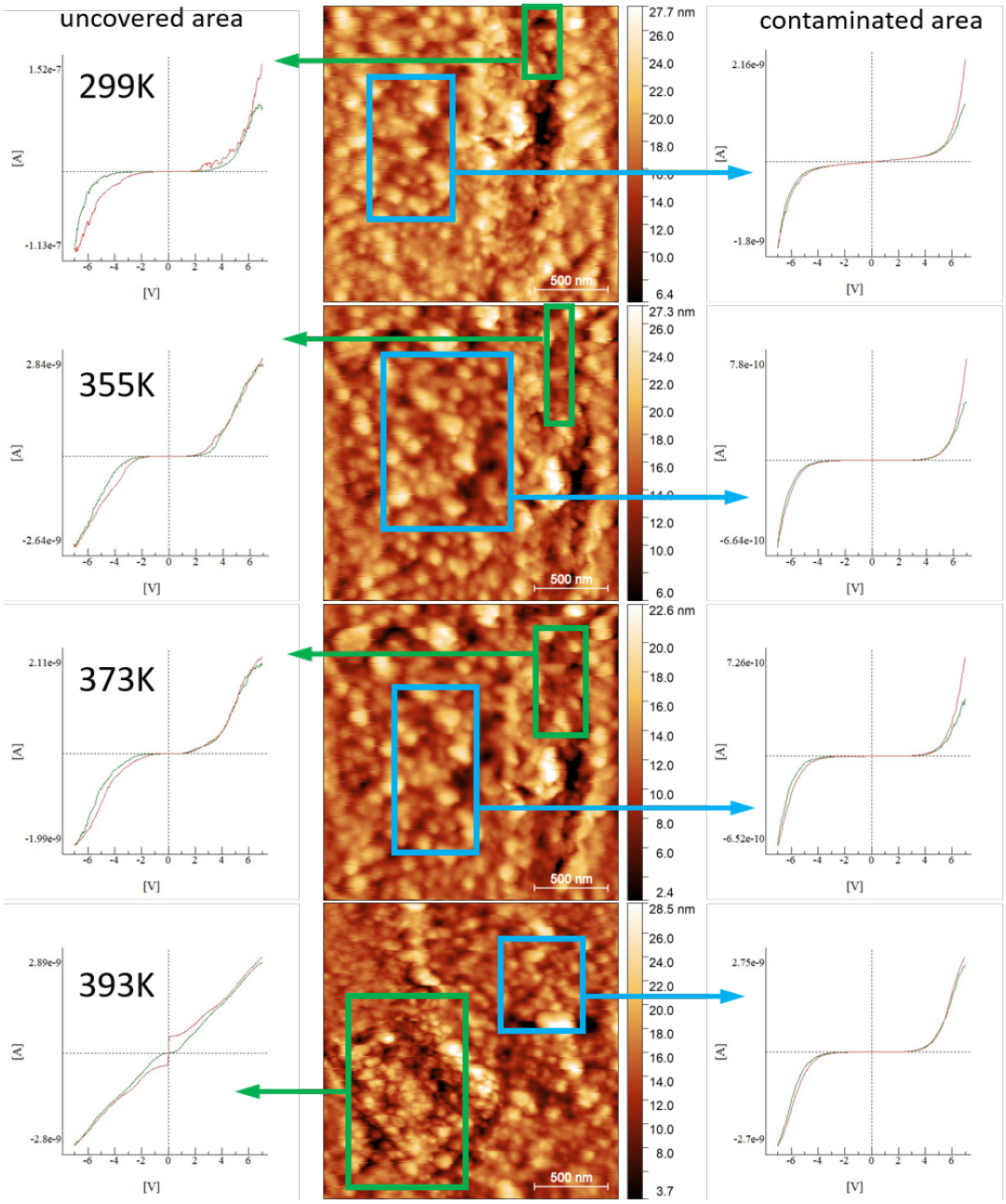

Figure 4.10: Temperature dependence of averaged I-V characteristics in sample S-24AOw. - I-V curves averaged over two areas uncovered (left) and covered (right) with contaminations arising from deposition process are shown. In the middle the topographic image over the scanned area is given with the areas of analysis denoted with rectangles. In the I-V curve, the green component is a forward scan measured with increasing voltage and red - backward scan measured with decreasing voltage.

characteristics which reveal the nature of the film underneath a layer of contamination. For both types of areas the curves indicate a semiconductor-like behaviour. However in the contaminated areas it is necessary to apply higher voltage before the same current response may be obtained - hence the resistivity of the area is higher. Whereas in the uncovered area the curves are narrower and the obtained current is a few orders of magnitude higher, apart only from the high temperature measurement. At 393 K the I-V curve is almost metallic, though averaged over a large area. The current is relatively low in comparison for values at lower temperatures, but this may be due to overlapping and averaging with the points with poor conductivity. It is also not negligible that the material undergoes constant resistive switching, which is shown in the individual I-V curves collected for certain measurement points (figure 4.11).

In the image, three types of I-V curves are shown - on the sides there are curves for either bare sub-surface area of contaminated surface area of measured sample S-24AOw. Curves in the middle present averaged I-V characteristics of certain scan area. All relationships are presented for four chosen temperature values - 299 K, 355 K, 373 K and 393 K. In the contaminated surface area the individual I-V characteristics show semiconducting behaviour with higher resistance than in the sub-surface area. In bare area the I-V characteristics of certain points appear to be different while scanning bias voltage in the forward and reverse direction. The reverse curves show a weaker response to applied bias voltage than forward curves - indicating switching of material to lower resistivity. While the temperature increases it is easier to switch a certain point, that is a lower voltage ('set' voltage) is needed for the switching. On the other hand, the low conducting, contaminated areas do not show any switching behaviour - the forward and backward I-V curves are pretty much their copy. In general, the whole scanned area also does not shot switching behaviour in I-V characteristics. Of course most of the surface in the investigated sample was contaminated and only small areas were presenting the low-resistivity phase.

In view of results from other experimental techniques characterizing the film it is likely that the uncovered area presented the proper $SmNiO_3$ perovskite phase.

Conclusions from LC-AFM measurements

Investigation of metal-insulator transition in $SmNiO_3$ thin films deposited by magnetron sputtering was not a straightforward task when using Local Conductivity mode in AFM microscopy. This is largely due to the structure of the sample and surface contaminations that arose during a necessary technological operation of high temperature and pressure oxygen annealing. The LC-AFM technique is a

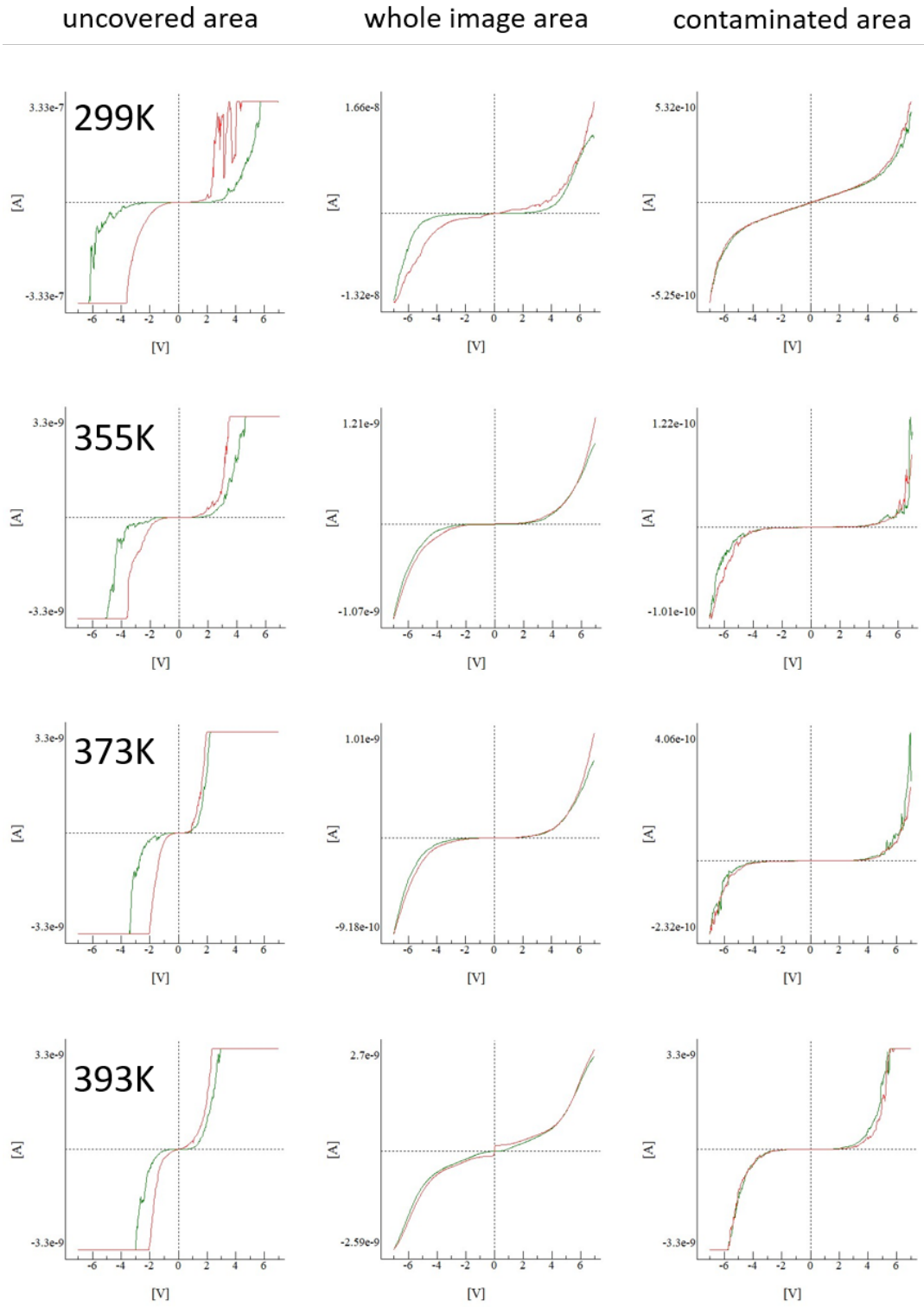

Figure 4.11: Temperature dependence of I-V characteristics of individual points in sample S-24AOw. - I-V curves of individual points in uncovered (left) and covered (right) areas. In the middle the I-V curve averaged over whole scanned area is given.

contact measurement method and therefore is highly sensitive to the surface composition of the sample. Most of the obtained results were masked by the electrical behaviour of the top layer made of oxides including chromium oxides. Therefore the temperature dependence of current averaged over several imaged regions did not yield a convincing evidence that the metal-insulator transition truly occurs in investigated samples. The increase of current level with respect to temperature was proven. That dependences converted, based on Ohm's law, into resistance-temperature diagrams, were too erratic. The inherent phenomena related to resistive switching behaviour but also artefacts related to surface contaminations also influence the electrical behaviour of studied material and obscured the behaviour related to metal-insulator transition of $SmNiO_3$ compound.

However even in this situation, the difference in behaviour of samples treated with annealing and untreated, were distinct. The untreated surface almost does not react to change of temperature, the level of current is several orders of magnitude lower than for treated samples even despite higher bias voltage applied. The level of current was also noticed to be lower by at least an order of magnitude when comparing the very top surface layer of material with the layers of material that are below that. It was very well evidenced in few regions that were discovered to be bare, exposed surface of most likely the actual $SmNiO_3$ crystalline phase. Those regions were deeply investigated, successfully enough to discover temperature differences of the electrical behaviour of covered and bare sample surface. As evidenced by the averaged I-V characteristic curves in sample S-12AOw, the electrical behaviour of bare surface changes from semiconducting at 299 K to almost metallic at 393 K. At the same time the covered areas stay semiconducting, with the current level an order of magnitude smaller.

The same obstacles hindered proper investigation of macroscopic electrical conductivity by four point probe method. This led to application of Raman spectroscopy to investigate the macroscopic effects of metal-insulator transition. Because the technique utilizes infrared laser radiation, it is able to penetrate the top layer of contaminations and probe the properties related to the actual $SmNiO_3$ phase.

4.2 Raman scattering processes

Temperature behaviour of Raman spectra of SNO thin films was investigated in order to obtain information of the occurence of metal-insulator transition and

the transition temperature. It was demonstrated that various modes in Raman spectra are sensitive to temperature change due to structural changes but may show a rather complicated behaviour in rare earth nickelate oxides (34, 100).

Rare-earth nickelates with medium-sized rare-earth ion, such as $SmNiO_3$ were found to have a very slight changes in structure, as measured by XRD. The observed change in symmetry from orthorhombic to monoclinic is so small that the lower symmetry structure still are equally well described by orthorhombic unit symmetry. On the other hand, Raman spectroscopy is more sensitive to structural changes and is able to detect even small distortions. Following the experiments described in the cited article, Raman spectra were collected within a range of temperatures that should cover the MI transition temperature and above. However, the regime below room temperature was not covered due to lack of necessary experimental set-up.

The polycrystalline thick film S-42Aw has its Raman spectra (figure 4.12) slightly resembling the literature ones obtained for SNO thin films deposited on LAO (34). Main difference is that the width of the bands is larger for the films studied in this work. Also the intensities of the bands other than the main at about 450 cm^{-1} are different than those presented in mentioned literature. It is advantageous that Raman spectrum of silicon substrate does not interfere with the spectrum of the film. Depending on the direction of polarization of laser relative to fiducial mark the position of bands appear slightly shifted. The first band of silicon metal is present at 520.8 cm^{-1}, and the second massif appears between 920 and 1020 cm^{-1} as found in RRUFF online database (http://rruff.info/Silicon).

The Raman mode at about 450 cm^{-1} shows a complicated behaviour with temperature change. Initial shift of position towards higher wave numbers at temperatures up to 308 K is soon followed by a rapid change of the position down to lower wave numbers. At 343 K there occurs an inflection point after which the mode softening becomes even more rapid. At about 408 K the position of the mode reaches a minimum wave number of about 447 cm^{-1}. The minimum is quite sharp. Above the critical temperature there is a similar rapid change of band position towards higher wave numbers. The overall shape of Raman spectra for another thicker film S-36AOw is very similar (figure 4.13). The change of Raman shift for both of the samples is at the same level. The chosen Raman mode presents very similar pattern of temperature change - rapid decrease below critical temperature and rapid increase above. However, the critical temperature estimated from the measurements is about 10 degrees Kelvin higher for sample S-36AOw than for S-42Aw.

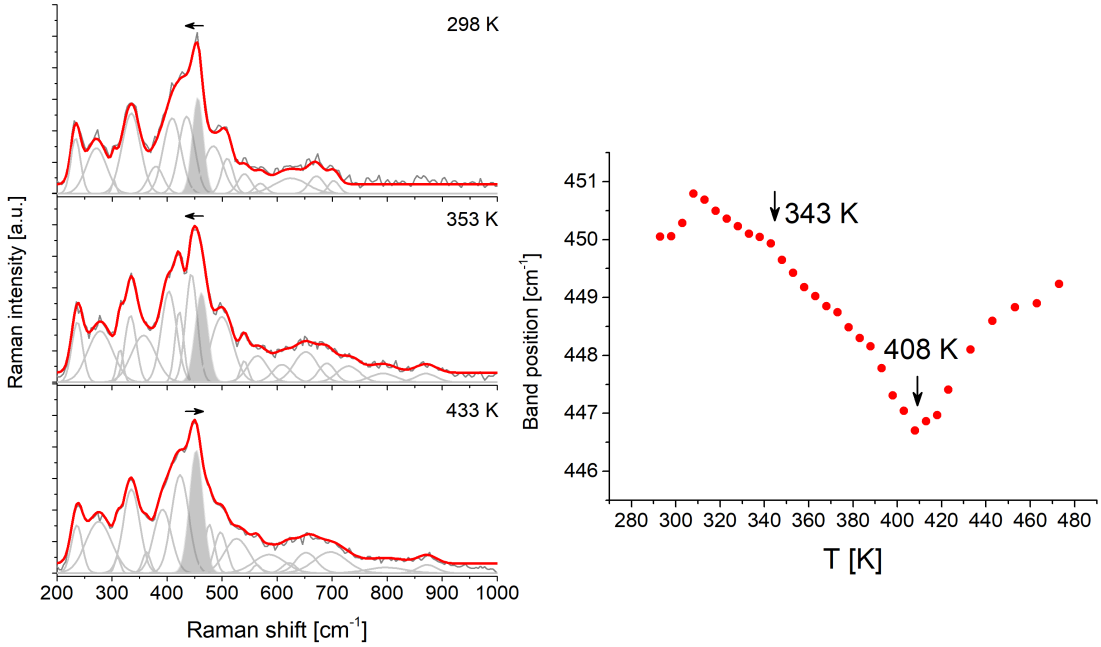

Figure 4.12: Temperature dependence of chosen Raman mode in sample S-42Aw - Band position of most intense mode in the spectra versus temperature is depicted. Initial minor increase in position soon changes into rapid softening of the mode down to a critical point at about 408 K. With further increase of temperature the position of the mode moves back in the direction of higher wavenumbers. On the left, Raman spectra at specific temperatures are shown together with the fittings. Arrows above the analysed band indicate the direction of changes of its position above the inherent temperature.

In much thinner S-12AOw film the Raman modes displayed a high half-width and strongly overlapped each other. Whereas for thicker films such as S-42Aw or S-36AOw the spectra show a better resolution with distinct Raman modes. Temperature variation of the Raman spectra in S-12AOw sample show that there is a slight softening of various modes (see figures 4.14 and 4.15). For example a mode around 400 cm^{-1} and actually the whole massif 400 - 450 cm^{-1} does experience slight shift towards lower wave numbers and also their intensity relative to the massif 200 - 350 cm^{-1} does decrease with temperature increase. The latter massif presents a bit different behaviour. While mode at about 330 cm^{-1} softens with temperature increase, the mode at about 230 cm^{-1} shifts towards higher wave numbers. The mode at 270 cm^{-1} is observed to strongly lower its intensity at about 413 - 423 K. Also the overall spectral .weight proportions between the

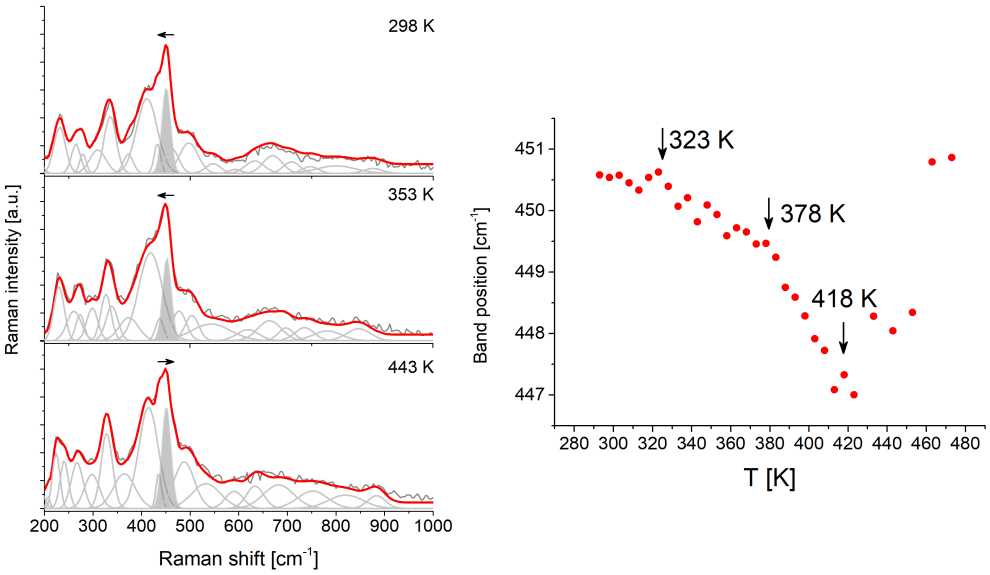

Figure 4.13: Temperature dependence of chosen Raman mode in sample S-36AOw - Band position of most intense mode in the spectra versus temperature is depicted. Initial minor increase in position soon changes into rapid softening of the mode down to a critical point at about 418 K. With further increase of temperature the position of the mode rapidly moves back in the direction of higher wavenumbers. On the left, Raman spectra at specific temperatures are given together with the fittings. Arrows above the analysed band indicate the direction of changes of its position above the inherent temperature.

two massiffs change with temperature increase. The massif 370 - 480 cm^{-1} is losing spectral weight in favour of 200 - 370 cm^{-1} massif. The latter one is also becoming narrower.

As expected, Raman spectra of sample before annealing present quite a different set of bands. Temperature dependent Raman spectra of sample S-30AOn have the Raman active modes in areas partially overlapping strong signal from silicon substrate, which is evidenced here despite the rather high thickness of the film (figure 4.16). The bands are significantly wider than for any annealed sample which indicates that the atomic structure is partially amorphous. The spectra of film are of lower intensity, whereas the prominent bands of silicon substrate appear between 480-560 cm^{-1} (Si 1^{st}) and 900-1000 cm^{-1} (Si 2^{nd}). The amorphous structure of the Sm-Ni-O film does not allow for many vibrations to appear collectively. No critical temperature was found for the set of obtained spectra.

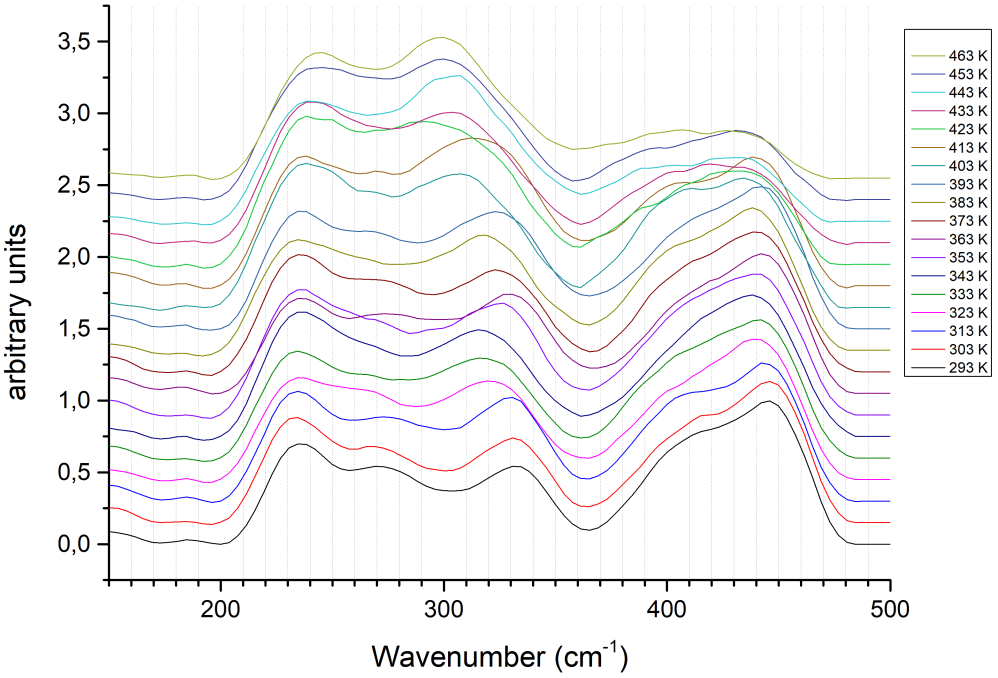

Figure 4.14: Temperature dependence of Raman modes in sample S-12AOw - A selected part of measured Raman spectrum is shown. The spectra contain two main massifs in which most of the individual modes undergo shifts with temperature and a few disappear. The increase of temperature is accompanied with a relative spectral weight transfer from the massif 370 - 480 cm^{-1} to the massif 200 - 370 cm^{-1}.

Raman spectroscopy is by definition strongly related to structural properties of a material, therefore a comparative analysis with the crystallographic structure data should be made. The table 4.1 includes necessary information. One can observe that the critical temperature of minimum value of Raman mode shift behaves according to pseudocubic lattice parameter or lattice mismatch. The higher the mismatch (lower pseudocubic lattice parameter), the higher the critical Raman temperature. The magnitude of Raman mode position change, that is difference between minimal value of Raman mode position and position at room temperature is inversely related to film thickness - the thinner the film the highest the Raman shift difference. For the thickest films, both obtained at different atmospheric plasma conditions - S-36AOw and S-42Aw, the Raman shift difference

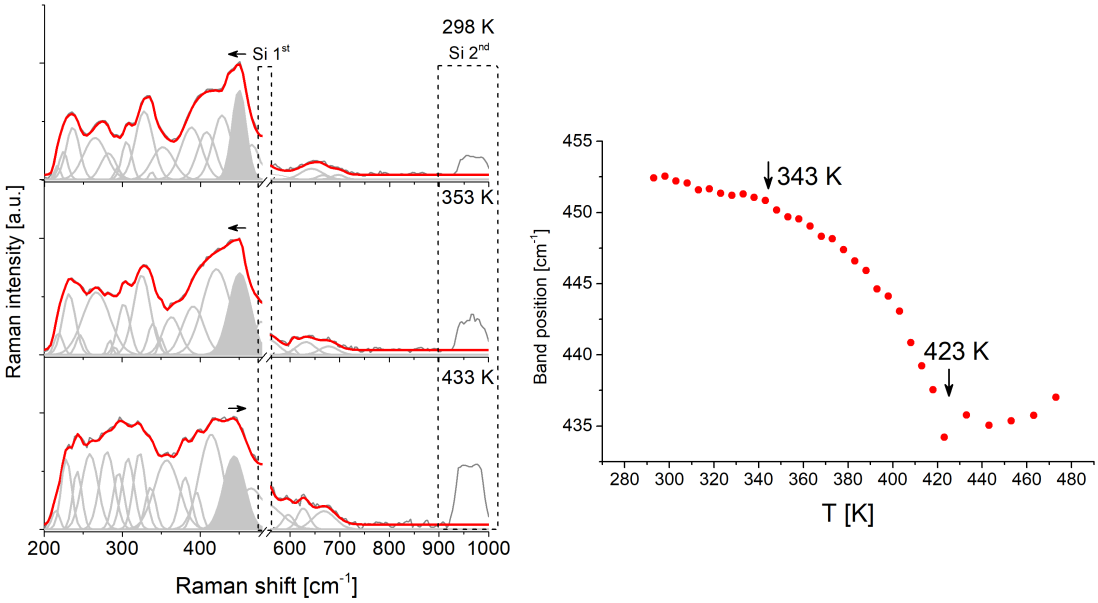

Figure 4.15: Temperature dependence of chosen Raman mode in sample S-12AOw - Band position of most intense mode in the spectra versus temperature is depicted. Initial minor increase in position soon changes into rapid softening of the mode down to a critical point at about 423 K. With further increase of temperature the position of the mode slowly moves back in the direction of higher wavenumbers. On the left, Raman spectra at specific temperatures are given together with the fittings. Arrows above the analysed band indicate the direction of changes of its position above the inherent temperature.

is the smallest and increases with thickness decrease.

4.3 Nickel electronic structure across the MIT

Photoelectron spectroscopy is a powerful technique which is used for both chemical analysis and electronic structure investigation. As it was shown for the $EuNiO_3$ films the careful analysis of core levels can be used for determination of the critical phenomena responsible for MI transition (12). The analysis of the valence band changes for nickel based films were also interesting.

However the extreme surface sensitivity of this technique causes severe difficulties the measure samples whose surface is affected by the manufacturing technology. Such is the case of SNO films. Despite the apparent surface contamination

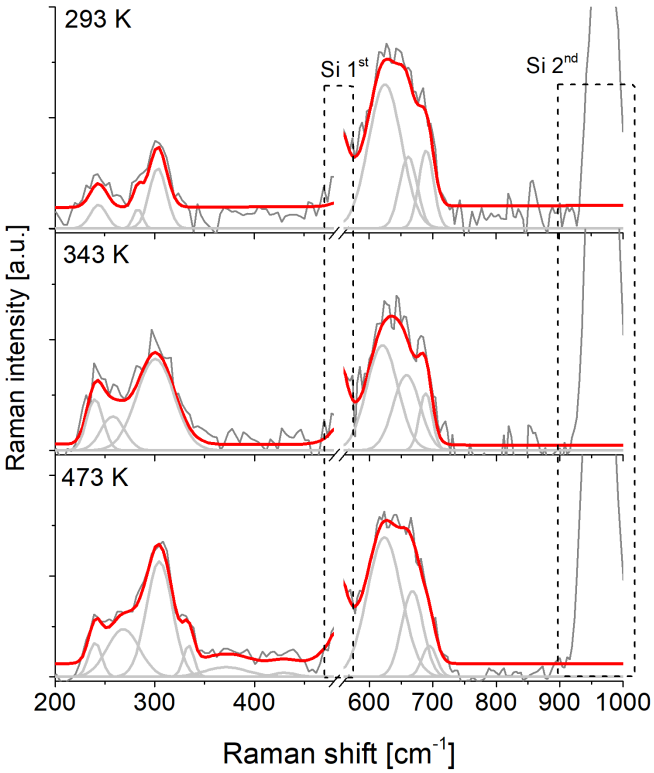

Figure 4.16: Temperature dependence of Raman spectra in sample S-30AOn - Raman spectra at chosen temperatures do not show any bands of the main massif between 400 and 500 cm^{-1}, and their shape is an indication of amorphous character of the sample. Raman spectra at specific temperatures are given together with the fittings. For clarity, the high intensity first and second silicon bands have been cut out.

of investigated films, in XPS the irradiating X-ray beam penetrates the sample deeper than only the strict surface and the escape depth of analyzed photoelectrons is at least few nanometers. Also gentle surface mechanical modification allowed to measure and to obtain interesting temperature dependent results.

The elemental composition of SNO films as well as the type of contaminations and their chemical states is described in previous chapter. This section is entirely focused on the chemical state of elements building $SmNiO_3$ films, primarily nickel, and their temperature dependence.

According to various theories on metal-insulator transition in compounds such as samarium nickelate, the nickel ion plays a crucial role in the phenomena. A possible disproportionation between charge on the nickel site in the temperature

Table 4.1: Comparison of thin film strain imposed by the substrate and critical temperatures in temperature dependence of chosen Raman mode position.

sample	thickness, nm	$\overline{a_p}$	lattice mismatch, %	T_2, K	Raman shift difference, cm^{-1}
S-4AOw	26	3.786	1.40% (tensile)		
S-12AOw	99	3.790	1.30% (tensile)	423	18.2
S-24AOw	169	3.793	1.21% (tensile)		
S-30AOw	193	3.792	1.25% (tensile)	413-418	8.6
S-36AOw	216	3.789	1.32% (tensile)	418	3.5
S-5Aw	80	3.800	1.03% (tensile)		
S-42Aw	520	3.794	1.19% (tensile)	408	3.4

regime below the transition which causes the electronic orbital separate. With an external trigger, such as temperature, the disproportionation decreases and at the same time the orbital overlap increases which leads to closing of energy gap between nickel and oxygen orbitals and increase in electronic conductivity in the material. The disproportionate distribution of electronic charges on the nickel sites creates at least two sites bearing charge described as $3-\delta$ and $3+\delta$. Such charge distribution would influence the electronic structure of material, especially nickel electronic structure. If large enough, it should be observable in X-ray induced photoelectron spectra as two or more components to the main nickel multiplet line whose position and intensity vary with temperature.

The energy gap in SNO compounds is considered to be a charge-transfer gap, it involves an electronic transfer between nickel and oxygen sites. Therefore oxygen electronic structure should also be taken into account. However due to inevitable surface contaminations the spectra are affected by the oxygen bearing surface contaminations and a detailed analysis is much more difficult. What is more, because in theory samarium does not take part in the metal-insulator transition, its electronic spectra should not vary with temperature. The spectra are also analyzed.

The S-36AOw sample was measured between 123 K and 683 K at selected temperatures. The fitted XPS nickel spectra for 123 K, 303 K and 683 K are presented in figure 4.17. During the experiment the sample was measured again at room temperature. Low-temperature spectrum is characterized by high background and

T, K	1	2	3	7	8	9	1/2	7/8	2-1	8-7
308	853.66	855.6	858	871	873	877	0.24	0.09	1.94	2.0
123	855.16	856.5	858	872	873.4	876	0.34	0.34	1.34	1.4
303	854.29	855.6	858	872	873.1	877	0.21	0.17	1.31	1.1
393	854.36	855.6	858	872	873.2	877	0.25	0.19	1.24	1.2
683	854.23	855.5	858	872	873.1	876	0.18	0.23	1.27	1.1

Table 4.2: The details of fitting of nickel spectra of S-36AOw sample for various temperatures. The position of fitted peak maximum, area ratio between constituent lines and energy displacement for each temperature are calculated.

higher noise, as opposed to high temperature measurements. Although slight, the change in the shape and ratio of constituent peaks in main $2p_{3/2}$ as well as $2p_{1/2}$ multiplet lines is evidenced. At low temperatures the $2p_{3/2}$ line visibly consists of at least two peaks. That separation becomes less prominent as temperature of the sample increases. Detailed data is presented in table 4.2.

Although the line position may not be best described due to errors while applying shift setup, the line separation is a meaningful parameter that can be used for comparison of data for various temperatures. As far as the area ratio of lines ascribed to $Ni^{3+\delta}$ and $Ni^{3-\delta}$ nickel states it is a bit more difficult to be used for comparison, mostly because the lines are probably composed of other individual lines. Whereas line position displacement, calculated as a difference between positions of maximum amplitude of both mentioned lines, is less sensitive to a true internal structure of the peak. A general conclusion can be drawn from presented results, that the higher the temperature, the smaller becomes the displacement between constituent peaks of Ni $2p_{3/2}$ line.

It is also noticeable that for the first measurement at room temperature the nickel spectrum is slightly different. This may be due to possible surface damage during mechanical processing. The damage involving broken nickel bonds may disappear at higher temperatures when the structure of the spectrum changes and a measurement repeated at room temperature does not yield quite the same spectrum. Another explanation would be that there is a hysteresis of nickel state in SNO lattice.

The much thinner S-12AOw sample, of estimated 100 nm in thickness, was a bit more difficult to measure. Effects of charge build-up were stronger and the signal-to-noise ratio was much lower. Especially at low temperature, despite

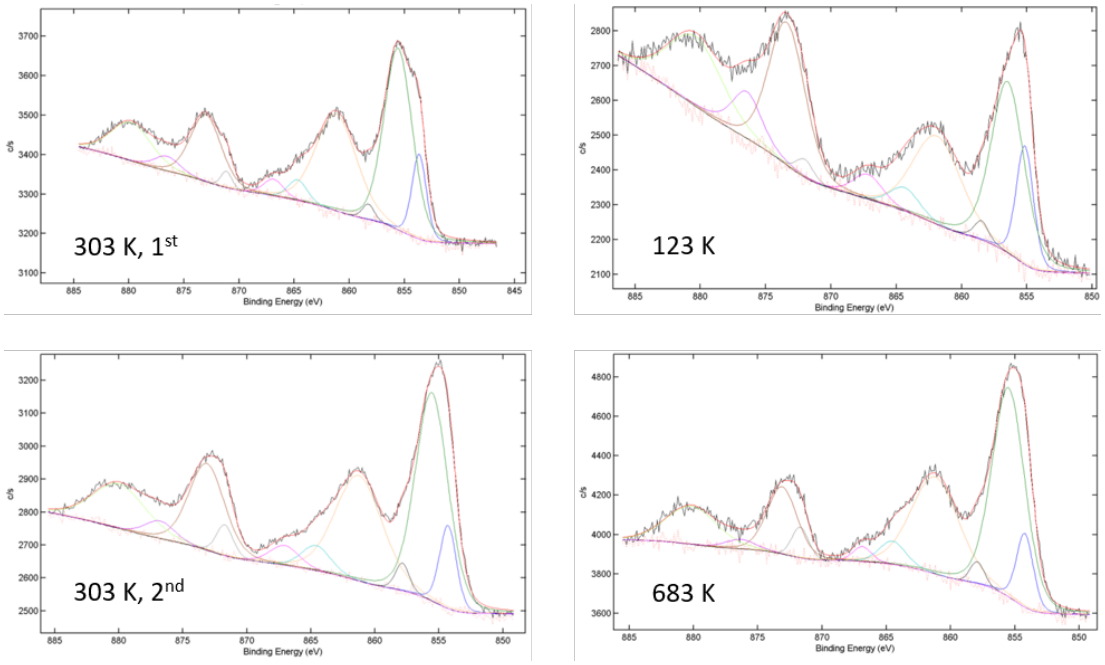

Figure 4.17: Nickel 2p multiplet spectra at different temperatures for sample S-36AOw - a. The low temperature spectrum of nickel presents a noticeable broadening and a kink for higher binding energies in the Ni $2p_{3/2}$ envelope. Two constituent peaks are separated by about 1.34 eV. b. In comparison to lower temperature spectrum the separation of the constituent peaks of Ni $2p_{3/2}$ line has decreased slightly, together with the area ratio between the low and high energy constituent peak. d. The spectrum aquired well above the literature value of MI transition still presents a complicated envelope. However the peak separation as well as area ratio is smaller than at lower temperatures.

even the long measurement duration a poor quality spectrum was collected in comparison to spectra at higher temperatures (figure 4.18). Details of spectra fitting are found in table 4.3.

The temperature behaviour is in principle very similar to what was observed for sample S-36AOw. Peaks forming the envelope of nickel Ni 2p spectrum undergo changes in binding energy position and the peak area. As the temperature rises the constituent peaks forming $2p_{3/2}$ line shift towards each other so that the energy displacement between them decreases. At the same time a transfer of spectral weight from low to high energy constituent peak is observed. What distinguishes this film from the thicker one is that the observed changes are more drastic. Both

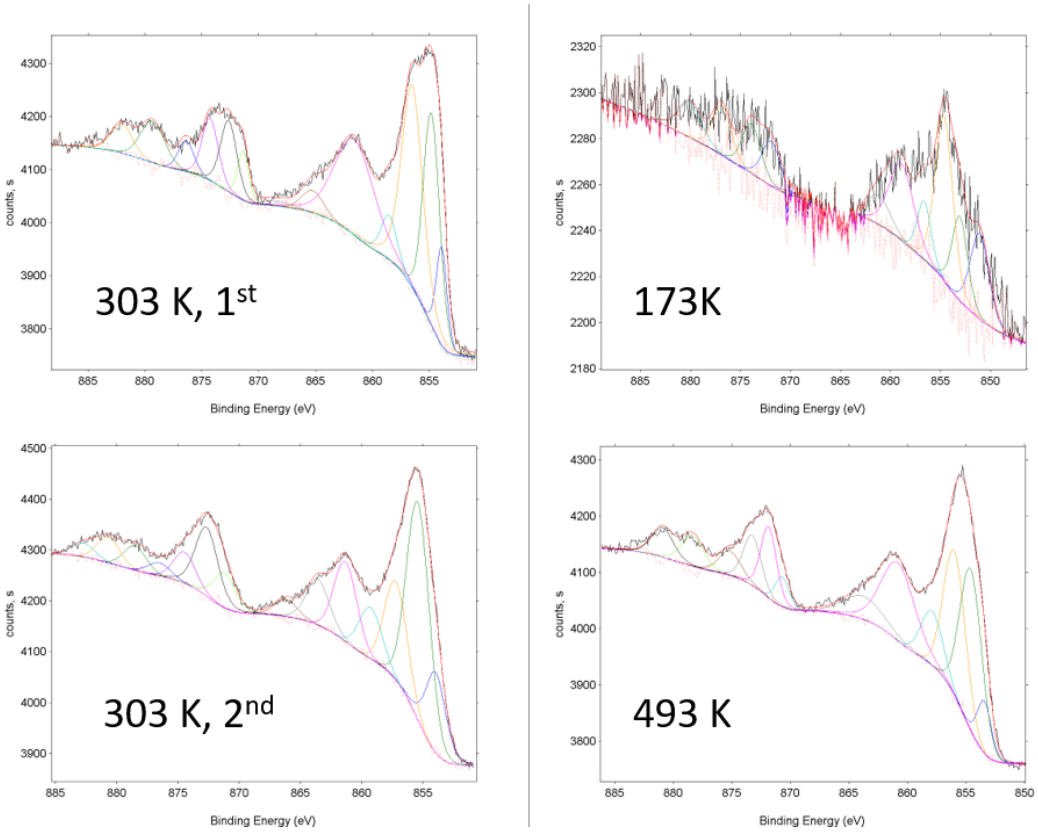

Figure 4.18: Temperature dependent nickel 2p multiplet spectra with fitting for sample S-12AOw - Although the initial room temperature separation of constituent photoelectron lines, it disappears with further temperature treatment

Table 4.3: The details of fitting of nickel spectra of S-12AOw sample for various temperatures. The position of fitted peak maximum, area ratio between constituent lines and energy displacement for each temperature are calculated.

T, K	1	2	3	7	8	9	1/2	7/8	2-1	8-7
303	855.57	857.22	859.36	872.89	874.85	877.3	0.49	0.39	1.65	1.96
100	851.51	854.60	857.57	872.81	875.97	878.29	0.57	1.89	3.09	3.16
303	854.62	856.09	858.29	872.07	874.04	877.7	0.63	1.16	1.47	1.97
493	853.50	855.00	857.30	871.30	872.7	873.6	0.14	1.86	1.56	1.4
673	853.40	854.80	856.80	871.14	872.4	873.9	0.23	1.01	1.45	1.29

Table 4.4: The details of fitting of nickel spectra of S-42Aw sample for various temperatures. The position of fitted peak maximum, area ratio between constituent lines and energy displacement for each temperature are calculated.

T, K	1	2	3	7	8	9	1/2	7/8	2-1	8-7
303	855.04	856.46	857.58	872.26	874.42	876.78	1.50	0.83	1.42	2.16
103	854.4	856.09	858.27	871.93	873.88	876.46	1.30	1.4	1.69	1.95
303	853.85	855.03	857.1	871.98	873.93	876.4	0.21	1.67	1.18	1.95
493	855.02	856.2	857.48	872.09	874.06	876.17	1.74	2.65	1.18	1.97

Table 4.5: The details of fitting of nickel spectra of S-30AOn sample for various temperatures. The position of fitted peak maximum, area ratio between constituent lines and energy displacement for each temperature are calculated.

T, K	1	2	3	7	8	9	1/2	7/8	2-1	8-7
103	855.78	857.20	858.95	873.11	874.48	875.80	0.62	0.79	1.42	1.37
303	854.56	855.77	858.24	872.01	873.48	875.31	0.35	0.82	1.21	1.47
493	854.34	855.54	857.71	871.88	873.24	876.45	0.35	0.36	1.2	1.36

the peak displacement and area ratio are much larger than for sample S-36AOw at lower temperature. At high temperatures, at 683 K for S-36AOw and at 673 K for S-12AOw, the area ratio of peaks 1:2 forming the Ni $2p_{3/2}$ line are quite similar - 0.18 and 0.23 respectively for both samples.

The energy displacement between peaks 1 and 2 at temperature below RT is about 1.34 eV for S-36AOw and 3.09 eV for S-12AOw. While temperature increases, the separation diminishes for both samples and well above MI transition temperature it is about 1.3 eV for S-36AOw and 1.45 eV for S-12AOw.

It is not unusual to see that also annealed film deposited in pure argon does exhibit temperature variation of nickel spectra (figure 4.19).

The same analysis was performed for film deposited without annealing. Some additional low energy peaks at low temperature were necessary to be added which were not taken into account when discussing the spectra variation with temperature.

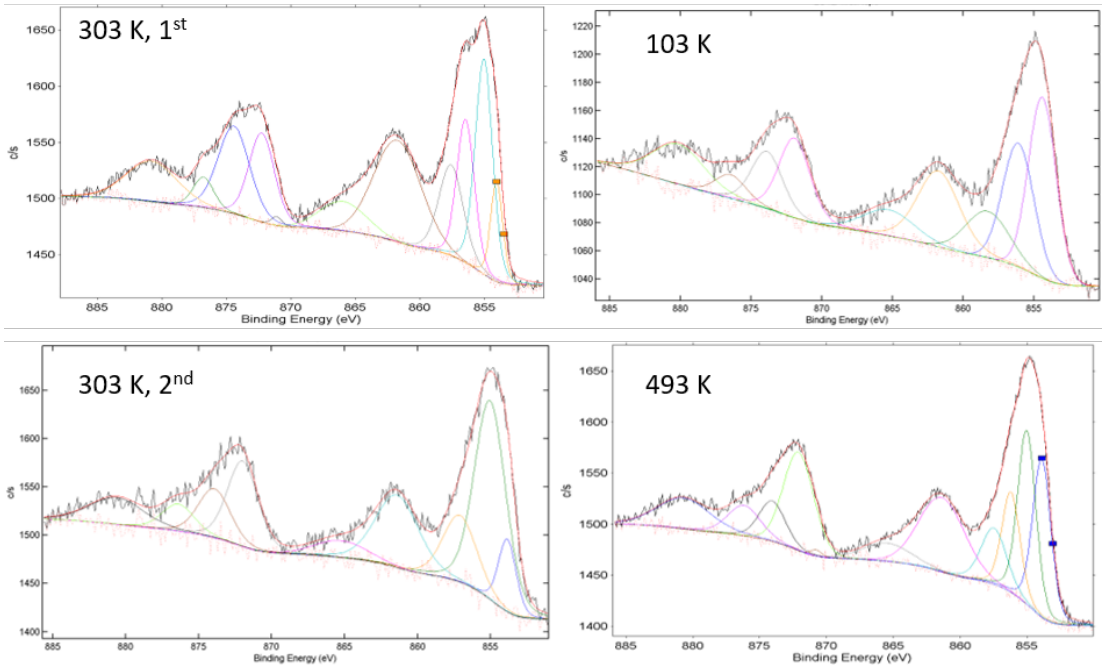

Figure 4.19: Temperature dependence of nickel 2p multiplet spectra for sample S-42Aw - A distinct splitting of $2p_{3/2}$ envelope is evident in initial spectrum at room temperature, this splitting disappears in the course of heating and does not occur in the re-measured spectrum at RT.

4.4 Discussion on nickel electronic state

The electronic spectrum of nickel 2p line is complicated regardless of studied compound. Various studies as well as calculations have shown that the multiplet spectrum is best fitted with a multiple-component envelope for any chemical state of nickel, whether it is metallic nickel, Ni+, Ni2+, Ni3+, Ni4+. A true assignment of constituent peaks to multiplet Ni2p envelope in $SmNiO_3$ compound would require performing advanced calculations that take into account the effects of the solid state, effects of reduced dimensions, non-zero temperature and possible coexistence of several chemical states. This work does not include such calculations therefore a reduced peak assignment at each spectrum was used. In such reduced spectrum possible existing groups of constituent peaks were approximated by a single Gauss-Lorentz curve, and number of curves was strictly dependent of experimental necessity - each inflexion point in Ni 2p spectrum was given one line. This way a minimum number of curves was used to fit obtained spectra.

Because of difficulties in attribution of peaks and the structure of Ni 2p lines,

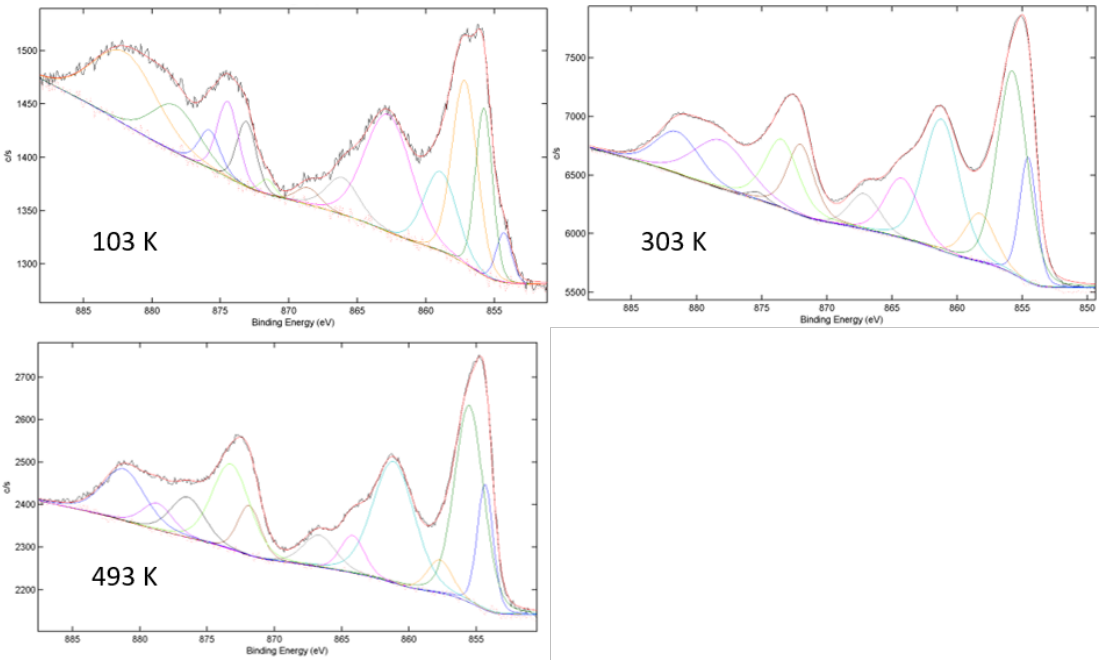

Figure 4.20: Nickel 2p multiplet spectrum fitting at for sample S-30AOn - A distinct splitting of $2p_{3/2}$ envelope is evident at low temperature, this splitting disappears in the course of heating.

the absolute values of line positions are not discussed here. However, the obtained fitting results still hold value for comparison of spectra for various temperatures and samples when comparing energy displacement between individual constituent lines (that are probably groups of peaks) as well as peak area ratios. The mentioned parameters when compared with respect to temperature or sample thickness have provided ground to draw conclusions of variation of electronic structure across investigated metal-insulator transition.

Nickel spectra collected for samarium nickelate thin films present subtle changes with respect to temperature. In-depth analysis of two constituent lines of main part of Ni 2p multiplet, that is Ni $2p_{3/2}$ line, revealed transfer of spectral weight between the two lines but more importantly a temperature dependent variation of energy difference between them. For each annealed $SmNiO_3$ thin film a general trend is that the energy difference between the two peaks decreases while temperature increases. What is more, for thinner films the energy difference is larger in comparison with respective spectra for films with greater thickness, regardless of temperature.

On the other hand, investigation of spectra of as-deposited films revealed that the energy difference between the first and second peak is also slightly influenced by temperature change. This might be related to the presence of the main perovskite phase also in those samples.

5

Conclusions

This work was performed in order to understand what physical parameters, or their combination, trigger the metal-insulator transition in $SmNiO_3$ thin film materials. This required a set of samples with a selected varying feature, such as film thickness, and their thorough investigation by a broad range of modern measurement techniques. Obtained materials were analyzed using various techniques such as microscopy, spectroscopy and diffraction in order to gain insight into a phenomenon that made the compound recognizable, that is the metal-insulator transition. Some of the techniques, such as X-ray diffraction, Time-of-Flight Secondary Ion Mass Spectroscopy and X-ray Fluorescence Spectroscopy were used solely for initial film characterization. While X-ray Photoelectron Spectroscopy, Atomic Force Microscopy and its variation Local Conductivity Atomic Force Microscopy, as well as Raman Spectroscopy, were the core techniques that provided means for investigation of metal-insulator phenomenon.

Direct macroscopic method to verify the presence of metal-insulator transition, that is the macroscopic temperature resistance measurements, was found to be unfit for the investigation of obtained materials. The utmost reason for that was the presence of a layer of contaminations which prevented a proper electrical current flow between electrical contacts and prevented us from obtaining reliable data. While the macroscopic technique was not sufficient, a microscopic technique, the LC-AFM, was more dedicated for the investigation of the system.

The magnetron sputtering was the method for the thin film production. Investigated $SmNiO_3$ films were deposited on silicon Si(100) substrate. Due to variable deposition conditions such as plasma composition and deposition time as well as post-processing treatment, the obtained films varied in terms of thickness,

chemical composition and crystalline structure. Large lattice mismatch of the film-substrate system forced strain on deposited films. As X-ray diffraction experiments have shown, depending on the thickness of the film the level of strain is different but smaller for thicker films or for films deposited in pure argon plasma atmosphere. The atmospheric condition in deposition chamber may have also influenced the surface of silicon substrate which is covered with a layer of oxidized silicon whose structure was not detectable in the course of investigation.

The annealing procedure after deposition was necessary to stabilize the perovskite structure. Without that step, films did not present long-range crystal order in diffraction experiments as well as no critical temperature in Raman spectroscopy experiments. Presence of oxygen as the second component of plasma in the sputtering deposition chamber (AO films) resulted in formation of highly textured films. The texture was not formed in films deposited in pure argon plasma. Even though further high temperature and high-pressure oxygen annealing were applied, the later films did not form any crystalline texture. The films sputtered by argon plasma (A films) have been found to have almost twice the thickness as respective AO films despite the same deposition time. What is more the calculated pseudocubic parameter is larger, the lattice mismatch lower and the atomic ratio of Sm:Ni atoms present in the films is much lower for A films than for AO films.

Experimental results have confirmed that for magnetron sputtered SNO films deposited on silicon substrate annealing is the necessary step to obtain the proper crystalline structure which exhibits metal-insulator transition. The as-deposited films do not present the signature of the perovskite structure neither in X-ray diffraction patterns nor in Raman spectra. It is however interesting that X-ray photoelectron spectra of not annealed film do exhibit temperature dependence. The most visible change occurs between 103 K and room temperature - the separation of 2p3/2 constituent lines decreases and there is a shift of spectral weight from lower to higher binding energy.

However, for the as-deposited film, the energy difference decreases for only about 0.2 eV. Whereas for films that underwent the annealing procedure the change was as large as about 1.5 eV for S-12AOw thin film or 0.7 eV for much thicker S-36AOw film.

The annealing operation was done in order to stabilize the perovskite structure and nickel ion in 3+ chemical state. High oxygen pressure and temperature were necessary to 'pump' oxygen atoms deep into the film's structure. Extensive annealing time favoured film crystallization and formation of long-range order.

Before annealing, the species that built the film were presumably highly defected amorphous $SmNiO_{3-\delta}$ molecules with low stoichiometry. Because many of the oxygen atoms were missing, the NiO_6 octahedra were not complete and having broken bonds. However, I would argue that some of the molecules exhibit complete well-established SNO unit cells and may react to temperature variation.

For annealed films, the results obtained from various techniques came together and formed following relationships. Films deposited in argon were polycrystalline with the smallest lattice mismatch from all measured films. They had the smallest Raman shift of the band selected for analysis. The critical temperature at which the band softening ends was also the lowest and closest to MI transition temperature for bulk materials, that is about 400 K. The lowest tensile strain would be in agreement with the Ni-O bonds being less stretched out so the temperature-induced overlap of nickel and oxygen electron bands was easier (energetically) than for materials with more elongated bonds. The Ni 2p XPS peak separations at room and higher temperatures were low in comparison to other annealed films but still were higher than the thickest AO film at lower temperatures.

The AO films had the highest strain for the lowest film thickness, and while the thickness increased, the strain diminished. However there was a noticeable minimum of strain for sample S-24AOw (about 160 nm in thickness). The increase of thickness correlated with the decrease of the strength of band softening. The critical temperature in Raman band softening was not clearly correlated with film thickness, however a slight decrease in temperature with film thickness increase was noted. Nevertheless, one has to remember that with the presented data it was difficult to estimate the exact critical temperature. On the other hand, the thicker films exhibited smaller energy separation between constituent peaks of Ni $2p_{3/2}$ line and the temperature variation of that energy value was less severe than for thinner films.

Measurements of local conductivity across a wide temperature range have inevitably shown that MI transition does take place in investigated SNO films. The IV characteristics were semiconductor-like below a certain temperature, while at temperatures close to 400 K the current response evolved to nearly linear - an indication of metallic conductivity. At the same time Raman experiments indicated the transition was not complete as the mode softening continued even at higher temperatures.

The complex spectrum of nickel 2p underwent temperature changes in such a way that the constituent peaks of main photoelectron line shifted towards each other so that the energy separation between them become smaller. Those changes

were evidenced in whole temperature range of measurements, however they were more rapid in the low to room temperature range. Further increase in temperature triggered comparably smaller changes in the energy shift. Yet, this separation was still present at high temperatures, above the transition. Such behaviour supports the theory of charge disproportion effect. Although this effect was also present in unannealed films that did not hold the proper structure. I assume, that the effect most likely appeared locally at chosen sites of better stoichiometry. At the same time, the same change visible on the metallic conductivity would require a common change appearing across whole sample volume. Such changes were evidenced in other compounds from the nickelate family. In neodymium nickelate thin films, where changes in peak position and relative intensity appeared with temperature variation (27). A shift towards higher binding energy at low temperature was observed for all films, with the highest shift in thickest (150 nm) film. However for those materials the largest change in line separation was observed for thickest film, unlike in SNO films in this work.

To conclude, I have found that the 'magnitude' of MI transition evidently depends on the thickness of SNO film. This magnitude' of MI transition is understood as a variation (change) of transition temperature, magnitude of Raman band softening and XPS peak energy separation. The thinner the film, the more prominent are the observed changes. The energy separation of XPS peaks is higher, thus the required temperature also increases. Stronger XPS effects for A films may stem from the possibly larger disorder and disturbed stoichiometry than corresponding AO films. At the same time, at the higher temperatures, this separation becomes lower than for other films which may indicate that structural changes can appear more easily in a polycrystalline material.

6

Future concepts

Thin film materials exhibiting metal-insulator transition are an important element of nowadays science and technology. The enticement to change material properties on demand by using external factors is not only appealing for engineering but, as boisterously as it sounds, is a part of human nature to want control the world around. As for science, any change in the world around is interesting and worth investigating.

The work carried out in favour of the presented thesis is only a small part of knowledge about metal-insulator transition in samarium nickel oxide materials. The very specific materials that were under study were deposited by magnetron sputtering technique on monocrystalline silicon (100) substrate. Films of various thicknesses and various structural properties were obtained as a result of modification of deposition time and atmosphere and post-processing. Investigation of such group of nominally $SmNiO_3$ chemical compounds facilitated getting insight into the crucial phenomena that emerges in those compounds - the metal-insulator transition.

Bibliography

[1] Adachi, G.y. & Imanaka, N. (1998). The Binary Rare Earth Oxides. *Chem. Rev.*, **98**, 1479–1514. 4

[2] Alonso, J.A., Martínez-Lope, M. & Hidalgo, M. (1995). Hole and Electron Doping of $RNiO_3$ (R= La, Nd). *Journal of Solid State Chemistry*, **116**, 146–156. 11

[3] Alonso, J.A., Martínez-Lope, M. & Rasines, I. (1995). Preparation, crystal structure, and metal-to-insulator transition of $EuNiO_3$. *Journal of Solid State Chemistry*, **120**, 170–174. 9, 10

[4] Alonso, J.A., García-Muñoz, J.L., Fernández-Díaz, M.T., Aranda, M.A.G., Martínez-Lope, M.J. & Casais, M.T. (1999). Charge Disproportionation in $RNiO_3$ Perovskites: Simultaneous Metal-Insulator and Structural Transition in $YNiO_3$. *Phys. Rev. Lett.*, **82**, 3871–3874. 6

[5] Alonso, J.a., Martínez-Lope, M., Casais, M.T., Martinez, J., Demazeau, G., Largeteau, a., García-Muñoz, J.L. & Fernández-Díaz, M. (1999). High-Pressure Preparation, Crystal Structure, Magnetic Properties, and Phase Transitions in $GdNiO_3$ and $DyNiO_3$ Perovskites. *Chem. Mater.*, **11**, 2463–2469. 6

[6] Alonso, J.A., Martínez-Lope, M.J., Casais, M.T., Aranda, M.a.G. & Fernández-Díaz, M.T. (1999). Metal-Insulator Transitions, Structural and Microstructural Evolution of $RNiO_3$ (R = Sm, Eu, Gd, Dy, Ho, Y) Perovskites: Evidence for Room-Temperature Charge Disproportionation in Monoclinic $HoNiO_3$ and $YNiO_3$. *J. Am. Chem. Soc.*, **121**, 4754–4762. 6

[7] Alonso, J.A., Martínez-Lope, M.J., Casais, M.T. & Fernández-Díaz, M.T. (2000). Room-temperature monoclinic distortion due to charge disproportionation in $RNiO_3$ perovskites with small rare-earth cations (R=Ho, Y, Er, Tm, Yb, and Lu): A neutron diffraction study. *Phys. Rev. B*, **61**, 1756–1763. 6

[8] Alonso, J.A., Martínez-Lope, M.J., Casais, M.T., García-Muñoz, J.L., Fernández-Díaz, M.T. & Aranda, M.A.G. (2001). High-temperature structural evo-

lution of $RNiO_3$ (R=Ho,Y,Er,Lu) perovskites: Charge disproportionation and electronic localization. *Phys. Rev. B*, **64**, 094102. 6

[9] Aydogdu, G.H., Ha, S.D., Viswanath, B. & Ramanathan, S. (2011). Epitaxy, strain, and composition effects on metal-insulator transition characteristics of $SmNiO_3$ thin films. *Journal of Applied Physics*, **109**, 124110. 48, 60, 61

[10] Biesinger, M.C., Brown, C., Mycroft, J.R., Davidson, R.D. & McIntyre, N.S. (2004). X-ray photoelectron spectroscopy studies of chromium compounds. *Surface and Interface Analysis*, **36**, 1550–1563. 73

[11] Biesinger, M.C., Payne, B.P., Lau, L.W.M., Gerson, A. & Smart, R.S.C. (2009). X-ray photoelectron spectroscopic chemical state quantification of mixed nickel metal, oxide and hydroxide systems. *Surface and Interface Analysis*, **41**, 324–332. 50, 51

[12] Bilewska, K., Wolna, E., Edely, M., Ruello, P. & Szade, J. (2010). Evidence of charge disproportionation on the nickel sublattice in $EuNiO_3$ thin films: X-ray photoemission studies. *Phys. Rev. B*, **82**, 165105. 106

[13] Catalan, G. (2008). Progress in perovskite nickelate research. *Phase Transitions*, **81**, 729–749. 59

[14] Catalan, G., Bowman, R.M. & Gregg, J.M. (2000). Metal-insulator transitions in $NdNIO_3$ thin films. *Phys. Rev. B*, **62**, 7892–7900. 23

[15] Catalan, G., Bowman, R.M. & Gregg, J.M. (2000). Transport properties of $NDNIO_3$ thin films made by pulsed-laser deposition. *Journal of Applied Physics*, **87**, 606–608. 59

[16] Chen, H.L., Lu, Y.M., Wu, J.Y. & Hwang, W.S. (2005). Effects of Substrate Temperature and Oxygen Pressure on Crystallographic Orientations of Sputtered Nickel Oxide Films. *Materials Transactions*, **46**, 2530–2535. 82

[17] Conchon, F., Boulle, A., Girardot, C., Pignard, S., Guinebretière, R., Dooryhée, E., Hodeau, J.L., Weiss, F., Kreisel, J. & Bérar, J.F. (2007). Epitaxial stabilization of $SmNiO_3$ films on (0 0 1) $SrTiO_3$ substrates. *Journal of Physics D: Applied Physics*, **40**, 4872–4876. 60

[18] Counsell, J.D.P., Roberts, A.J., Boxford, W., Moffitt, C. & Takahashi, K. (2014). Reduced Preferential Sputtering of TiO_2 using Massive Argon Clusters. *Journal of Surface Analysis*, **20**, 211–215. 49

[19] Cullity, B.D. (1978). *Elements of X-Ray Diffraction*. Addison-Wesley Publishing Company, Inc., Nôtre Dame, Indiana. 36

[20] Czternastek, H. (2004). ZnO thin films prepared by high pressure magnetron sputtering. *Opto-Electronics Review*, **12**, 49–52. 82

[21] Demazeau, G., Marbeuf, A., Pouchard, M. & Hagenmuller, P. (1971). Sur une série de composés oxygènes du nickel trivalent derivés de la perovskite. *J. Solid State Chem.*, **3**, 582–589. 6

[22] Downs, R.T. & Hall-Wallace, M. (2003). The American Mineralogist Crystal Structure Database. *American Mineralogist*, **88**, 247–250. 38

[23] Fanciulli, M. & Scarel, G., eds. (2007). *Rare Earth Oxide Thin Films. Growth, Characterization, and Applications*. Springer-Verlag, Berlin/Heidelberg. xvii, 3, 4, 5

[24] Fernández-Díaz, M.T., Alonso, J., Martínez-Lope, M., Casais, M., García-Muñoz, J. & Aranda, M. (2000). Charge disproportionation in $RNiO_3$ perovskites. *Phys. B Condens. Matter*, **276-278**, 218–221. 6

[25] Frand, G., Bohnke, O., Lacorre, P., Fourquet, J., Carre, A., Eid, B., Theobald, J. & Gire, A. (1995). Tuning of Metal/Insulator Transition around Room Temperature of Perovskites $Sm_{1-x}Nd_xNiO_3$. *Journal of Solid State Chemistry*, **120**, 157–163. 10

[26] Freund, L.B. & Nix, W.D. (1996). A critical thickness condition for a strained compliant substrate/epitaxial film system. *Applied Physics Letters*, **69**, 173–175. 23

[27] Galicka, K., Szade, J., Ruello, P., Laffez, P. & Ratuszna, A. (2009). The photoemission study of $NdNiO_3/NdGaO_3$ thin films, through the metal-insulator transition. *Applied Surface Science*, **255**, 4355–4361. 120

[28] García-Muñoz, J.L., Rodriguez-Carvajal, J. & Lacorre, P. (1992). Sudden Appearance of an Unusual Spin Density Wave At the Metal-Insulator Transition in the Perovskites RNiO3 (R= Pr, Nd). *Europhysics Letters*, **20**, 241–247. 14

[29] García-Muñoz, J.L., Rodríguez-Carvajal, J., Lacorre, P. & Torrance, J.B. (1992). Neutron-diffraction study of $RNiO_3$ (R=La,Pr,Nd,Sm): Electronically induced structural changes across the metal-insulator transition. *Phys. Rev. B*, **46**, 4414–4425. 5, 6, 7, 8, 18

[30] Gasgnier, M. (1980). Rare earth metals, rare earth hydrides, and rare earth oxides as thin films a critical review. *Physica Status Solidi (A)*, **57**, 11–57. 3

[31] Gauglitz, G. & Vo-Dinh, T., eds. (2003). *Handbook of Spectroscopy*. WILEY-VCH Verlag GmbH & Co. KGaA, Weinheim. 40, 41

[32] Georges, A., Kotliar, G., Krauth, W. & Rozenberg, M.J. (1996). Dynamical mean-field theory of strongly correlated fermion systems and the limit of infinite dimensions. *Rev. Mod. Phys.*, **68**, 13–125. 17

[33] Girardot, C., Conchon, F., Boulle, A., Chaudouet, P., Caillault, N., Kreisel, J., Guinebretière, R., Weiss, F. & Pignard, S. (2007). Influence of thickness on the epitaxial stabilisation of $SmNiO_3$ thin films. *Surface and Coatings Technology*, **201**, 9021–9024. 60, 61

[34] Girardot, C., Kreisel, J., Pignard, S., Caillault, N. & Weiss, F. (2008). Raman scattering investigation across the magnetic and metal-insulator transition in rare earth nickelate $RNiO_3$ (R = Sm, Nd) thin films. *Phys. Rev. B*, **78**, 104101. 102

[35] Granados, X., Fontcuberta, J., Obradors, X. & Torrance, J.B. (1992). Metastable metallic state and hysteresis below the metal-insulator transition in $PrNiO_3$. *Phys. Rev. B*, **46**, 15683–15688. 19, 20

[36] Granados, X., Fontcuberta, J., Obradors, X., Manosa, L. & Torrance, J.B. (1993). Metallic state and the metal-insulator transition of $NdNiO_3$. *Physical Review B*, **48**, 11666–11672. 8, 18, 19, 20, 21

[37] Gražulis, S. (2003). Crystallography Open Database. Open-access collection of crystal structures of organic, inorganic, metal-organics compounds and minerals, excluding biopolymers. http://www.crystallography.net/cod/index.php. 38

[38] Gražulis, S., Daškevič, A., Merkys, A., Chateigner, D., Lutterotti, L., Quirós, M., Serebryanaya, N.R., Moeck, P., Downs, R.T. & Le Bail, A. (2012). Crystallography open database (cod): an open-access collection of crystal structures and platform for world-wide collaboration. *Nucleic Acids Research*, **40**, D420–D427. 38

[39] Gražulis, S., Chateigner, D., Downs, R.T., Yokochi, A.F.T., Quirós, M., Lutterotti, L., Manakova, E., Butkus, J., Moeck, P. & Le Bail, A. (2009). Crystallography Open Database - an open-access collection of crystal structures. *Journal of Applied Crystallography*, **42**, 726–729. 38

[40] Gražulis, S., Merkys, A., Vaitkus, A. & Okulič-Kazarinas, M. (2015). Computing stoichiometric molecular composition from crystal structures. *Journal of Applied Crystallography*, **48**, 85–91. 38

[41] Greenblatt, M. (1997). Ruddlesden-Popper $Ln_{n+1}Ni_{n0}O_{3n+1}$ nickelates: structure and properties. *Current Opinion in Solid State and Materials Science*, **2**, 174–183. 6, 7

[42] Greene, J.E. (1993). *Multicomponent and Multilayered Thin Films for Advanced Microtechnologies: Techniques, Fundamentals and Devices*, chap. Physics of Film Growth from the Vapor Phase, 39–85. Springer Netherlands, Dordrecht. 69

[43] Grosvenor, A.P., Biesinger, M.C., Smart, R.S. & McIntyre, N.S. (2006). New interpretations of xps spectra of nickel metal and oxides. *Surface Science*, **600**, 1771 – 1779. 47, 49, 50, 51

[44] Guan, L., Zuo, J., Jia, G., Liu, Q., Wei, W., Guo, J., Dai, X., Liu, B., Wang, Y. & Fu, G. (2013). Structural stability and electronic properties of lao- and nio2-terminated lanio3 (0 0 1) surface. *Applied Surface Science*, **264**, 570 – 573. 23, 24

[45] Gupta, R.P. & Sen, S.K. (1974). Calculation of multiplet structure of core p-vacancy levels. *Phys. Rev. B*, **10**, 71–77. 49

[46] Gupta, R.P. & Sen, S.K. (1975). Calculation of multiplet structure of core p -vacancy levels. ii. *Phys. Rev. B*, **12**, 15–19. 48, 49, 50

[47] Gutzwiller, M.C. (1965). Correlation of electrons in a narrow s band. *Phys. Rev.*, **137**, A1726–A1735. 16

[48] Ha, S.D., Aydogdu, G.H. & Ramanathan, S. (2011). Examination of insulator regime conduction mechanisms in epitaxial and polycrystalline $SmNiO_3$ thin films. *Journal of Applied Physics*, **110**. 29, 30, 33

[49] Ha, S.D., Aydogdu, G.H. & Ramanathan, S. (2011). Metal-insulator transition and electrically driven memristive characteristics of $SmNiO_3$ thin films. *Applied Physics Letters*, **98**. 28, 31

[50] Ha, S.D., Otaki, M., Jaramillo, R., Podpirka, A. & Ramanathan, S. (2012). Stable metal-insulator transition in epitaxial $SmNiO_3$ thin films. *Journal of Solid State Chemistry*, **190**, 233 – 237. 27, 28

[51] Ham, N.S. (1962). The Jahn-Teller theorem. *Spectrochim. Acta*, **18**, 775–789. 13

[52] Horcas, I., Fernández, R., Gomez-Rodriguez, J., Colchero, J., Gomez-Herrero, J. & Baro, A.M. (2007). WSxM: A software for scanning probe microscopy and a tool for nanotechnology. http://www.wsxm.es/. 55

[53] Horcas, I., Fernández, R., Gómez-Rodríguez, J.M., Colchero, J., Gómez-Herrero, J. & Baro, A.M. (2007). Wsxm: A software for scanning probe microscopy and a tool for nanotechnology. *Review of Scientific Instruments*, **78**, 013705. 55

[54] Howng, W.Y. & Thorn, R. (1980). Investigation of the electronic structure of $La_{1-x}(M^{2+})_xCrO_3$, Cr_2O_3 and La_2O_3 by X-ray photoelectron spectroscopy. *Journal of Physics and Chemistry of Solids*, **41**, 75 – 81. 73

[55] Hsiao, C.L. & Qi, X. (2013). Substrate-dependant chemical stability and conductivity of $LaNiO_{3-x}$ thin films. *Thin Solid Films*, **529**, 356–359. 25, 27

BIBLIOGRAPHY

[56] Hyeon Lee, S., Kim, M., Ha, S.D., Lee, J.W., Ramanathan, S. & Tiwari, S. (2013). Space charge polarization induced memory in $SmNiO_3$/Si transistors. *Applied Physics Letters*, **102**, 072102. 32

[57] Ihzaz, N., Oumezzine, M., Kreisel, J., Vincent, H. & Pignard, S. (2008). Growth of $SmNiO_3$ Thin Films on $LaAlO_3$ Single Crystals. *Chemical Vapor Deposition*, **14**, 111–114. 60, 61

[58] Ikemoto, I., Ishii, K., Kinoshita, S., Kuroda, H., Franco, M.A. & Thomas, J. (1976). X-ray photoelectron spectroscopic studies of CrO_2 and some related chromium compounds. *Journal of Solid State Chemistry*, **17**, 425 – 430. 73

[59] Imada, M., Fujimori, A. & Tokura, Y. (1998). Metal-insulator transitions. *Reviews of Modern Physics*, **70**, 1039–1263. 14

[60] Iwasa, Y., Kawasaki, M., Keimer, B., Nagaosa, N. & Tokura, Y. (2012). Emergent phenomena at oxide interfaces. *Nature Materials*, **11**, 103–113. 1

[61] Jaramillo, R., Schoofs, F., Ha, S.D. & Ramanathan, S. (2013). High pressure synthesis of $SmNiO_3$ thin films and implications for thermodynamics of the nickelates. *Journal of Materials Chemistry C*, **1**, 2455. 24, 25, 26, 27, 59, 61

[62] Jena, A. & Nanda, B.R.K. (1965). Unconventional Magnetism and Band Gap Formation in $LiFePO_4$: Consequence of Polyanion Induced Non-planarity. *Scientific Reports*, **6**, 19573. 14, 15

[63] Kittel, C. (1996). *Introduction to Solid State Physics*. John WIley & Sons Inc., Ney York, USA. 20

[64] Klapetek, P. & Nečas, D. (2004). Gwyddion - Free SPM data analysis software. http://gwyddion.net/. 55

[65] Ku, R. & Winterbottom, W. (1985). Electrical conductivity in sputter-deposited chromium oxide coatings. *Thin Solid Films*, **127**, 241 – 256. 93

[66] Lacorre, P., Torrance, J.B., Pannetier, J., Nazzal, A.I., Wang, P. & Huang, T. (1991). Synthesis, crystal structure, and properties of metallic $PrNiO_3$: Comparison with metallic $NdNiO_3$ and semiconducting $SmNiO_3$. *Journal of Solid State ChemistrY*, **91**, 225–237. 6, 7, 13, 39

[67] Laffez, P., Zaghrioui, M., Monot, I., Brousse, T. & Lacorre, P. (1999). Microstructure and metal-insulator transition of $NdNiO_3$ thin films on various substrates. *Thin Solid Films*, **354**, 50–54. 59

[68] Langjahr, P., Lange, F., Wagner, T. & Rühle, M. (1998). Lattice mismatch accommodation in perovskite films on perovskite substrates. *Acta Materialia*, **46**, 773 – 785. 23

[69] Lee, Y.E., Lee, J.B., Kim, Y.J., Yang, H.K., Park, J.C. & Kim, H.J. (1996). Microstructural evolution and preferred orientation change of radio-frequency - magnetron sputtered ZnO thin films. *Journal of Vacuum Science & Technology A*, **14**, 1943–1948. 82

[70] Leger, J., Yacoubi, N. & Loriers, J. (1981). Synthesis of rare earth monoxides. *Journal of Solid State Chemistry*, **36**, 261 – 270. 3

[71] Li, Z., Zhou, Y., Qi, H., Pan, Q., Zhang, Z., Shi, N.N., Lu, M., Stein, A., Li, C.Y., Ramanathan, S. & Yu, N. (2016). Correlated perovskites as a new platform for super-broadband-tunable photonics. *Advanced Materials*, **28**, 9117–9125. 2

[72] Makarevich, A., Kharchenko, A., Mankevich, A., Tsymbarenko, D., Korsakov, I. & Grigoriev, A. (2010). Epitaxial $LnNiO_3$ (Ln=La, Pr, Nd, Sm) films from 4f-3d heterometallic complexes. *Thin Solid Films*, **518**, 4696–4700. 60

[73] Matienzo, J., Yin, L.I., Grim, S.O. & Swartz, W.E. (1973). X-ray photoelectron spectroscopy of nickel compounds. *Inorganic Chemistry*, **12**, 2762–2769. 47

[74] Matthews, J. & Blakeslee, A. (1974). Defects in epitaxial multilayers: I. misfit dislocations. *Journal of Crystal Growth*, **27**, 118–125. 23

[75] McCreery, R.L. (2000). *Raman Spectroscopy for Chemical Analysis. v.157*. John Wiley & Sons Inc., Columbus, Ohio. 56, 57

[76] Medarde, M.L. (1997). Structural, magnetic and electronic properties of perovskites (R= rare earth). *Journal of Physics: Condensed Matter*, **9**, 1679–1707. 5, 6

[77] Medarde, M.L., Mesot, J., Rosenkranz, S., Lacorre, P., Gobrecht, K. & Fischer, P. (1995). Pressure dependence (internal and external) of the metallization process and the magnetic ordering of $PrNiO_3$: A neutron powder diffraction study. *Physica B: Condensed Matter*, **214-214**, 1025–1027. 11

[78] Medarde, M.L., Mesot, J., Rosenkranz, S., Lacorre, P., Marshall, W.G., Klotz, S., Loveday, J.S., Hamel, G., Hull, S. & Radaelli, P. (1997). Pressure-induced orthorhombic-rhombohedral phase transition in $NdNiO_3$. *Physica B: Condensed Matter*, **236**, 15–17. 5

[79] Merkys, A., Vaitkus, A., Butkus, J., Okulič-Kazarinas, M., Kairys, V. & Gražulis, S. (2016). *COD::CIF::Parser*: an error-correcting CIF parser for the Perl language. *Journal of Applied Crystallography*, **49**. 38

[80] Montero, J., Guillén, C., Granqvist, C.G., Herrero, J. & Niklasson, G.A. (2014). Preferential Orientation and Surface Oxidation Control in Reactively Sputter Deposited Nanocrystalline SnO_2:Sb Films: Electrochemical and Optical Results. *ECS Journal of Solid State Science and Technology*, **3**, N151–N153. 82

[81] Nečas, D. & Klapetek, P. (2012). Gwyddion: an open-source software for SPM data analysis. *Central European Journal of Physics*, **10**, 181–188. 55

[82] Obradors, X., Paulius, L., Maple, M., Torrance, J.B., Nazzal, A.I., Fontcuberta, J. & Granados, X. (1993). Pressure dependence of the metal-insulator transition in the charge-transfer oxides $RNiO_3$ (R= Pr, Nd, $Nd_{0.7}La_{0.3}$). *Physical Review B*, **47**, 12353–12356. 8, 9

[83] Ohring, M. (2002). *The Materials Science of Thin Films*, chap. Characterization of Thin Films, 273–275. Academic Press, San Diego. 38

[84] O'Keeffe, M. & Hyde, B.G. (1977). Some structures topologically related to cubic perovskite ($E2_1$), ReO_3 ($D0_9$) and Cu_3Au ($L1_2$). *Acta Crystallographica Section B*, **33**, 3802–3813. 9

[85] Quirós, M., Gražulis, S., Girdzijauskaitė, S., Merkys, A. & Vaitkus, A. (2018). Using SMILES strings for the description of chemical connectivity in the Crystallography Open Database. *Journal of Cheminformatics*, **10**. 38

[86] Rodriguez-Carvajal, J. (2006). Fullprof Suite. Crystallographic tools for Rietveld, profile matching & integrated intensity refinements of X-ray and/or neutron data. https://www.ill.eu/sites/fullprof/index.html. 38

[87] Sato, S., Takahashi, R., Kobune, M. & Gotoh, H. (2009). Basic properties of rare earth oxides. *Applied Catalysis A: General*, **356**, 57 – 63. 3

[88] Shi, J., Ha, S.D., Zhou, Y., Schoofs, F. & Ramanathan, S. (2013). A correlated nickelate synaptic transistor. *Nature Communications*, **4:2676**, 1–9. 2

[89] Suwas, S. & Ray, R.K. (2014). *Crystallographic Texture of Materials. Engineering Materials and Processes.*. Springer-Verlag, London. 81

[90] Suzuki, S., Sugiyama, K. & Waseda, Y. (2002). Changes in the chemical state and composition of the surface of iron oxides due to argon ion sputtering. *Journal of Surface Analysis*, **9**, 455–458. 49

[91] Tiwari, A. & Rajeev, K. (1998). Effect of oxygen stoichiometry on the electrical resistivity behaviour of $NdNiO_{3-\delta}$. *Solid State Communications*, **109**, 119 – 124. xvii, 11, 12, 19, 25, 29

[92] Torrance, J.B., Lacorre, P., Nazzal, A., Ansaldo, E.J. & Niedermayer, C. (1992). Systematic study of new insulator-metal transition in perovskite $RNiO_3$ (R = Pr, Nd, Sm, Eu) due to closing of the charge-transfer gap. *Physical Review B*, **45**, 8209–8212. 8, 9, 21

[93] Torriss, B., Margot, J. & Chaker, M. (2017). Metal-Insulator Transition of strained $SmNiO_3$ Thin Films: Structural, Electrical and Optical Properties. *Scientific Reports*, **7**, 40915. 93

[94] van Veenendaal, M.A. & Sawatzky, G.A. (1993). Nonlocal screening effects in $2p$ X-ray photoemission spectroscopy core-level line shapes of transition metal compounds. *Phys. Rev. Lett.*, **70**, 2459–2462. 47

[95] Vassiliou, J.K., Hornbostel, M., Ziebarth, R. & Disalvo, F. (1989). Synthesis and properties of $NdNiO_3$ prepared by low-temperature methods. *Journal of Solid State Chemistry*, **81**, 208–216. 5, 13, 18

[96] Viswanath, B., Aydogdu, G., Ha, S. & Ramanathan, S. (2012). In situ stress relaxation and diffraction studies across the metal-insulator transition in epitaxial and polycrystalline $SmNiO_3$ thin films. *Scripta Materialia*, **66**, 463–466. 60

[97] Wang, L., Ju, S., You, L., Qi, Y., wei Guo, Y., Ren, P., Zhou, Y. & Wang, J. (2015). Competition between strain and dimensionality effects on the electronic phase transitions in $NdNiO_3$ films. *Scientific Reports*, **5**, 18707. 18, 22, 30, 31

[98] Wartewig, S. (2003). *IR and Raman Spectroscopy. Fundamental Processing*. WILEY-VCH GmbH & Co. KGaA, Weinheim. 56

[99] Zaanen, J., Sawatzky, G.A. & Allen, J.W. (1985). Band gaps and electronic structure of transition-metal compounds. *Phys. Rev. Lett.*, **55**, 418–421. 14, 16, 19

[100] Zaghrioui, M., Bulou, A., Lacorre, P. & Laffez, P. (2001). Electron diffraction and Raman scattering evidence of a symmetry breaking at the metal-insulator transition of $NdNiO_3$. *Phys. Rev. B*, **64**, 081102. 102

[101] Zhou, Y., Guan, X., Zhou, H., Ramadoss, K., Adam, S., Liu, H., Lee, S., Shi, J., Tsuchiya, M., Fong, D.D. & Ramanathan, S. (2016). Strongly correlated perovskite fuel cells. *Nature*, **534**, 231–234. 2

List of author's publications

Drzazga, M., Prajsnar, R., Chmielarz, A., Benke, G., Leszczyńska-Sejda, K., Ciszewski, M., Bilewska, K. & Krawiec, G. (2018). Germanium and indium recovery from zinc metallurgy by-products dross leaching in sulphuric and oxalic acids. *Metals*, **8**, 1041.

Jonczy, I., Kamińska, M., Bilewska, K. & Gerle, A. (2018). Crystalline phases in the waste foundry sands based on quartz sand matrix. *Inżynieria i Ochrona Środowiska*, **21**, 213-226.

Jonczy, I., Kamińska, M. & Bilewska, K. (2018). Fazy siarczkowe i siarczanowe w żużlach hutniczych. *Archiwum Gospodarki Odpadami i Ochrony Środowiska*, **20**, 1-10.

Gorewoda, T., Mzyk, Z., Anyszkiewicz, J., Bilewska, K., Cybulski, A., Malara, S., Gołębiewska-Kurzawska, J., Knapik, M., Kostrzewa, J. & Grzegorczyk, M. (2017). Novel sample treatment procedures for the determination of phosphorus in Cu-based alloys using X-ray Fluorescence Spectrometry to solve the microstructural effect issue. *X-Ray Spectrometry*, **46**, 554-562.

Osadnik, M., Wrona, A., Lis, M., Kamińska, M., Bilewska, K., Czepelak, M., Czechowska, K., Moskal, G. & Więcław, G. (2017). Plasma-sprayed Mo-Re coatings for glass industry applications. *Surf. Coat. Tech.*, **318**, 349-354.

Wrona, A., Bilewska, K., Lis, M., Kamińska, M., Olszewski, T., Pajzderski, P., Więcław, G., Jaśkiewicz, M. & Kamysz, W. (2017). Antimicrobial properties of protective coatings produced by plasma spraying technique. *Surf. Coat. Tech.*, **318**, 332-340.

Księżarek, S., Kazana, W., Marszowski, K., Rudnicki, K., Płonka, A.,Woch, M., Śmieszek, Z., Staszewski, M., Kołacz, D., Kamińska, M. *et al.* (2017). Nanokrystaliczne druty bimetalowe żelazo-miedź - technologia i właściwości fizykomechaniczne. *Hutnik, Wiadomości Hutnicze*, **84**, 44-47.

Hryniszyn-Kula, A., Wrona, A., Czechowska, K., Lis, M., Bilewska, K., Tomczyk, P. & Stencel, M. (2017). Inżynieria materiałowa w walce z mikroorganizmami. Rudy i Metale Nieżelazne Recykling, **62**, 57-58.

Dulski, M., Bilewska, K., Wojtyniak, M., Szade, J., Kusz, J., Nowak, A., Wrzalik, R., Kubacki, J. & Galuskin, E. (2015). Rondorfite-type structure -

XPS and UV-VIS study. *Mater. Res. Bull.*, **70**, 920-927.

Wrona, A., Czechowska, K., Osadnik, M., Kamińska, M., Lis, M., Bilewska, K., Czepelak, M., Więcław, G. & Moskal, G. (2015). Composite ZrO_2-based cermet material modified with Mo. *Solid State Phenomen*, **237**, 3-8.

Wrona, A., Lis, M., Bilewska, K., Czechowska, K., Więcław, G., Moskal, G., Osadnik, M. & Kamińska, M. (2015). Warstwy ochronne na bazie metali wysokotopliwych wytwarzane techniką natryskiwania cieplnego. *Obróbka Plastyczna Metali*, **26**.

Kołacz, D., Czepelak, M., Rudnicki, K., Wrona, A., Księżarek, S., Kamińska, M., Staszewski, M. & Bilewska, K. (2015). Kompozytowy materiałstykowy na bazie srebra z dodatkiem azotku chromu przeznaczony na styki elektryczne. Rudy i Metale Nieżelazne Recykling, **60**, 361-368.

Staszewski, M., Czepelak, M., Kamińska, M., Ślusarek, A., Lis, M., Osadnik, M. & Bilewska, K. (2015). Materiały piezoelektryczne wytwarzane w Instytucie Metali Nieżelaznych w Gliwicach. *Rudy i Metale Nieżelazne Recykling*, **60**, 127-135.

Osadnik, M., Wrona, A., Czepelak, M., Lis, M., Czechowska, K., Kamiń ska, M. & Bilewska, K. (2014). Nowe pole zastosowań renu jako składnika kompozytów cermetalicznych. *Rudy i Metale Nież elazne Recykling*, **59**, 12-15.

Wrona, A., Bilewska, K., Mazur, J., Lis, M. & Staszewski, M. (2014). Properties of thermoelectric Zn-Sb type material directly synthesized by Spark Plasma Sintering. *J. Alloy. Compd.*, **616**, 350-355.

Staszewski, M., Kapias, P., Bilewska, K., Kamiń ska, M. & Osadnik, M. (2013). Quantitative X-ray phase analysis as a method of control of iron blende roasting process. *Solid State Phenomena*, **203**, 156-159.

Wrona, A., Sierczyń ska, A., Bilewska, K., Kamińska, M. & Staszewski, M. (2013). Stability of thermally processed $LaNi_5$-based alloys for hydrogen storage. *Solid State Phenomena*, **203**, 423-426.

Wrona, A., Leszczyńska-Sejda, K., Lis, M., Benke, G., Czepelak, M., Anyszkiewicz, K., Mazur, J., Bilewska, K., Chmielarz, A., Woch, M. *et al.* (2013). Sferyczne proszki ze stopów renu z kobaltem i niklem. *Rudy i Metale Nieżelazne*, **58**, 828-834.

Staszewski, M., Myczkowski, Z., Bilewska, K., Sosiński, R., Lis, M., Czepelak, M. & Kołacz, D. (2012). High-energy milling as a method for obtaining tetragonal form of PbO. *Journal of Achievements in Materials and Manufacturing Engineering*, **52**, 39-46.

Wrona, A., Mazur, J., Kamińska, M., Bilewska, K., Staszewski, M. & Czepelak, M. (2012). Dependence of microstructure induced with manufacturing parameters and physical properties of compound of skutterudite structure type $Ce_xFeCo_3Sb_{12}$. *AIP Conference Proceedings*, **1449**, 247-250. DOI: 10.1063/1.4731543.

Mazur, J., Wrona, A., Bilewska, K., Staszewski, M. & Lis, M.(2012). Temperature-controlled formation of microstructure of n-type bismuth telluride with SPS method. *AIP Conference Proceedings*, **1449**, 397. DOI: 10.1063/1.4731580.

Wrona, A., Staszewski, M., Mazur, J., Kamińska, M., Lis, M., Osadnik, M. & Bilewska, K. (2012). Wytwarzanie materiałow termoelektrycznych na osnowie związku Bi_2Te_3 technik(a spiekania plazmowego. *Rudy i Metale Nieżelazne*, **57**, 765-770.

Bilewska, K., Wolna, E., Edely, M., Ruello, P. & Szade, J. (2011). $EuNiO_3$ thin films - growth and characterization. *J. Phys.: Conf. Series*, **289**, 012014. 10.1088/1742-6596/289/1/012014

Bilewska, K., Wolna, E., Edely, M., Ruello, P. & Szade, J. (2010). Evidence of charge disproportionation on the nickel sublattice in $EuNiO_3$ thin films: X-ray photoemission studies. *Phys. Rev. B*, **82**, 165105. DOI: 10.1103/PhysRevB.82.165105